Deep-Inelastic Scattering off ^{14}N

Jeroen J. van Hunen

ISBN: 90-6488-014-X
Cover: wood engraving, Jaap F. van Hunen

Deep-Inelastic Scattering off ^{14}N

Diep-inelastische verstrooiing aan ^{14}N

(met een samenvatting in het Nederlands)

Proefschrift ter verkrijging van de graad van doctor aan
de Universiteit Utrecht op gezag van
de Rector Magnificus, Prof. Dr. H.O. Voorma,
ingevolge het besluit van het College voor Promoties
in het openbaar te verdedigen op
maandag 6 maart 2000 des middags te 16.15 uur

door

Jeroen Jaap van Hunen

geboren op 14 april 1968, te London, Canada

Promotor:	Prof. Dr. P.K.A. de Witt Huberts
	Faculteit der Natuur- en Sterrenkunde
Copromotor:	Dr. G. van der Steenhoven
	NIKHEF

The work described in this thesis is part of the research program of the "Stichting voor Fundamenteel Onderzoek der Materie (FOM)", which is financially supported by the "Nederlandse Organisatie voor Wetenschappelijk Onderzoek (NWO)".

Contents

1 Introduction **1**

2 Deep-Inelastic Scattering **7**
2.1 Formalism for deep inelastic scattering 7
2.1.1 Kinematics 8
2.1.2 DIS Cross section 10
2.1.3 Quark Parton Model 12
2.1.4 Nuclear effects 13
2.2 Formation of the final state 19
2.2.1 Semi-inclusive DIS cross section 20
2.2.2 Hadronization in the nuclear medium 20

3 The HERMES experiment **31**
3.1 Introduction 31
3.2 The HERA storage ring 31
3.3 Internal gas target at HERMES 32
3.4 The HERMES Spectrometer 32
3.4.1 Tracking detectors 33
3.4.2 Particle identification 33
3.4.3 Trigger 35
3.4.4 Detector performance 36

4 Vertex Chambers **37**
4.1 Introduction 37
4.2 Performance of the vertex chambers 38
4.2.1 Introduction 38
4.2.2 Design considerations 38
4.2.3 Performance of the MSGC 42

4.2.4 Conclusions 44
4.3 Occupancy of the MSGC at HERMES 45
4.4 MSGC's in other experiments 46

5 A-dependence of $R = \sigma_L/\sigma_T$ 47
5.1 Introduction 47
5.2 Cross section ratios for ^{14}N and ^{3}He 48
5.2.1 Event selection 48
5.2.2 Constraints on the lepton kinematics 50
5.2.3 Number of DIS events 51
5.2.4 Radiative corrections 51
5.2.5 Smearing corrections 53
5.2.6 Uncertainty in the cross section ratio 55
5.2.7 Results 56
5.3 Extraction of $R_{^{14}N}/R_D$ and $R_{^{3}He}/R_D$ 68
5.4 Interpretation of the data 83
5.4.1 The A-dependence of R 83
5.4.2 Results on σ_T^A/σ_T^D and σ_L^A/σ_L^D 83
5.5 Models for a nuclear enhancement of R 86
5.6 Conclusion 88

6 Hadron Attenuation in ^{14}N 91
6.1 Introduction 91
6.2 Determination of R_{att} 92
6.2.1 Event selection 93
6.2.2 Hadron and Pion identification 93
6.2.3 Acceptance 94
6.2.4 Kinematic distributions 95
6.2.5 Radiative corrections 96
6.2.6 Diffractive ρ^0 production 98
6.2.7 Systematic uncertainties 100
6.2.8 Results 101
6.3 Models for the attenuation ratio 107
6.3.1 One-time and two-time scale models 107
6.3.2 Gluon bremsstrahlung model 117
6.4 Conclusion 119

7 Summary 123

A DIS cross section expression **127**

B $R_A = R_D$ in the radiative corrections **129**

Bibliography **133**

Samenvatting **139**

Acknowledgements **143**

Chapter 1

Introduction

Quantum chromodynamics (QCD) is the theory that describes the (strong) interactions of quarks and gluons. The strength of the strong interaction in QCD is quantified by the coupling constant α_s. It is stronger than the electromagnetic interaction in quantum electrodynamics (QED), as shown for example by the fact that the strong force keeps the u quarks in the proton together, while the electromagnetic force is repulsive. Quarks interact by exchanging gluons, which are colored, massless, spin-1 particles. Gluons themselves interact mutually as well.

Although the QCD and QED frameworks are very similar, there are striking differences between the electromagnetic and the strong force. This is shown for example by the contrasting behavior of α_s and the fine structure constant α, as a function of the distance over which the forces extend. With increasing distance between the charges, i.e. electric charge for QED and color charge for QCD, the value of α decreases (screening), while α_s increases (anti-screening). At distances considerably smaller than the size of nucleons the quarks are loosely bound (asymptotic freedom). When the distance between the quarks increases, α_s grows rapidly. The result is a strong binding of the quarks, which are in fact confined within the nucleon (confinement).

Deep-inelastic scattering (DIS) experiments are used to investigate the quark-gluon structure of nucleons. In DIS experiments a high energy lepton is scattered off quarks inside the nucleon, leading to the breakup of the nucleon. The interaction is described as the emission and absorption of a virtual (since $E^2 \neq c^2p^2$) photon with energy ν by the incident charged lepton and quark, respectively. The DIS cross section is governed by the

structure function F_2, which describes the quark momentum distributions in nucleons. At present F_2 cannot be calculated from first principles, but can be determined experimentally.

Before 1982, the structure function F_2 was thought to be independent of the nucleus in which the target nucleon resides. The influence of the surrounding nucleons was expected to be negligible, as the energies involved in DIS (several GeVs) are much higher than those relevant for nuclei (several MeVs).

In 1982 it was found at CERN, however, that the F_2 structure function ratio of a target with atomic mass A and a deuterium target is not equal to unity, but a function of the Bjorken scaling variable (x) [1]. The phenomenon, known as the *EMC-effect* at high values of x ($x > 0.2$) and as *shadowing* at low values of x, triggered an enormous theoretical effort in order to understand the observations. The experimental results can be described by a variety of models and more experimental data are required to discriminate between them. An overview of the experimental and theoretical work until 1994 can be found in [2].

The deep-inelastic scattering cross section has both a longitudinal component σ_L and a transverse component σ_T. The structure function F_2 can be expressed in terms of σ_L and σ_T. Given the not well understood modification of F_2 inside the nuclear medium, it is of interest to study the A-dependence of σ_L and σ_T separately. This is particularly interesting since σ_L is sensitive to higher twist effects, i.e. quark-gluon correlations which are expected to be enhanced in nuclei [3, 4]. A convenient quantity to study is R, which represents the ratio of the absorption cross section of longitudinally and transversely polarized virtual photons ($R = \sigma_L/\sigma_T$). An A-dependence of R would thus indicate a difference in the A-dependence of σ_L and σ_T. Investigation of the A-dependence of R may help in understanding the A-dependence of F_2 better, and may supply information about interactions between quarks residing in different nucleons in the nucleus.

In this thesis we discuss how the HERMES experiment (DESY, Hamburg) found the first experimental evidence for an A-dependence of R. At the time of this writing no explicit calculations of such an effect are available. It can be argued, however, that these results possibly represent an indication for quark-gluon correlations which are enhanced in nuclei.

In the second part of this thesis the formation of hadrons in deep-inelastic

scattering is discussed. The struck and recoiling quarks can combine with other quarks and gluons that emerge during the break up of the target nucleon to form colorless particles. At the HERMES experiment it is possible to study the influence of the nuclear medium on the hadron formation process, and use the nucleus to derive information on the time needed to form a hadron (τ_f).

The process of hadron formation (referred to as hadronization) cannot be calculated in perturbative QCD (pQCD). This can be understood from the following consideration. Even though the quarks and gluons which form a hadron may have large energy, during hadronization the interactions between them involve small energy transfers, i.e. smaller than the restmass of a hadron. At these small energy transfers the interaction time and spatial separation can be large, as dictated by the uncertainty principle. Since α_s is large under these conditions, the participation of more quarks and gluons (higher order processes) cannot be neglected, i.e. pQCD cannot be applied.

By embedding the hadronization process in a nuclear medium, a method is offered to investigate the hadronization process. The quantity which is studied is the attenuation ratio (R_{att}), which is the number of hadrons observed per DIS event for a target with atomic mass A, divided by the same number for a deuterium target. For hadrons carrying a small energy fraction (z) of the virtual photon energy ν ($z = E_h/\nu$) the ratio can be larger than unity due to rescattering processes. For hadrons with a larger z, the ratio R_{att} is expected to be smaller than unity due to interactions between the quark and hadron with the nuclear medium. In order to investigate the time scales involved in hadron formation, hadrons with a relatively high energy fraction should be used. Some models for hadron attenuation assume a 'leading' hadron, i.e. a hadron that contains the quark which absorbed the virtual photon. The z value of these leading hadrons is expected to be high, i.e. $z > 0.5$. However, the exact values of the appropriate z-cut is not known, and therefore often chosen on the basis of experimental constraints (energy acceptance, events rates, etc.).

The attenuation depends on the interaction cross section of the quark (σ_s) with the nuclear medium and the formation time (τ_f) of the hadron. Hence, it may be possible to use such attenuation data to derive quantitative information on both σ_s and τ_f, while at present no experimental information exists on these quantities. The formation time τ_f and the cross section σ_s represent fundamental properties of the hadron formation process which are

of interest on their own, but are also needed in other fields. In heavy-ion physics, for instance, knowledge of the energy loss of a quark propagating in nuclear media is important for the analysis of signals that may indicate the formation of a guark-gluon plasma [5].

A rough indication of the effect of the nuclear medium on R_{att} can be obtained from an estimate of the formation time τ_f, which is the time between the initial hard scattering and the moment at which the hadron is formed. In e^+e^--experiments at CERN it was found that the energy gradient contained by the color field of two quarks is about 1 GeV/fm (i.e. the string constant, κ). As an order of magnitude estimate for the formation length ($l_f = \tau_f c$) it can therefore be estimated that $l_f \approx \nu/\kappa$.

For HERMES energies ($4 < \nu < 24$ GeV) nuclear effects may be significant [6] since the formation length is of the same order of magnitude as the diameter of the target nucleus (^{14}N $\approx$ 6 fm). The energies used in deep-inelastic muon scattering experiments at CERN ($20 < \nu < 200$ GeV) [7] lead to formation times as large as 20-200 fm/c. As a result, the formation process takes place largely outside the nucleus. The attenuation ratio is therefore expected to be close to unity for the high ν values produced at CERN. Hence, in order to observe significant nuclear effects in hadron formation, one should perform studies at an intermediate energy experiment, such as HERMES.

The measurement of the attenuation ratio at HERMES is the second experimental result described in this thesis. Values of R_{att} are determined for pions and hadrons separately, as a function of ν, and other kinematic variables. The experimental results are compared to both phenomenological descriptions and a gluon bremsstrahlung model [8]. The models for hadron attenuation do not distinguish between the formation of mesons and baryons. The HERMES results, however, show a larger attenuation ratio for negative hadrons than for positive hadrons. Since the baryon contribution is larger in the positive hadron sample than in the negative hadron sample, this difference may represent evidence of a significantly longer formation time for a baryon than for a meson.

The thesis is organized as follows. In chapter 2 the formalism for DIS is introduced. The HERMES spectrometer is briefly described in chapter 3, while a somewhat more detailed account of the HERMES Vertex Chamber is given in chapter 4. The extraction of the results on the A-dependence of R

and on the hadron attenuation are presented in chapters 5 and 6, respectively. The conclusions concerning the two subjects are summarized in the final chapter.

Chapter 2

Deep-Inelastic Scattering

In deep-inelastic scattering a lepton is scattered off a quark in a nucleon, resulting in the production of a number of hadrons. Experimentally, the scattered lepton and hadrons can be detected by the particle detectors, making up the spectrometer.

Deep-inelastic scattering (DIS) involves two distinct processes. The interaction of the lepton with the constituents of the nucleon is a hard scattering process which can be studied by detecting the scattered lepton only. This is known as inclusive DIS. In a second process the final hadrons are formed which can be studied in semi-inclusive DIS, involving the detection of part of the hadronic final state.

This chapter is organized as follows. In the first section the kinematics and cross section formalism of inclusive DIS are presented. The formalism is extended to semi-inclusive processes, including a discussion of hadron formation, in section 2.2. In both cases the effect of the nuclear medium on the reaction is discussed as well.

2.1 Formalism for deep inelastic scattering

In deep-inelastic scattering the lepton interacts with the constituents of the nucleon by the exchange of a virtual photon. A virtual photon differs from a real photon since its energy is not equal to its momentum. As a result the momentum and energy transfer to the nucleon constituents can be independently varied.

2.1.1 Kinematics

The DIS process in the target rest frame (i.e. laboratory frame) is shown schematically in figure 2.1.

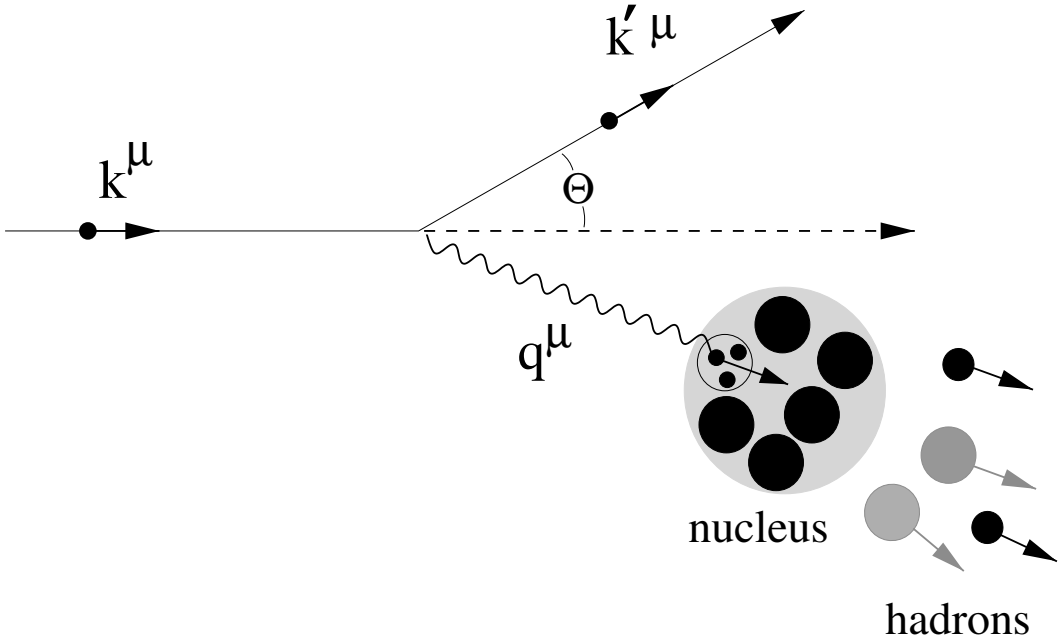

Figure 2.1: Schematic view of a deep-inelastic scattering event. The scattering angle (Θ) is the angle between the incident and scattered lepton.

With k^μ (k'^μ) the momentum 4-vector of the incident (scattered) electron, the 4-vector q^μ of the virtual photon equals:

$$q^\mu \equiv k^\mu - k'^\mu. \tag{2.1}$$

The energy transfer (ν) of the virtual photon to the target nucleon can be evaluated from the momentum 4-vector (p^μ) and the rest mass (M) of the target nucleon

$$\nu \equiv \frac{p^\mu q_\mu}{M} = E - E', \tag{2.2}$$

with E and E' the energy of the incident and scattered lepton, respectively.

The interaction kinematics (using units with $c = \hbar = 1$) are described by the Lorentz scalars Q^2, W^2, x, and y. Using the definitions of these Lorentz scalars given below, the expressions are also given in the laboratory reference frame. The scalar Q^2 is defined as

$$-Q^2 \equiv (q^\mu q_\mu) = 4EE' sin^2(\frac{\Theta}{2}), \tag{2.3}$$

and represents minus the squared invariant mass of the virtual photon.

The quantity W^2 is defined as

$$W^2 \equiv (p^\mu + q^\mu)^2 = M^2 + 2M\nu - Q^2, \tag{2.4}$$

and represents the total invariant mass squared in the virtual-photon nucleon system.

The two variables x and y are dimensionless, range between zero and unity, and are defined as

$$x \equiv \frac{q^\mu q_\mu}{2(p^\mu q_\mu)} = \frac{Q^2}{2M\nu} \tag{2.5}$$

and

$$y \equiv \frac{p^\mu q_\mu}{p^\mu k_\mu} = \frac{\nu}{E}, \tag{2.6}$$

where x represents, as shown in subsection 2.1.3, the nucleon momentum fraction of the struck quark, and y represents the energy fraction of the virtual photon.

The scalars W^2, x, and y are not independent. Hence, any combination of two of these scalars determines, for a given beam energy, the kinematics of the interaction.

The dimensionless variable z, used to describe the final state, is defined as

$$z \equiv \frac{p^\mu p^h_\mu}{p^\mu q_\mu} = \frac{E_h}{\nu}, \tag{2.7}$$

with $p^h_\mu = (E_h, \mathbf{p}^h)$ the 4-vector of the formed hadron. The variable z represents the fraction of the photon energy ν transfered to hadron h.

2.1.2 DIS Cross section

The differential cross section for deep-inelastic lepton scattering equals

$$\frac{d\sigma}{dE'd\Omega} = \frac{\alpha^2}{Q^4}\frac{E'}{E}\mathcal{L}^{\mu\nu}\mathcal{W}_{\mu\nu}, \tag{2.8}$$

with α the fine structure constant. The leptonic tensor $\mathcal{L}^{\mu\nu}$ can be calculated exactly in quantum electrodynamics (QED), while the hadronic tensor $\mathcal{W}_{\mu\nu}$ has to be parametrized since the structure of the hadron cannot be calculated in pQCD. The differential cross section can be written [9] (laboratory frame) as

$$\frac{d\sigma}{dE'd\Omega} = \frac{4\pi\alpha^2}{Q^4}\left[y^2F_1 + \frac{1}{x}\{1 - y - \frac{Mxy}{2E}\}F_2\right] \tag{2.9}$$

Where the dimensionless structure functions $F_1(x, Q^2)$ and $F_2(x, Q^2)$ describe the structure of the nucleon.

In terms of the cross section for the absorption of transversely and longitudinally polarized virtual photons, Eq. (2.8) can be written [9] as

$$\frac{d\sigma}{dE'd\Omega} = \Gamma(\sigma_T + \epsilon\sigma_L), \tag{2.10}$$

with $\sigma_T(Q^2, \nu)$ and $\sigma_L(Q^2, \nu)$ the transverse and longitudinal virtual photon absorption cross section, respectively. The virtual photon flux Γ equals,

$$\Gamma = \frac{\alpha(\nu - Q^2/2M)}{2\pi^2Q^2}\frac{E'}{E}\frac{1}{1-\epsilon}\ , \tag{2.11}$$

with ϵ the virtual photon polarization parameter,

$$\epsilon = \frac{4(1-y) - \frac{Q^2}{E^2}}{4(1-y) + 2y^2 + \frac{Q^2}{E^2}}. \tag{2.12}$$

The cross sections $\sigma_T(Q^2, \nu)$ and $\sigma_L(Q^2, \nu)$ are related to $F_1(Q^2, x)$ and $F_2(Q^2, x)$ as follows,

$$\sigma_T = \frac{4\pi^2\alpha}{KM}F_1 \ , \tag{2.13}$$

and

$$\sigma_L = \frac{4\pi^2\alpha}{K\nu M}\left[(1+\frac{\nu^2}{Q^2})MF_2 - \nu F_1\right] = \frac{4\pi^2\alpha}{KM}\frac{1}{2x}F_L \ , \tag{2.14}$$

with

$$K = \frac{2M\nu - Q^2}{2M}. \tag{2.15}$$

The right hand side of Eq. (2.14) implicitly defines the longitudinal structure function F_L in terms of F_1 and F_2.

The DIS cross section can be expressed in terms of $R = \sigma_L/\sigma_T$ and F_2 as well. The derivation is straight forward, as shown in appendix A. The resulting equation is given here,

$$\frac{d\sigma(x,Q^2,\epsilon)}{dE'd\Omega} = \sigma_{mott}\frac{2MxF_2}{Q^2\epsilon}\left(\frac{1+\epsilon R}{1+R}\right). \tag{2.16}$$

The Mott-cross section σ_{mott} represents the cross section for scattering off a point charge (with unity charge) and equals,

$$\sigma_{mott} = \frac{4\alpha^2 E'^2}{Q^4}cos^2(\frac{\Theta}{2}), \tag{2.17}$$

where Θ represents the scattering angle (figure 2.1).

For $R = \sigma_L/\sigma_T$ it follows from Eq. (2.13) and (2.14) that

$$R = \frac{F_L}{2xF_1}, \tag{2.18}$$

i.e. it also represents the ratio of the longitudinal and transverse structure functions. The structure functions F_1 and F_2 can be expressed in terms of σ_L and σ_T, which is useful for future reference:

$$F_1 = \frac{MK}{4\pi^2\alpha}\sigma_T \tag{2.19}$$

and

$$F_2 = \frac{MK}{4\pi^2\alpha}\frac{\nu}{(M+\nu/2x)}\left(\sigma_L + \sigma_T\right). \tag{2.20}$$

2.1.3 Quark Parton Model

In this section the hard scattering of the lepton with the nucleon constituents is discussed in terms of the Quark Parton Model (QPM). In the QPM a quark is considered to be a structureless point particle with spin $\frac{1}{2}$. The structure functions F_1 and F_2 can then be written [9] as a sum over all quark flavors

$$F_2(x) = \sum_f e_f^2 x q_f(x) \tag{2.21}$$

and

$$F_1(x) = \frac{1}{2x}F_2(x), \tag{2.22}$$

with $q_f(x)$ the momentum distribution of a quark with flavor f and e_f the charge of the quark in units of the electron charge. The dimensionless variable x can be interpreted in the infinite momentum frame as the momentum fraction of the parton which absorbed the virtual photon. It is noted that the structure functions only depend on x, and not on ν and Q^2 separately. This behavior is referred to as Bjorken scaling. Increasing the spatial resolution of the scattering process by increasing Q^2 (uncertainty principle) leaves the structure functions unchanged, because the quarks are assumed to be point particles in the QPM. The scaling behavior is globally confirmed experimentally. However, when the Q^2-dependence of $F_2(x)$ is studied in

detail, violations of Bjorken scaling are observed. These are understood in QCD in terms of gluon emission. QCD predicts that at increasing resolution (increasing Q^2) we should find that the quarks are surrounded by a cloud of gluons, and other quarks. At low x the structure function F_2 increases with Q^2, since more partons with a low momentum fraction are observed at higher values of Q^2. At high x, the structure function F_2 decreases since less partons with a high momentum fraction are observed when increasing Q^2. This Q^2-dependence is calculable within QCD, and when the structure functions are known for a certain value of Q^2, they can be evolved to other Q^2 values using the Altarelli-Parisi equations [10].

Going to low values of Q^2 the resolution decreases. The lower Q^2 limit at which the QPM is still applicable is not exactly known. Generally a value of 1 GeV^2 is assured, which corresponds to a spatial resolution of about 0.2 fm. However, comparison of experimental data to QCD analyses [11] suggests that Q^2 evolutions work well for Q^2 values as low as 0.3 GeV^2. When such low values of Q^2 are combined with high values of the energy transfer ν the spatial resolution is small. However, the interaction time is short (uncertainty principle) and it is still possible to interpret the scattering process as scattering from a free quark. For lower Q^2 values higher twist effects, i.e. quark-gluon correlations, may be important [1].

2.1.4 Nuclear effects

In 1982 the EMC experiment at CERN found unexpectedly that the structure function F_2 depends on the nuclear mass (A) of the target. The influence of the surrounding nucleons was assumed to be negligible in DIS, as the energies involved (several GeVs) are much higher than those relevant for nuclei (several MeVs).

The F_2 structure function can be expressed in terms of the longitudinal and transverse virtual photon absorption cross sections, σ_L and σ_T (see Eq. (2.20)). With F_2 found to be A-dependent, it is interesting to see if there

[1] For Q^2 larger than 1 GeV^2 a QCD analysis from U.K. Yang and A. Bodek [12] suggests that significant higher twist effects (implemented by $1/Q^2$ and $1/Q^4$ corrections [13]) are needed in a next to leading order (NLO) calculation of F_2 and R in order to describe the experimental data on a proton and deuterium target. However, it was shown by the same authors that in a NNLO calculation these higher twist effects do not need to be included [14].

is a difference in the A-dependence of σ_L and σ_T. A possible difference in the A-dependence of these two components can be studied by investigating the A-dependence of R, which is the ratio of the longitudinal and transverse virtual photon absorption cross sections, i.e. $R = \sigma_L/\sigma_T$.

Information on the A-dependence of the longitudinal and transverse component separately, may help in understanding the A-dependence of F_2 better. Furthermore it is expected that the longitudinal component is sensitive to higher twist effects [3].

In the remaining part of this subsection the available measurements of the A-dependence of F_2 and R are briefly reviewed. Using the experimental observations, the models describing or suggesting such an A-dependence are discussed as well.

The F_2 structure function in nuclei

A study of the influence of the nuclear mass on DIS involves measurements of the ratio of the cross section for a nucleus A and deuterium (D). Deuterium is a suitable reference target since its isospin (I) equals zero. For targets which have non-zero isospin the ratio σ_A/σ_D is corrected by making use of the measured cross section ratio σ_D/σ_{1_H}. For ^{3}He, the ratio $\sigma_{3_{He}}/(\sigma_{1_H} + \sigma_D)$ is determined in order to correct for the non-zero isospin.

After the correction for $I \neq 0$ a simple relation applies for the nucleon cross section ratio of deep inelastic scattering on targets with atomic mass A (at HERMES ^{3}He or ^{14}N) and 2 (i.e. a D target),

$$\frac{\sigma_A}{\sigma_D} = \frac{F_2^A}{F_2^D} \frac{(1 + \epsilon R_A)(1 + R_D)}{(1 + R_A)(1 + \epsilon R_D)}. \tag{2.23}$$

If either $\epsilon = 1$ or $R_D = R_A$, the cross section ratio is equal to the structure function ratio.

The EMC experiment was the first to report an A-dependence of σ_A/σ_D at high Q^2, using high energy muon beams [1]. Because of the high energy used most data were collected for $\epsilon > 0.9$. Moreover, explicit measurements of a possible A-dependence of R indicated that $R_A = R_D$. Therefore, these data can be presented in terms of the A-dependence of F_2^A/F_2^D. The results for the structure function ratio of carbon and deuterium from NMC [15], SLAC [16], and E665 [17], are shown in figure 2.2.

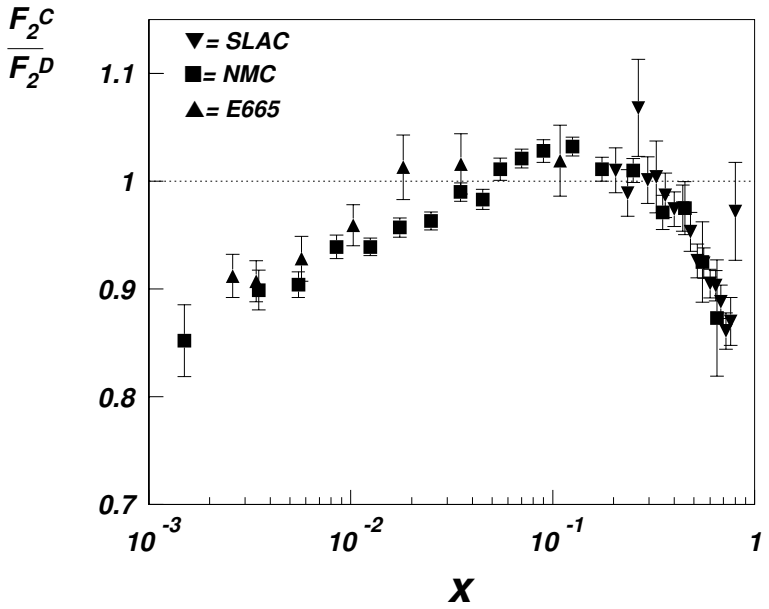

Figure 2.2: The x-dependence of the ratio of structure functions F_2 for ^{12}C and D. The error bars include the statistical and systematic error summed quadratically.

From figure 2.2 it can be seen that the size and sign of the deviation of F_2^A with respect to F_2^D is x-dependent. In the high x-region ($x \gtrapprox 0.2$) the A-dependence of F_2 is known as the *EMC-effect*, while in the low ($x \lessapprox 0.05$) x-region the effect is referred to as *shadowing*.

Apart from the x-dependence of the structure function ratios, also the Q^2-dependence has been studied. The NMC results [15] show no Q^2-dependence of the structure function ratios He/D, C/D and Ca/D for the explored x and Q^2 range, i.e. $0.0035 < x < 0.60$ with $0.60 < Q^2 < 41$ GeV^2.

Several models exists that are able to describe the shadowing data. These are mostly based on the vector meson dominance (VMD) model. In the models based on VMD, the virtual photon fluctuates in a $q\bar{q}$-pair (i.e. vector mesons ρ, ϕ, ω, and higher mass states). The cross section for interactions of the hadronic component of the photon with the target nucleon depends on the longitudinal propagation length (l_c) and the transverse size ($l_\perp$) of the hadronic state. These are given by [18],

$$l_{coh} = \frac{2\nu}{M_{q\bar{q}} + Q^2}, \tag{2.24}$$

with $M_{q\bar{q}}$ the invariant mass of the virtual hadronic state, and

$$l_{\perp} \propto \sqrt{\frac{1}{Q^2}}. \tag{2.25}$$

Because the hadronic interaction is much stronger than the electromagnetic interaction, the $q\bar{q}$-pair will only see the outer nucleons of the nucleus. The inner nucleons are thus in the shadow of the outer ones, reducing at low Q^2 the cross section per nucleon (i.e. shadowing). At high Q^2 the longitudinal propagation length l_{coh} equals approximately $2\nu/Q^2 = 1/2Mx$, showing that l_{coh} is large at low x. In other words the interaction cross section of the hadronic component of the virtual photon is largest at low x, where shadowing is indeed most prominent.

The higher x-region (*EMC-effect*) is described by a large number of models which are generally based on a modified nuclear potential or a modified quark confinement size, both resulting in an enhanced parton momentum distribution at low x and a reduced momentum distribution at high x. In general a reasonable description of the data is obtained in this way.

An overview of models and experimental data until 1994, for the shadowing region and the EMC-effect, can be found in ref. [2].

The ratio $R = \sigma_L/\sigma_T$ in nuclei

It is seen from Eq. (2.20) that F_2 contains both a longitudinal and a transverse component. Since F_2 is found to be A-dependent, the question arises whether σ_L and σ_T have the same A-dependence. This can be investigated by studying the A-dependence of $R = \sigma_L/\sigma_T$.

In the QPM the value of R is zero. This follows from helicity conservation and the fact that quarks are spin $\frac{1}{2}$ particles. Helicity (h) conservation demands that, for example in the Breit frame, the helicity of the quark is conserved. Since the quark has spin $\frac{1}{2}$ and σ_L involves no helicity flip, σ_L is zero in the QPM, while σ_T requires a helicity flip and can thus obtain a

non-zero value. This corresponds to R=0. However, this is only exactly true at $Q^2 \to \infty$, and R may have a non-zero value at lower values of Q^2.

In the case of spin-0 partons R could be large, since helicity conservation of the quark demands that $\sigma_T(h = \pm 1) = 0$, while $\sigma_L(h = 0) \neq 0$. Thus R is sensitive to spin-0 (or spin-1) constituents in the nucleon.

The quantity R has been determined experimentally with reasonable precision at medium values of x ($0.05 < x < 0.10$). The value of R is about 0.35 ± 0.05 at $Q^2 \approx 1$ GeV^2 and is consistent with zero at Q^2 values of about 20 GeV^2. The world data on R [19] are shown in figure 2.3. Figure 2.3 shows an abundance of data in the high x-region (a: $0.05 < x < 0.10$), while not very much data are available in the low x-region (c: $0.01 < x < 0.02$). The data are mainly collected on hydrogen and deuterium targets. However, also measurements on carbon, iron and beryllium are shown.

Different mechanisms for an A-dependence of R have been proposed. According to reference [3] F_L is a function of the transverse (with respect to the virtual photon) momentum of the quarks in a nucleon, while in reference [20] it is suggested that the transverse momentum of the quarks in a nucleon may be enhanced when the nucleon resides in a nucleus. Alternatively, it has been shown [21] that an enhanced gluon distribution in nuclei would lead, for leading twist, to R_{Sn} about 10% larger than R_C. An other different mechanism that would lead to an A-dependence of R is a possible difference in nuclear shadowing for longitudinally and transversely polarized photons [22]. It was shown [23] that such an effect is expected to be smaller than 50%.

In figure 2.4 measurements of $\Delta R = R_{A_1} - R_{A_2}$ for different nuclear targets A_1 and A_2 are shown. The precision of the experiments is not very good as it is a measurement of a difference. For the kinematic region explored by the existing experiments it is concluded that no significant A-dependence of R has been found. As a consequence, the quoted mechanisms that can give rise to an A-dependence of R have received relatively little attention in the literature.

The region with $0.3 < Q^2 < 1$ GeV^2, which is accessible at the HERMES experiment, has not yet been explored by other experiments. Cross section ratio measurements (σ_A/σ_D) have been carried out in this domain at DESY [24], Daresbury [25], Cornell [26], SLAC [27] and FNAL [28], but these data have not been used to study a possible A-dependence of R.

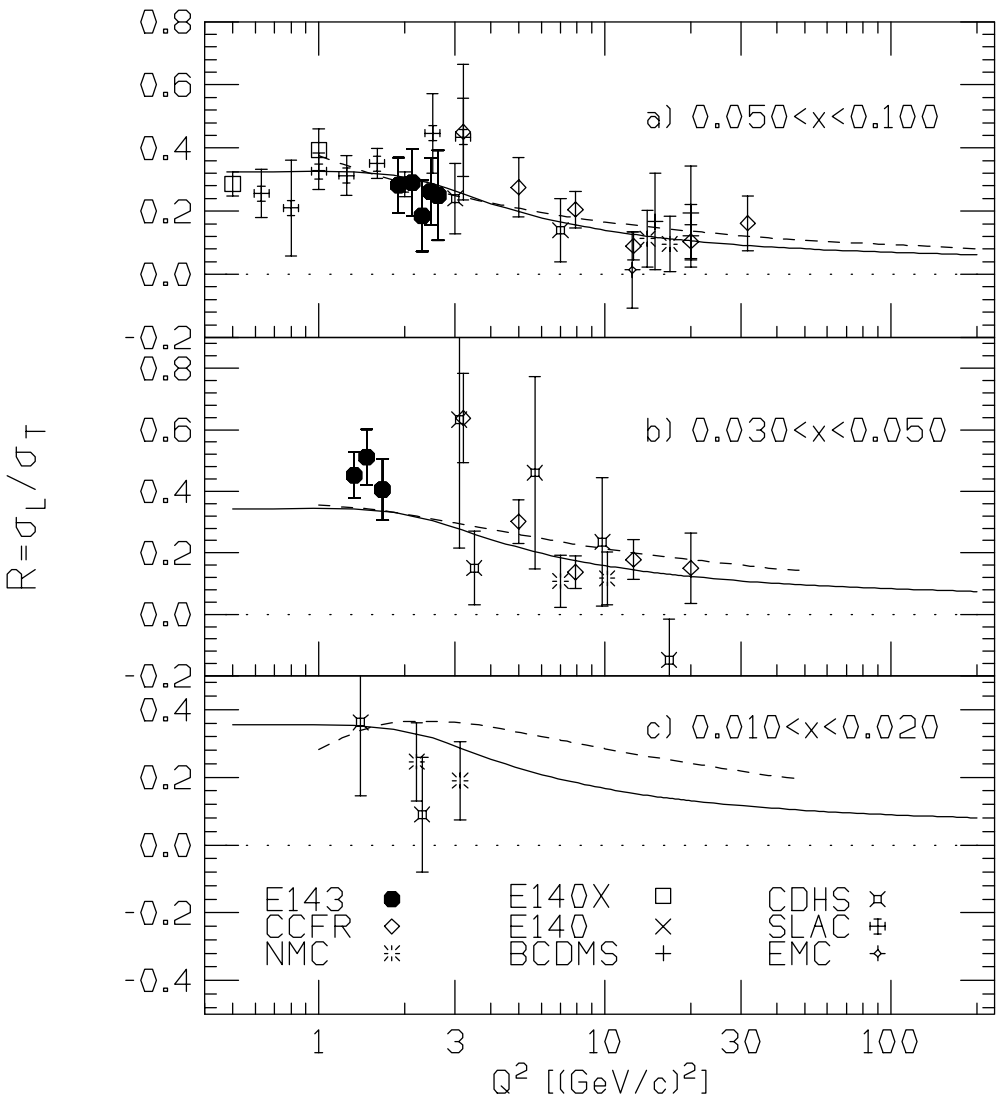

Figure 2.3: R as a function of Q^2 for three x-regions, a: $0.05 < x < 0.10$, b: $0.03 < x < 0.05$, and c: $0.01 < x < 0.02$. The solid curve represents the R1998 parametrization, while the dashed curve is a NNLO pQCD calculation (the figure is reprinted from Physics Letters, B452, K. Abe et al., *Measurements of* $R = \sigma_L/\sigma_T$ *for* $0.03 < x < 0.1$ *and Fit to World Data*, 194, 1999, with permission of Elsevier Science).

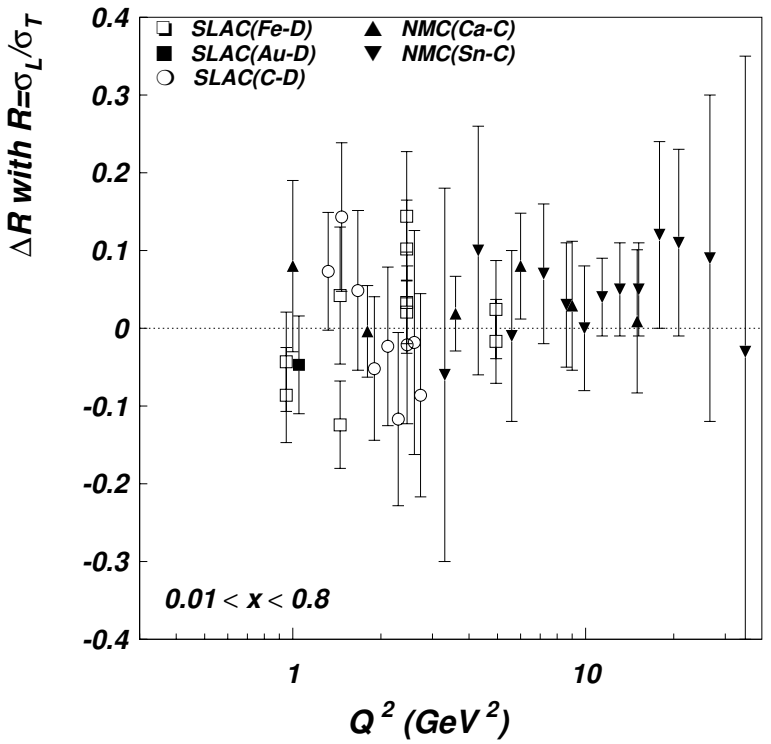

Figure 2.4: The world data [29, 30, 31] on the A-dependence of R. The difference of R for different nuclear targets is shown as a function of Q^2.

2.2 Formation of the final state

The quark, which obtains a large momentum in the initial hard scattering process by the absorption of a virtual photon, is a colored particle. The particles which we observe in our particle detectors are colorless and real (i.e. they satisfy the relation $E^2 = p^2 + m^2$). As mentioned earlier, pQCD cannot be used to calculate this hadronization process. Therefore, phenomenological models are used to calculate the probability to form a certain hadron in DIS [34]. However, as the experimental data presented in this thesis focus on hadronization in a nuclear environment, the emphasis in this section is on models describing how the nuclear environment affects the hadronization process. First the framework of semi-inclusive DIS is presented.

2.2.1 Semi-inclusive DIS cross section

The cross section for the formation of a hadron (h) in semi-inclusive DIS reads

$$\frac{d\sigma(eN \to hX)}{dz} = \sum_f \sigma(eN \to q_f X) D_f^h(z), \tag{2.26}$$

where the sum extends over all quark flavors f, $D_f^h(z)$ is the fragmentation function, and q represents the quark which absorbed the virtual photon. The probability to create a hadron h in the interval $(z, z+dz)$, when a quark of flavor f has absorbed the virtual photon, equals $D_f^h(z)dz$. The fragmentation functions cannot be calculated in pQCD and are determined experimentally. In Eq. (2.26) the hadron formation process is separated from the initial hard scattering, i.e. factorization is assumed. It is noted, though, that D_f^h is known to have a weak Q^2-dependence as it is the subject to the same scaling violations that were described in section 2.1.3, in relation to the inclusive structure functions. The Q^2-dependence of D_f^h is also calculable in QCD.

Within the QPM Eq. (2.26) can be expressed in terms of the quark distribution functions $q_f(x)$, which were introduced in Eq. (2.21), using Eqs. (2.9) and (2.21):

$$\frac{1}{\sigma}\frac{d\sigma(eN \to hX)}{dz} = \frac{\sum_f e_f^2 q_f(x) D_f^h(z)}{\sum_f e_f^2 q_f(x)}, \tag{2.27}$$

with e_f the electric charge of the quark. In this equation σ is the (inclusive) DIS cross section. Note that Eq. (2.27) actually represents a multiplicity distribution, i.e. represents the number of hadrons (in a given z-bin) per DIS event.

2.2.2 Hadronization in the nuclear medium

The quantity which is measured in the experiment is the attenuation ratio R_{att}, defined as the ratio of the number of hadrons per DIS event for a target with nuclear mass A and a deuterium target:

$$R_{att}(z,\nu) \equiv \frac{\frac{1}{N_e^A}\left(\frac{dN^h}{dzd\nu}\right)_A}{\frac{1}{N_e^D}\left(\frac{dN^h}{dzd\nu}\right)_D}, \tag{2.28}$$

with N^h the number of formed hadrons in the (x,Q^2)-range corresponding to a certain (ν,z)-bin, and N_e the total number of DIS events for the same (x,Q^2)-range. The attenuation ratio is usually studied as a function of ν or z. However, a dependence on x, Q^2 and p_t is also possible.

It is noted that the ratio N_e^A/N_e^D is a function of x, corresponding to the A-dependence of the structure function as discussed in section 2.1.4. This x-dependence affects the z and ν-dependence of $\frac{dN^h}{dzd\nu}$, since the x-range corresponding to the separate (z,ν)-bins is not the same. It is important to separate the A-dependence of the inclusive DIS cross section and the A-dependence of the hadron formation process, which originate presumably from different mechanisms. For that reason $R_{att}(z,\nu)$ is evaluated as a double ratio, i.e. the ratio of produced hadrons normalized by the inclusive ratio N_e^A/N_e^D. Below, we show that this choice effectively corrects for the A-dependence of the inclusive DIS cross section ratio.

With Eq. (2.27), it follows that, for a given (z,ν) and (x,Q^2) domain:

$$R_{att} = \frac{(\frac{1}{\sigma}\frac{d\sigma(eN\to hX)}{dz})_A}{(\frac{1}{\sigma}\frac{d\sigma(eN\to hX)}{dz})_D} = \frac{(\frac{\sum_f e_f^2 q_f(x) D_f^h}{\sum_f e_f^2 q_f(x)})_A}{(\frac{\sum_f e_f^2 q_f(x) D_f^h}{\sum_f e_f^2 q_f(x)})_D}. \tag{2.29}$$

Hence, if it is assumed that the virtual photon γ^* is mainly absorbed by a given quark flavor (such as the dominant u quarks), the attenuation ratio equals the fragmentation function ratio,

$$R_{att} = \frac{\left(D_u^h(z)\right)_A}{\left(D_u^h(z)\right)_D}. \tag{2.30}$$

In other words, R_{att} plays the same role in semi-inclusive DIS as the F_2-ratio in inclusive DIS.

For hadrons which carry a small fraction (z) of the virtual photon energy, R_{att} can be larger than unity due to rescattering processes of the final hadrons and pion production. These processes do not supply information on the formation of hadrons in DIS fragmentation. For hadrons with a larger energy fraction R_{att} is smaller than unity due to interactions between the quark and final hadron and the nuclear medium. In order to investigate the hadron formation process, hadrons with a relatively high energy fraction z should be used. However, the value for this z-cut is not known apriori, and is often chosen on basis of experimental constraints such as the energy acceptance and the number of events.

By studying the attenuation ratio as a function of ν and z information on the time scales involved in hadron formation can be obtained. In figure 2.5 the formation time (τ_f), i.e. the time between the initial γ^*-quark interaction and the moment when the hadron has been formed, is indicated.

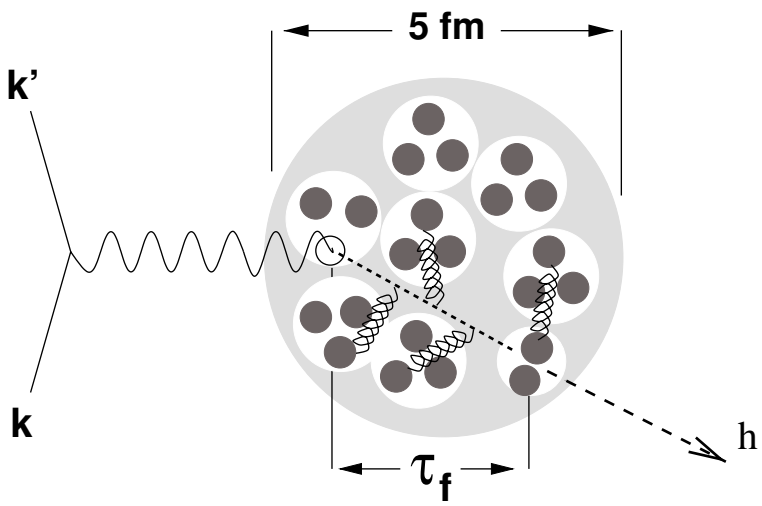

Figure 2.5: Pictorial representation of the formation of a hadron in the nuclear environment.

In the remainder of this subsection R_{att} is related to τ_f, using models with one or two time scales. One-time scale models have been described, for example, by Bialas and Chimay [32], while two-time scale models were combined with the string model by Bialas and Gyulassy in ref. [33]. Additionally

the gluon bremsstrahlung model, developed by Kopeliovich and Nemchek [8], is described. This model allows the evaluation of R_{att} for leading hadrons.

One-time scale model

The first model which we discuss contains only one time scale as shown in figure 2.6. There are two cross sections involved in the interaction with the nuclear environment, σ_h is the (measured) cross section of the formed hadron with the nuclear medium, and σ_s is the unknown cross section of the hadron constituents interacting with the nuclear environment before the hadron is formed.

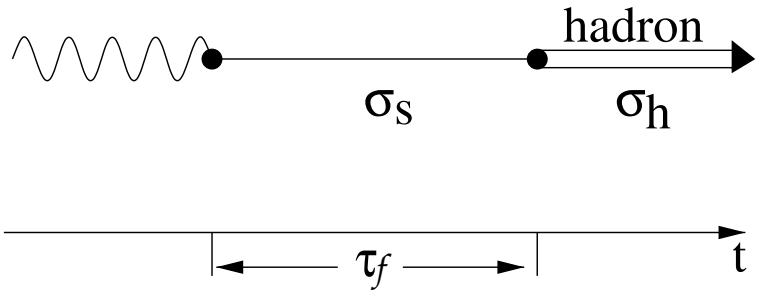

Figure 2.6: The relevant time scale is τ_f, the formation time of the hadron. The cross sections σ_s and σ_h are the cross sections of the hadron constituents and the final hadron with the nuclear environment, respectively.

The probability that neither the quark (q) nor the hadron (h) interacts with the nucleus is represented by the survival probability S_A:

$$S_A(b,l) = 1 - \sigma_s \int_l^\infty dl' \rho_A(b,l') P_q(l'-l) - \sigma_h \int_l^\infty dl' \rho_A(b,l') P_h(l'-l). \tag{2.31}$$

In this expression, the variable b is the impact parameter, l is the position in the direction of the incident quark and ρ_A is the nuclear density, normalized to unity.
The functions $P_q(l'-l)$ and $P_h(l'-l)$ represent the probability that a quark or hadron exists after traversing a distance $(l'-l)$ in the nucleus. If τ_f is interpreted as the lifetime of q, $P_q(l'-l)$ can be expressed as (with $l_f = \tau_f c$)

$$P_q(l'-l) = e^{-(l'-l)/l_f} = 1 - P_h(l'-l). \tag{2.32}$$

For τ_f a choice has to be made. It is either characteristic of the hadron (τ_h) or of the quark (τ_q). In each case it has to be multiplied by the Lorentz factor $\frac{E_h}{m_h}$ or $\frac{E_q}{m_q}$, respectively. Thus,

$$\tau_f = \tau_h \frac{E_h}{m_h} = \tau_h \frac{z\nu}{m_h}, \tag{2.33}$$

or

$$\tau_f = \tau_q \frac{E_q}{m_q} = \tau_q \frac{\nu}{m_q}, \tag{2.34}$$

where the masses m_h and m_q represent the mass of the final hadron and the quark, respectively. It is not clear, however, what mass for the quark should be taken, the effective mass of the quark bounded in the nucleon (the constituent quark mass, i.e. ≈ 0.3 GeV) or the so called 'current quark mass' (2-15 MeV).

The attenuation ratio can be evaluated by integrating the survival probability S_A over all values of b and l that can be reached in a given nucleus:

$$R_{att} = 2\pi \int_0^\infty bdb \int_{-\infty}^\infty dl \rho_A(b,l)[S_A(b,l)]^{A-1}. \tag{2.35}$$

The exponent $A-1$ arises since interactions of the quark or hadron may take place with each of the remaining $A-1$ nucleons. By evaluating Eq. (2.35) with τ_h (or τ_q) and σ_s as free parameters one can use measurements of R_{att} to obtain information on the hadron formation times.

Two-time scale model

Since a hadron contains at least two constituents, which are not necessarily created at the same time, actually two time scales may be involved (figure 2.7).

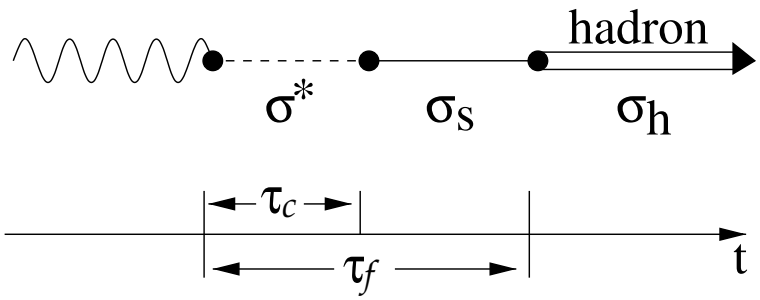

Figure 2.7: The relevant time scales in the two time scale model are the formation time τ_f and the constituent time τ_c. The additional cross section σ^* is the cross section of the color field with the medium, before any of the hadron constituents exists.

The different time scales that play a role in this model are illustrated in the space-time diagram of the hadronization process (figure 2.8)), which is based on the color string model [34]. It is shown for an e^+e^- experiment, however there is no fundamental difference with the DIS case, where the string stretches between the quark which has absorbed the virtual photon and the remaining constituents of the target nucleon. The figure depicts the separation of the initial $q\bar{q}$-pair and the appearance of new $q\bar{q}$-pair pairs from the vacuum. These pairs form colorless states which develop (i.e. building up mass) into hadrons. The times τ_c and τ_f, or equivalently the length scales l_c and l_f, represent the time elapsed between the initial quark-virtual photon interaction and the appearance of the first and second constituent of the formed hadron, respectively. The detected hadron is shown in black in figure 2.8.

Introducing a second time scale, requires the introduction of a third cross section (σ^*). This cross section represent the interaction of the initial color string with the nuclear medium before the quarks making up the final hadron have appeared.

The two time scales τ_c and τ_f are not independent as can be seen from figure 2.8. The energy of the formed hadron ($E_h = z\nu$) must already be contained by the string between τ_c and τ_f. As the energy of a string depends on the string constant $\kappa \approx 1$ GeV/fm and the stretching of the string, a simple relation can be written down:

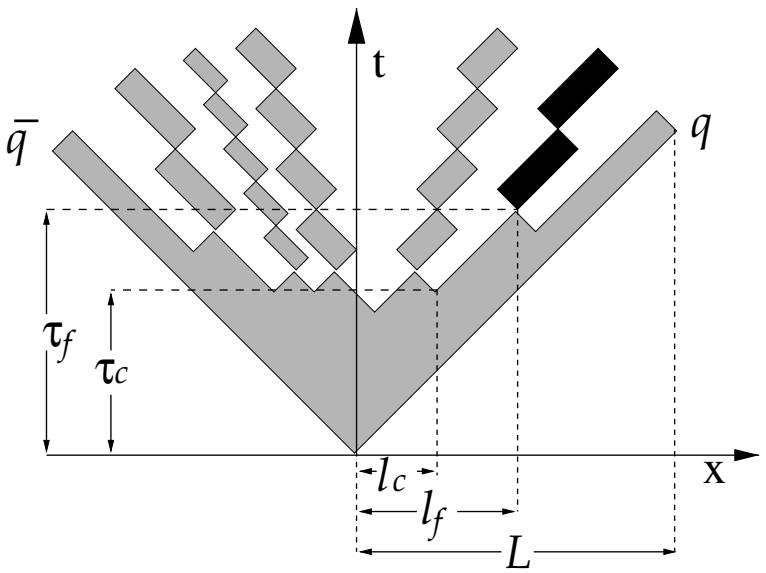

Figure 2.8: The hadronization process of a $q\bar{q}$ pair, leading to the formation of two jets of hadrons. The times τ_c and τ_f, or equivalently the length scales l_c and l_f, represent the time between the initial interaction and the appearance of the first and second constituent of the formed hadron (shown in black).

$$l_f - l_c = \frac{z\nu}{\kappa}. \tag{2.36}$$

In this case the expression for S_A involves three integrals, each corresponding to a time period in the hadron formation process:

$$S_A(b,l) = 1 - \sigma^* \int_l^{l_c} dl' \rho_A(b,l') - \sigma_s \int_{l_c}^{l_f} dl' \rho_A(b,l') - \sigma_h \int_{l_f}^{\infty} dl' \rho_A(b,l'). \tag{2.37}$$

Clearly, R_{att} can be obtained in the same way as before using Eq. (2.35). Also in this case the comparison to experimental data can be used to obtain information on the formation time and the various quark-nucleon cross sections.

Gluon Bremsstrahlung model

The model for meson attenuation developed by Kopeliovich and Nemchek [8] is different from the phenomenological models described above, as it uses ingredients from QCD.

The quark which absorbed the virtual photon is considered to be a highly virtual object, which reaches its mass shell by the emission of gluons. The energy loss of the quark in a nuclear environment depends on its energy, and is time dependent. When the energy of the quark has decreased and no more gluons are emitted it combines with a quark or anti-quark from the last emitted gluon, forming a colorless dipole which develops into a final meson, during which time its mass is constructed. Since the quark which has absorbed the virtual photon is always one of the quarks in the final meson, the model concerns the attenuation of leading mesons. The z value for leading mesons is not well defined, but is expected to be relatively high. The authors make predictions on meson attenuation of mesons with $z > 0.5$. A generalization of the model for the formation of three-quark systems is not yet available.

In vacuum, the energy loss of the quark which absorbed the virtual photon is constant, like for a color string ($\kappa = 1$ GeV^2/fm), and proportional to Q^2. The nuclear environment affects meson formation in two ways:

- The final meson interacts with the nuclear environment with a cross section equal to the meson-nucleon cross section (σ_h) of about 25 mb.
- In the nuclear environment the initial quark radiates additional gluons, initiated by interactions of the quark with the nuclear environment. The additional gluon radiation increases the transverse momentum of the initial quark (and the transverse momentum of the final meson) and leads to a faster energy loss, resulting in shorter formation times.

The model of Kopeliovich and Nemchek [8] also includes the following ingredients:

- After combination of the initial quark with the quark (anti-quark) from the last emitted gluon, initially a small sized $q\bar{q}$ pair is formed with a reduced interaction cross section (color transparency). This small sized configuration develops to the final meson, building up it mass and size.

- If a high-z meson is formed the initial quark cannot radiate many gluons. However, a color charge cannot propagate over a long distance in a nuclear environment without radiating gluons. The production of high-z mesons is therefore suppressed in a large nucleus compared to a small nucleus.

The interaction of the final meson with the nuclear environment is the main ingredient leading to meson attenuation. For HERMES kinematics, the combined effect of additional gluon radiation due to the nuclear environment, and the time needed for the development of a small sized configuration into a full sized meson, give rise to 2-3% effects only.

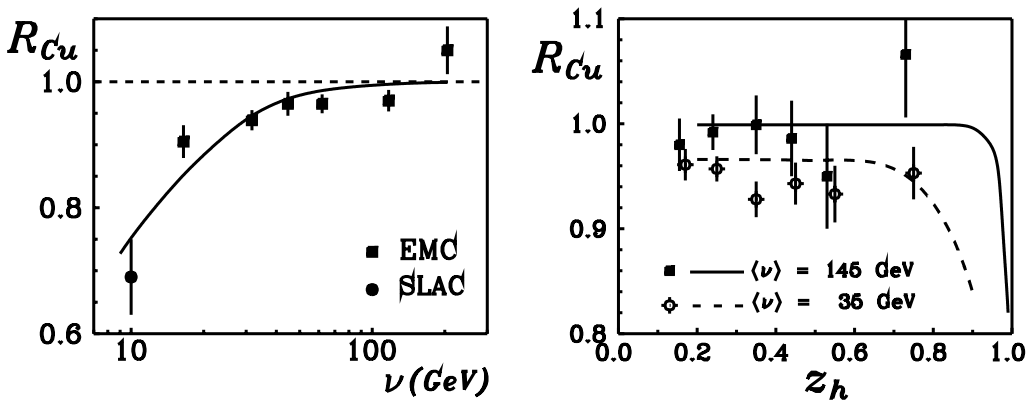

Figure 2.9: The ν and z-dependence of the attenuation ratio. The figure is taken from reference [8]. The experimental data are from SLAC and CERN.

The gluon bremsstrahlung model can, to a certain extent, be compared with a one-time scale model including two cross sections σ_s and σ_h and a formation time τ_f. The formation time in the gluon bremsstrahlung model is roughly equal to the formation time in the one-time scale model. The difference between the two formation times is the additional time needed in the gluon bremsstrahlung model for the development of a small sized configuration into a meson. While σ_h is the same for the two models, the effect of σ_s cannot be compared directly. In the gluon bremsstrahlung model σ_s leads to additional energy loss of the quark due to gluon radiation, while in the one-time scale model σ_s leads to the removal of the quark. However, in both models σ_s is very small (leading to 0-3% effects). The formation times

in the gluon bremsstrahlung model are short for high z mesons (1-3 fm/c at z=0.95 and ν=30 GeV) and long for lower z mesons (4-12 fm/c at z=0.7 and ν=30 GeV), while in the one-time scale model the formation time is either independent of z, or proportional to $z\nu$.

The gluon bremsstrahlung model predicts, for example, the ν and z-dependence of meson attenuation. The predictions of the model are shown in figure 2.9 for a Cu target. It is seen that the attenuation rises with ν. As mentioned earlier this is expected since at high energies the meson formation takes place largely outside the nucleus. The attenuation ratio as a function of z shows a strong decrease at high z values. The decrease sets in at lower values of z, when the energy transfer (ν) is smaller. The experimental data in the figure are from SLAC [35] and EMC [7]. The new experimental data of HERMES presented in chapter 6, enables a more precise assessment of the model because of the improved precision of the data.

Chapter 3

The HERMES experiment

3.1 Introduction

The HERMES (HERA MEasurement of Spin) experiment is located at DESY (Hamburg) and utilizes the polarized HERA electron/positron storage ring. The experiment collects polarized deep inelastic scattering (DIS) data to investigate the spin structure of the nucleon. In addition there is an unpolarized physics program for studying other properties of the nucleon, such as the flavor asymmetry of the sea quarks and hadron formation. These unpolarized data are usually collected in short time periods of a few days or a week at relatively high luminosity (L) conditions ($L \approx 10^{33}$ nucleons/cm^{2}s).

In this chapter the experimental setup is discussed in brief. The storage ring is outlined in section 3.2, and the internal target is the subject of section 3.3. The HERMES spectrometer, of which a more detailed description can be found in reference [36], is presented in section 3.4.

3.2 The HERA storage ring

The HERA storage ring is used to accelerate and store electrons or positrons. At the center of mass energy of the HERMES fixed target experiment the DIS scattering process is the same for both leptons. For the data presented in this thesis, positrons were used. The stored positrons had an energy of 27.5 GeV, and the lifetime of the beam was about 8-12 hours, representing one fill. The beam current ranged from about 35 mA at the beginning of a fill to about 12 mA at the end of a fill. Part of the data taking was carried

out at much shorter beam life times (4 hours) when the target thickness was increased to 6×10^{15} nucleons/cm^2 (see also section 3.3).

3.3 Internal gas target at HERMES

The target [37] consists of a gas, which is injected into the HERA positron beam. The target gas is contained in a storage cell, i.e. a 400 mm long aluminum tube with a height of 9.8 mm and a width of 29 mm. The tube is open on both ends, allowing the positron beam to pass through the cell. The gas flows continuously through the cell, and is pumped out at both ends by a powerful pumping system to avoid that a significant amount of gas enters the region outside the target cell in the HERA beam line.

During the unpolarized studies the target density reached values up to 6×10^{15} nucleons/cm^2. This leads to a luminosity of 1.2×10^{33} nucleons/cm^{2}s at the maximum beam current (32 mA).

The luminosity is measured by detecting the beam positrons which are scattered off the target electrons (Bhabha-scattering). The scattered target electrons are detected in coincidence with the scattered positrons in a pair of $NaBi(WO_4)_2$ electromagnetic calorimeters.

The position of the DIS interaction vertex in the storage cell is defined by two variables relative to the center of the cell, namely z_L in the longitudinal and z_T in transverse direction, constrained by the cell walls. These variables are used in section 5.2.1.

3.4 The HERMES Spectrometer

The forward angle spectrometer has an acceptance between $\pm$ 170 mrad in the horizontal direction θ_x and between $\pm$40 and $\pm$140 mrad in the vertical direction θ_y. The scattering angle, i.e. the polar angle θ, therefore ranges from 40 to 220 mrad.

The spectrometer, shown in figure 3.1, contains a dipole magnet which provides a deflecting power of 1.3 Tm. The gap between the pole faces encloses the full acceptance as described above. Tracking is realized by several sets of position sensitive detectors before, after and inside the dipole magnet (see section 3.4.1). The HERMES spectrometer is also equipped with a set of particle identification detectors, on which more details are given in sec-

tion 3.4.2. The trigger and read-out system are summarized in section 3.4.3, while some performance parameters are presented in the last subsection of this chapter.

3.4.1 Tracking detectors

There are a number of detectors for tracking, namely the vertex chambers (VC), the drift vertex chambers (DVC), the front chambers (FC), the magnet chambers (MC) and the back chambers (BC). The VC is a Micro Strip Gas Counter (MSGC), which is described in more detail in chapter 4. The DVC, FC and BC are drift chambers. Tracks are reconstructed using an efficient tree-search algorithm [45] allowing to combine partial tracks before and after the magnet in several ways. Overall the spectrometer has planes in three different orientations, x (position resolution in the horizontal direction), v and u (which are tilted by $+30^0$ and -30^0 with respect to the vertical direction, in the plane perpendicular to the beamline).

3.4.2 Particle identification

Particle identification is accomplished using a threshold Čerenkov detector (Č), a transition radiation detector (TRD), a pre-shower counter (H2) and an electromagnetic calorimeter (CAL).

The electromagnetic calorimeter consists of two walls, one above and one below the beam line, each containing 420 lead-glass scintillator blocks. Each block is viewed from the rear by a photomultiplier tube. For monitoring the gain of the photomultipliers each one is fed by light pulses from a dye laser through an optical fiber. The light pulses are also measured by a photodiode. Since the gain of the photodiode is stable, the relative gain changes of the photomultipliers can be determined. This gain monitoring system is referred to as GMS.

The pre-shower counter consists of two radiation lengths of lead and a plastic scintillator hodoscope.

The Čerenkov detector contains a gas mixture of 70% nitrogen and 30% perfluorobutane (C_4F_{10}) as radiator. An array of 20 spherical mirrors reflects the Čerenkov light on 20 photomultipliers with photocathodes of 12.7 cm diameter. The photocathode faces are coated with a wavelength shifter (p-terphenyl) to increase the photoelectron yield. The mean number of photo-electrons for a β=1 particle in a pure nitrogen radiator is slightly less than 3.

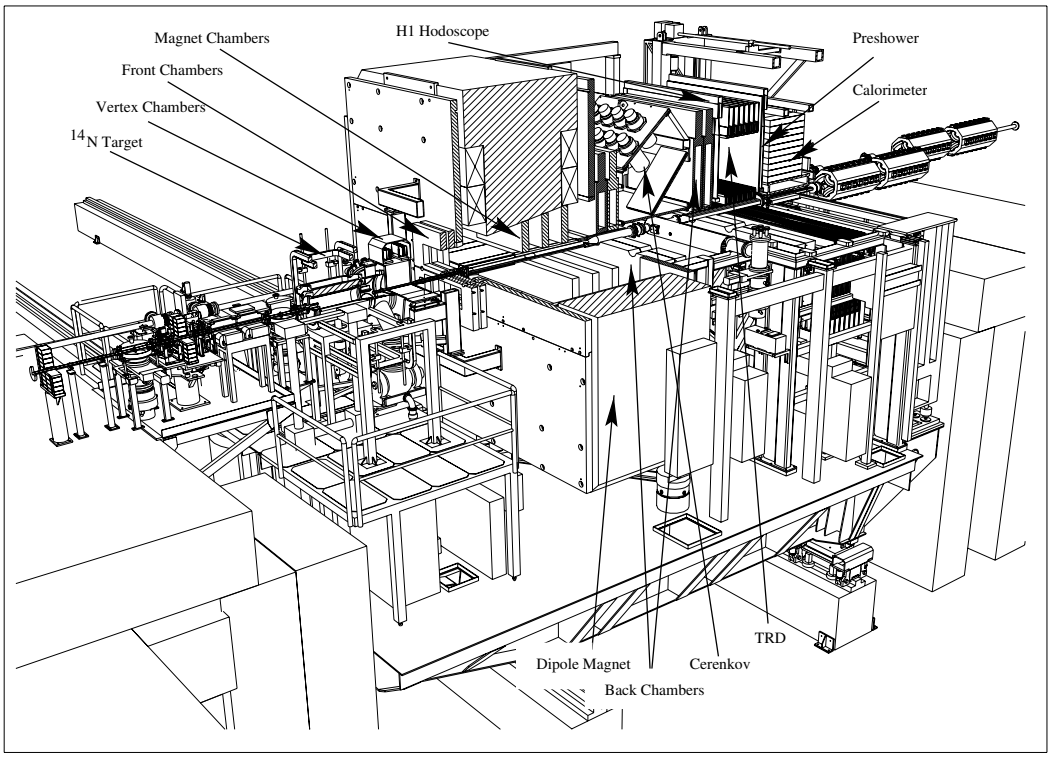

Figure 3.1: The HERMES forward angle spectrometer. It consists of a number of tracking chambers which are described in the text, and several detectors for particle identification. The distance from the target cell on the left to the calorimeter on the right is about 10 meters. The picture has been taken from reference [38].

The transition radiation detector contains 6 modules, each consisting of a radiator (fibers) and a Xe/CH_4 (90:10) filled proportional chamber. In the HERMES energy regime only positrons (or electrons) produce transition radiation in the fibers. The emitted X-rays are detected by the proportional chamber.

Positron-hadron separation is accomplished by combining the signals of the transition radiation detector, Čerenkov detector, calorimeter, and preshower counter. In the HERMES particle identification (PID) scheme usually two quantities are used, namely PID3 and PID5. PID3 is defined as

$$PID3 = log_{10}[(P^e_{cal}P^e_{h2}P^e_{\check{c}})/(P^h_{cal}P^h_{h2}P^h_{\check{c}})] \ ,$$

where P^i_j is the probability that a particle i is produced given a response in detector j. The values for P^i_j are determined for each detector as a function of the momentum from calibration measurements and/or Monte Carlo techniques. PID5 reflects the same probability for the transition radiation detector. In practice, the signals of each PID detector are converted to a probability P^i_j for each event, which thus provide experimental values for PID3 and PID5 on an event by event basis.

Pions can be identified by the Čerenkov detector. The used gas mixture of nitrogen and perfluorobutane makes pion identification possible in the energy range between 4 and 13.5 GeV. A hadron in this energy range with a signal larger than 0.25 photoelectrons is identified as a pion.

3.4.3 Trigger

Positron events are selected by the requirement of a hit in three scintillator hodoscopes (H0, H1 and H2) and an energy deposition of at least 3.5 GeV in two adjacent calorimeter columns. The trigger efficiency is good. Two-third of the triggers have tracks, and 95% of the reconstructed tracks come from the target. One-third of the triggered events contains a scattered positron.

The data are written to 9 GB staging disks during a fill. In between two fills the data are copied to the DESY main computer center using a FDDI link. At the HERMES experimental site the data are copied to DLT tapes. The data are written in blocks of 429 MB (run) containing about 50 data units (burst).

3.4.4 Detector performance

Apart from the figures given above it is useful to provide some additional information on the performance of the spectrometer.

At standard unpolarized running conditions ($L \approx 10^{32}$ nucleons/cm^{2}s) the trigger rate is typically 50 Hz. A significant part of the unpolarized data has been collected at a much higher luminosity ($L \approx 10^{33}$ nucleons/cm^{2}s) with trigger rates up to 500 Hz, depending on the chosen prescale factors for individual subtriggers. At these high luminosity conditions the deadtime was always below 10%.

All detectors making up the spectrometer performed well. At standard operational conditions the data quality cuts which reflect the performance of the detectors, target and data acquisition together, resulted in the rejection of only about 15% of the data.

The particle identification detectors allow a positron identification with an efficiency of 99% with a hadron contamination of less than 1%. The momentum resolution is good and equals 0.7% at 4 GeV and 1.25% at 25 GeV positron energy.

Chapter 4

Vertex Chambers

4.1 Introduction

A large Micro-Strip Gas Counter (MSGC) is the first tracking detector at the HERMES deep-inelastic lepton scattering experiment at DESY. It is used for the determination of the interaction vertex. This vertex chamber (VC) consists of two separate units, one above and one below the beam line. Each detector half comprises 6 planes with an active area of 13×40 cm^2 each. To minimize the data transfer time, the signals of the 24800 anode strips are digitized at an early stage, resulting in a deadtime of less than 58 μs.

In this chapter the layout and performance of the HERMES vertex chambers is presented. For this pupose the text of an article which previously appeared in Nuclear Instruments and Methods in Physics Research[1] is reproduced in the following section. A more detailed description of the vertex chambers including its design and construction can be found in reference [39]. In the last two sections of this chapter some additional information is given on the occupancy of the chambers, and the use of Micro-Strip Gas Chambers in other high energy physics (HEP) experiments.

[1] J.J. van Hunen, Nuclear Instruments and Methods in Physics Research A409 (1998) 95-99, *Performance of the HERMES Micro-Strip Gas Chamber*, reprinted with permission from Elsevier Science.

4.2 Performance of the vertex chambers

4.2.1 Introduction

The HERMES experiment at HERA is designed to investigate the spin structure of the nucleon. Polarized positrons with an energy of 27.5 GeV are deep-inelastically scattered from a polarized internal gas target. Inclusive as well as semi-inclusive events have been collected using polarized ^{1}H and ^{3}He, and unpolarized ^{1}H, ^{2}D, ^{3}He, and ^{14}N targets. A Micro-Strip Gas Counter is used as the tracking system closest to the target. It combines excellent position resolution with small radiation length. The HERMES MSGC system [40] was designed and constructed at NIKHEF. It is able to determine the tracks with an angular resolution of better than 200 μrad, which matches the uncertainty due to multiple scattering from the target exit window. In order to obtain two space points either above or below the beam line, 12 planes are used. These 12 planes are arranged in 4 groups, each group consisting of 3 planes. The 3 planes have their strips at respectively $+30^0$, -30^0 and 0^0 with respect to the vertical axis.

4.2.2 Design considerations

The main challenge in the design and construction of the present MSGC is the large size in combination with a small radiation length and fast data readout. Since the integrated luminosity at HERMES is low, no special measures to minimize aging effects are necessary.

The complete set-up is displayed in figure 4.1. The 6 MSGC planes of the bottom half of the detector are visible. The distance between the HERA positron beam pipe and the edge of the MSGC planes is only 2 mm. The gas target extends over a distance of 40 cm, the center being located at a distance of 73 cm from the first MSGC plane. Since the chamber is operated with a Ne/DME gas mixture, which is flammable, it is necessary to have an additional entrance and exit foil creating a volume which is flushed with N_2 and monitored for possible DME content. The inner foils are made out of copper coated kapton with a thickness of 75 μm. The outer windows are made of aluminized mylar with a thickness of 50 μm. The individual planes can be aligned in the vertical direction with a precision below 20 μm. The geometrical acceptance of the MSGC in both the horizontal and vertical planes is shown in figure 4.2.

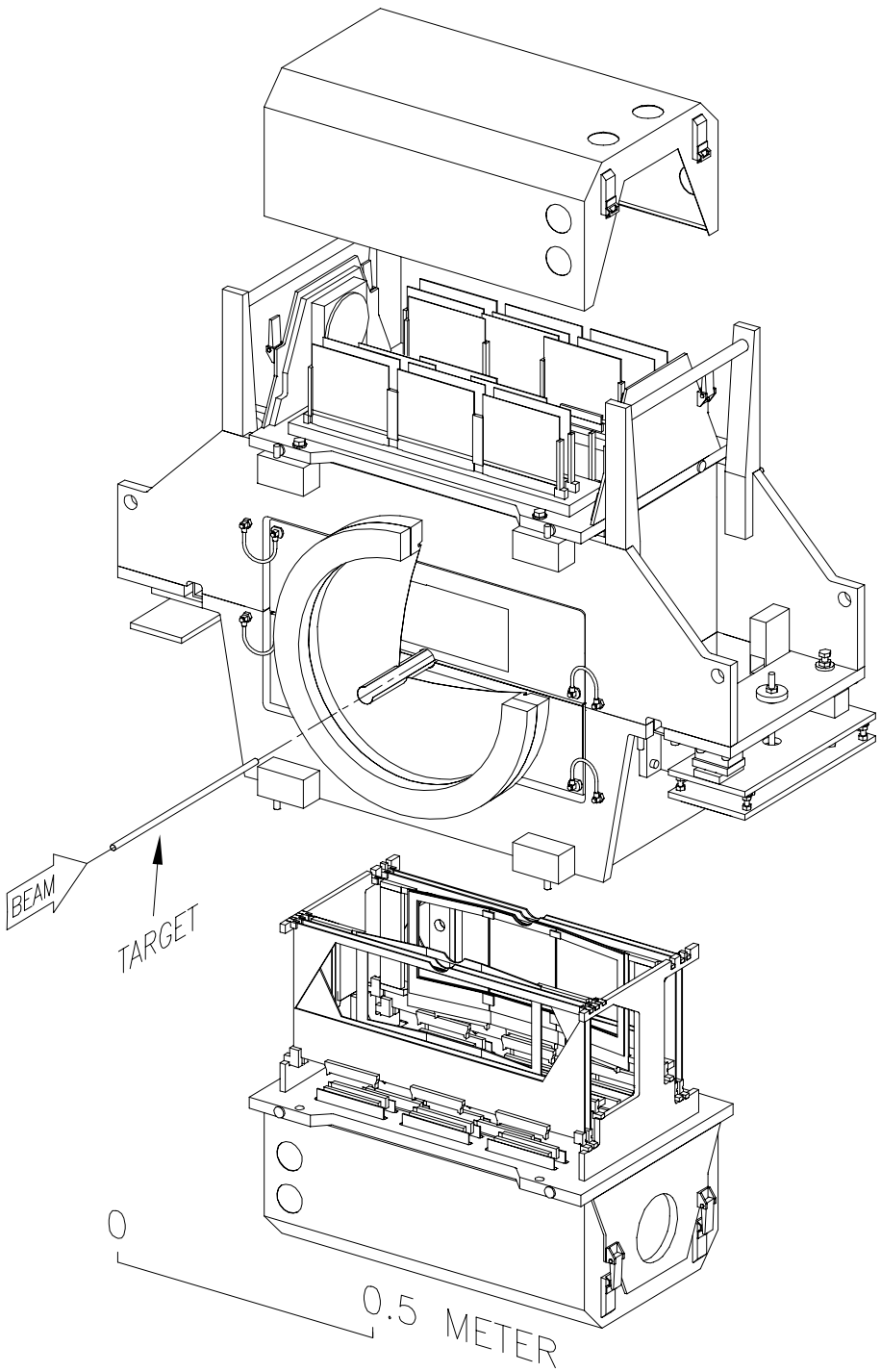

Figure 4.1: Exploded view of the vertex detector.

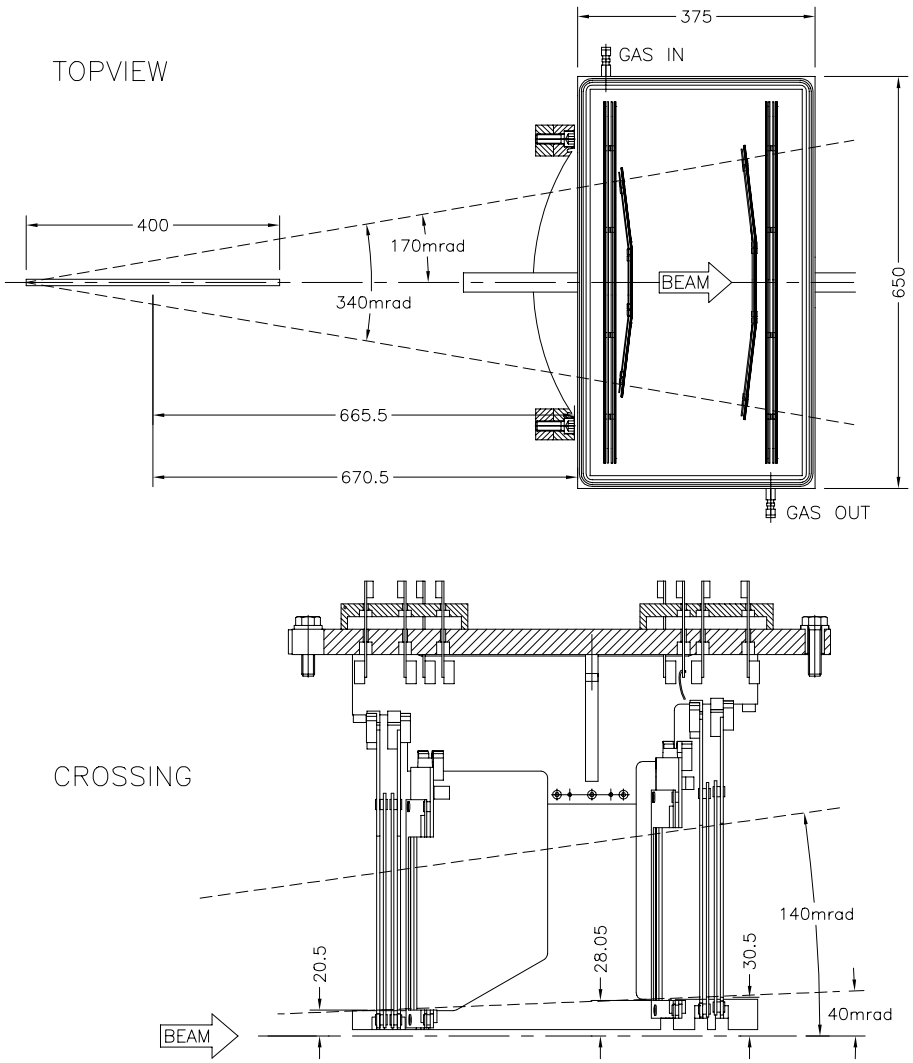

Figure 4.2: Top and side view of one half of the the MSGC. The 6 planes are arranged in a UVX and XVU sequence, respectively. A U plane contains strips under $+30^0$ with respect to the vertical axis, a V plane under -30^0, and an X-plane has strips parallel to the axis. The horizontal and vertical angular acceptance are given by 40 mrad $\leq \mid \theta_{vert} \mid \leq$ 140 mrad and $\mid \theta_{hori} \mid \leq$ 170 mrad.

Configuration of the detector planes

The production size of the glass substrates is large, which is difficult in view of their thickness. In fact, 200 μm is the minimum thickness that can be used since otherwise electrostatic deflections become critical. To obtain an active area of around 13×40 cm^2 several substrates are used for one detector plane. In the case of a 30^0 plane five substrates are used, in the case of a 0^0 plane three. The substrates and the chips for the readout are glued on regular PC boards.

Configuration of the micro-strip substrates

While standard substrates have been used for the HERMES MSGC's, special care is taken to protect the strips against discharges. For protection of the strip structure and the preamplifiers the substrates are equipped with NiCr resistors which are created in the photolithographic process. The resistors which connect groups of 16 cathode strips to the HV supply are 1 MΩ and limit the energy of a discharge to 35 μJ. The resistors which connect the anode strips with the preamplifiers have a value of 1 kΩ and limit the maximum current to 0.5 A. The relevant materials and measures of the micro-strip substrates are listed in table 4.1. Because the integrated luminosity collected during years of running is modest at HERMES, standard Desag-263 substrates with aluminium strips are used. Aging curves have been measured at NIKHEF [41], which indicate a maximum gain loss of a few percent per year. The drift of Na^+ ions in the substrates can lead to an increase in the gain of a few percent during a one year running period. In order to avoid depletion of Na^+ ions near the anode strip, the polarity of the strip voltage can be inversed during the yearly shutdown period.

Digital readout of the MSGC

A fast readout of the MSGC requires that the 24800 channels are digitized at an early stage. No pulse height information is stored as the required position resolution can be obtained without application of the center-of-gravity method. Use is made of the APC-64 chip which has 64 input channels. For the data readout 62 channels are used while the remaining 2 serve as a reference. Each chip is read out by a separate discriminator to minimize the deadtime. A first trigger can be accepted immediately, the second trigger can be accepted after 58 μs.

Table 4.1: Key parameters of the HERMES MSGC

Cathode Plane	Cu (1 μm), Kapton (75 μm)
Micro-strips	NiCr (5 nm) + Al (1 μm)
Substrate	200 μm Desag-263
Gas mixture	Ne/DME (50/50)
MSGC support	PC board
Cathode strip width	85 μm
Anode strip width	7 μm
Anode pitch	193 μm
0^0 substrate	150 $\times$ 150 mm^2 (production)
30^0 substrate	150 $\times$ 200 mm^2 (production)
Gas gap	3 mm

4.2.3 Performance of the MSGC

Tracking efficiency

The MSGC was first installed and tested under beam conditions in 1995. However, as the available APC-64 chips did not satisfy their specifications, the chamber could only be operated at reduced efficiency. During the yearly shutdown in 1996 the upper MSGC system was upgraded. The APC-64 chips were replaced by an improved version, and several micro-strip substrates, which had suffered from an error in the photolithographic process, were replaced. The upper half of the MSGC system was reinstalled in June 1996, while the lower chamber was added in February 1997. Since the reinstallation, data have been collected over more than ten months. With an average of 10 h of positron beam per day this amounts to more than 3000 h of operation. During this period the efficiency was high and very stable, as can be seen from figure 4.3.

In order to obtain the absolute values of efficiency an internal efficiency code has to be used to avoid effects of the efficiency of other tracking detectors within HERMES. During a short period of time (indicated by the absence of data in the figure) no efficiency values could be determined due to a temporary readout problem. The efficiency was determined with an internal efficiency code by comparing the relative yield in the individual MSGC planes. A value of 94% was found, where the difference from 100% is largely

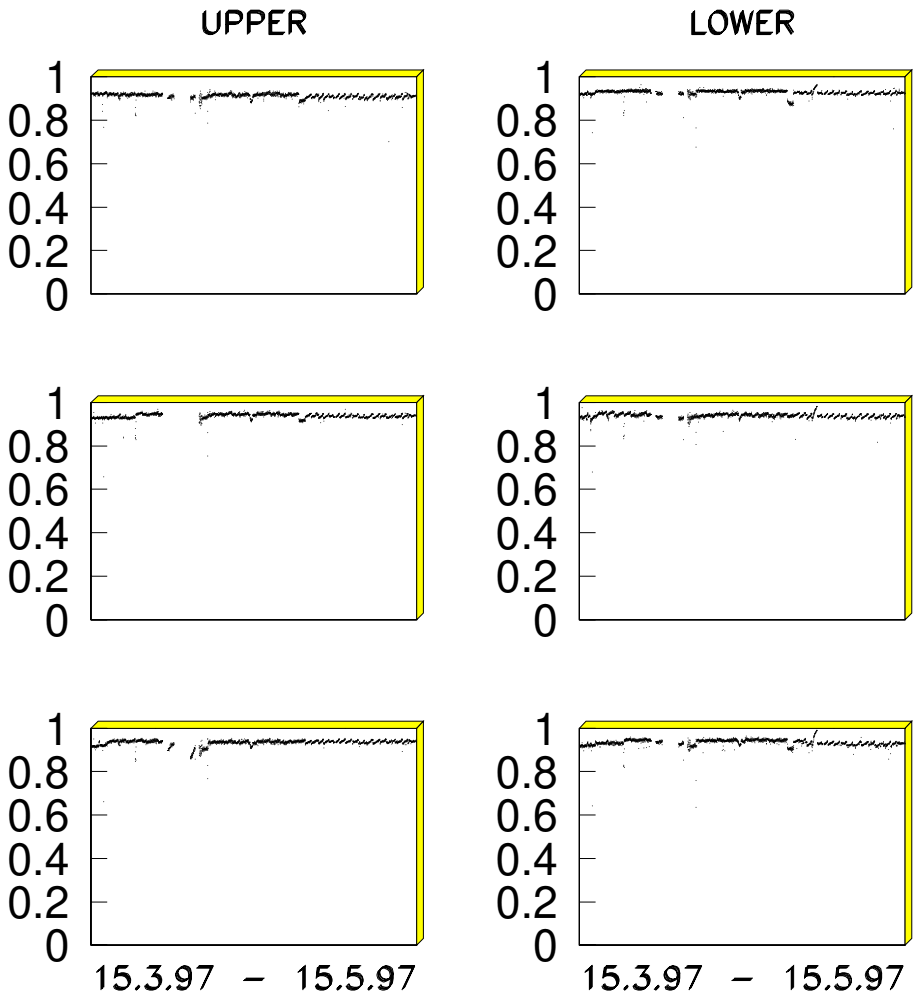

Figure 4.3: The tracking efficiency of 6 sample MSGC planes as determined by the HERMES tracking system. A track is defined by all available tracking chambers of the HERMES spectrometer. In the front region 9 planes out of 30 are allowed to have no hit on the track, in the back region, i.e. behind the spectrometer magnet, 9 out of 24 can miss a track. Since there is a dependence of the MSGC efficiency on the performance of the other tracking chambers, the efficiency displayed does not represent the real efficiency of the MSGC.

understood from known technical defects. Correcting for these effects, the operational parts of the MSGC's had an efficiency of 98%. The known defects include:

- Interrupted anode strips (during the photolithographic process): 1.2%
- Broken NiCr resistors (during the photolithographic process or an imperfect edge due to the cutting process): 1.5%
- Subtraction of "hot channels" (due to defects in the electronics): 1.6%

Position resolution

For the 1997 data the average residual with respect to a track determined by the HERMES tracking chambers was found to be 71 μm, as shown in figure 4.4. This value can be further reduced if the positions of the individual planes of the HERMES tracking chambers, as well as the individual substrates of the MSGC planes are optimized in the software. In 1996, after optimalization of the alignment, the best planes had a position resolution better than 48 μm, providing an angular resolution of 240 μrad.

4.2.4 Conclusions

A large array of MSGC's has been operated successfully in the HERMES deep-inelastic scattering experiment at DESY. During 1996 and the first half of the 1997 running period the upper chamber has been under operating conditions for 3000 h. Since the beginning of the 1997 run the lower chamber has been in operation equally successfully. The tracking efficiency is high, on average 94%, and if corrected for known mechanical defects, the efficiency is even higher. There has been no sign of aging after one year of running. However, cancellation of the increase of the gain due to the Na^+ drift in the substrate, and the decrease due to aging might occur. The position resolution is good. After optimalization of the alignment, the residuals of the MSGC tracks were found to be 71 μm. Further improvements for the 1996 and 1997 data are expected.

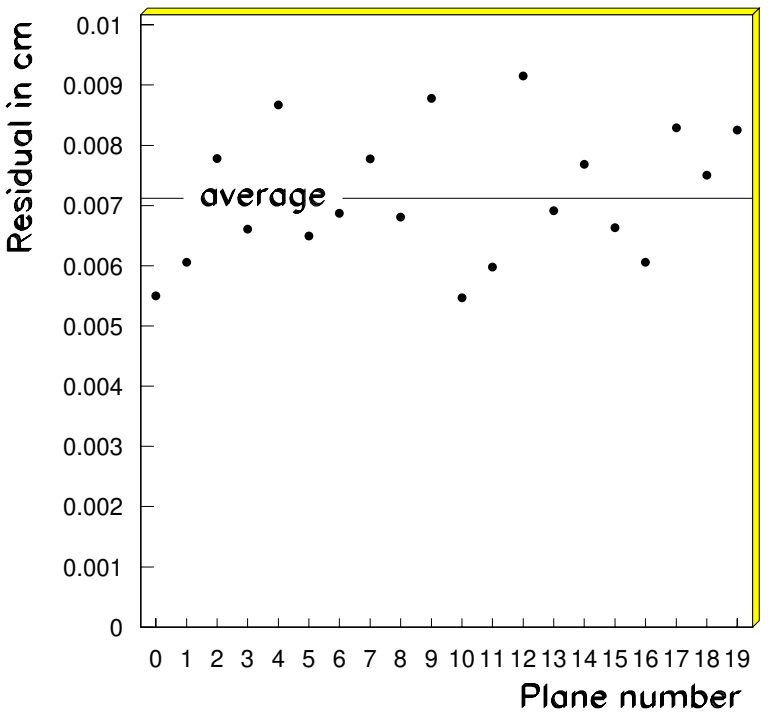

Figure 4.4: The residuals of the MSGC planes with respect to a track, determined by the HERMES tracking system.

4.3 Occupancy of the MSGC at HERMES

At standard (polarized) running conditions the occupancy of the MSGC was studied. Events from a random trigger were collected, and the number of hits above threshold per event were determined for all the MSGC planes separately.

Generally the lower chamber (below the beam line) has a lower occupancy than the upper chamber. This is most likely related to the different background conditions in the upper and lower detector, because the lower half of the HERMES spectrometer is better shielded. It may also be related to the fact that the APC chips from the upper chamber were in use one year longer than the APC chips from the lower chamber, and therefore could reveal a radiation damage effect.

The number of hits per event for the lower MSGC planes ranges from 7.5

to 10.4, while for the upper MSGC planes it ranges from 9.5 to 16.6. The numbers depend on the plane position (closer to the target implies more hits), as well as the quality of the readout electronics of the plane. Given the number of strips per plane, the measured occupancy is about 0.43±0.06 % for the lower MSGC and 0.60±0.16 % for the upper MSGC. The occupancy measurements have been carried out at a luminosity of about 1.7×10^{31} nucleons/cm^{2}s. At a higher luminosity (10^{33} nucleons/cm^{2}s) the MSGC's have been operated as well, showing an occupancy which was only 2-3 times higher. This indicates that, to a large extent, background tracks (not originating from the gas target) contribute to the occupancy numbers given above.

4.4 MSGC's in other experiments

The good position resolution, high tracking efficiency, and high rate capability of MSGC's make it a suitable detector type for high energy physics experiments. As shown in the previous section, at the HERMES experiment a large array of MSGC's has been operated successfully at luminosities up to 10^{33} nucleons/cm^{2}s. However, performance interruptions have occurred in 1998 and 1999 because of broken APC chips, most likely due to radiation damage.

Also at other experiments MSGC's are in use. At the HERA-B experiment at DESY, for instance, the inner tracking chamber is of the MSGC type. However, the occurrence of discharges made it necessary to implement an additional amplification step. A Gas Electron Multiplier (GEM) [42, 43] was therefore used in conjunction with the MSGC, i.e. an additional electron amplifier was inserted between the cathode plane and the substrate. The voltage of the MSGC can therefore be reduced, decreasing the probability for discharges. The GEM-MSGC combination [44] is a promising development of the MSGC technology for future applications.

Chapter 5

A-dependence of $R = \sigma_L/\sigma_T$

5.1 Introduction

The F_2 structure function can be expressed in terms of the longitudinal and transverse virtual photon absorption cross sections, σ_L and σ_T (Eq. (2.20)). Given the observed modification of F_2 inside the nuclear medium [1], it is of interest to study the A-dependence of σ_L and σ_T separately. This is particularly interesting since σ_L is sensitive to higher twist effects, i.e. quark-gluon correlations, which are expected to be enhanced in nuclei [4, 20]. The difference in the A-dependence of the longitudinal and transverse component can be investigated by studying the A-dependence of $R = \sigma_L/\sigma_T$, the ratio of the longitudinal and transverse virtual photon absorption cross sections.

The ratio R is an important observable in deep-inelastic scattering (DIS), as it probes the nucleon beyond leading order. Measurements of R [19] show that it is different from zero in the range $Q^2 < 20$ GeV^2 and $x < 0.1$.

An A-dependence of R may be related to spin-0 objects in the nucleus, which may be the result of correlations between partons of neighboring nucleons. Such a higher-twist effect is predicted to be enhanced in nuclei, leading to a ratio R_A/R_D larger than unity. For the leading twist term it was suggested that the gluon distribution may be enhanced in nuclei, which would also give rise to $R_A > R_D$ [21]. An alternative mechanism, in terms of shadowing, was suggested in references [22, 23], where a difference in nuclear shadowing for longitudinally and transversely polarized photons is also shown to enhance R in a nucleus.

Usually the A-dependence of R is investigated by measuring the DIS cross

section on various nuclei at two different beam energies. At each beam energy the DIS cross section at a given value of (Q^2, x) corresponds to a different value of the virtual photon polarization parameter ϵ. From the two cross sections a value for R and F_2 can be obtained using Eq. (2.16). However, for this method (often referred to as 'Rosenbluth Separation') an absolute measurement of the cross section at each beam energy is needed, introducing a relatively large systematic error on R. By carrying out this procedure for different target nuclei, the A-dependence of R can be determined. As can be seen from figure 2.4 measurements of $\Delta R = R_{A1} - R_{A2}$ suffer from large uncertainties, since a difference must be taken between two variables carrying large error bars.

In this chapter we present the ratios $R_{^{14}N}/R_D$ and $R_{^3He}/R_D$ which are evaluated at a single beam energy by exploiting the large ϵ-range ($0.3 < \epsilon < 1.0$) covered by the HERMES spectrometer. The data still span a sizable ϵ-range after they have been split in small x-bins. Therefore, cross section ratios σ_A/σ_D can be measured as a function of ϵ for a number of small x-bins. From these data, ratios of the type R_A/R_D and F_2^A/F_2^D are determined, thus avoiding the large errors that would arise in an absolute measurement. Since the HERMES spectrometer allows to study the cross section ratios at relatively small scattering angles, the R_A/R_D values can be determined for Q^2 values as low as 0.4 GeV^2.

In the next section, the extraction of the cross section ratios is discussed. These results are used to determine the ratios $R_{^{14}N}/R_D$ and $R_{^3He}/R_D$ as a function of x and Q^2. The last but final section is devoted to the interpretation of the data. Concluding remarks are given in the final section.

5.2 Cross section ratios for ^{14}N and ^{3}He

Inclusive DIS events on ^{14}N, ^{3}He, and ^{2}H are used to determine the cross section ratios σ_N/σ_D and σ_{He}/σ_D. In this section the data analysis is discussed, and the results on the cross section ratio are presented.

5.2.1 Event selection

The data collected on ^{3}He, ^{14}N, and ^{2}H contain a few million DIS events for each target. However, the collected data also contain events which do not include a scattered positron, or a positron that cannot be uniquely identified

to represent a true DIS event. Furthermore there were periods during the run where a small part of the spectrometer did not function properly due to, for example, a high voltage interrupt, resulting in missing or incorrect information in a number of events. Therefore the raw events have to be filtered, thus removing corrupted and non-DIS events. In the following two subsections the criteria which are imposed on the events are explained. The first subsection describes the constraints that ensure that the spectrometer functioned optimally. In the following subsection the constraints on the kinematics are discussed. The number of events that passed all the selection criteria, and the radiative corrections, are presented in the last subsections.

Data-quality

There are several sources of information on the performance of the spectrometer. The HERMES data files (96b and 97b μDST) contain information on high voltage interrupts (*HV-trips*) of the detectors, target type and performance, performance of all individual detector systems, and data acquisition (DAQ) status. Additionally, a logbook is maintained that lists any problem with the equipment, mediated through alarm messages and signals during data taking. For every HERA fill and HERMES data taking period (i.e. a period with the complete spectrometer and DAQ system switched on) a so called run summary is written.

The logbook and run summaries were use to reject data due to HV-interrupts, incorrect target mode, and problems which were not included in the automatic registration scheme (only occurring occasionally). The information in the μDSTs was checked using dedicated software. The following additional conditions were imposed in the analysis.

- Data acquisition
  - Dead-Time (DT in %): $DT < 20$
  - *Burst* Length (BL in seconds): $BL \leq 11$
  - First and last *burst* of each *run* are removed since these data are corrupted in the data acquisition.

- Spectrometer components
  - Gain monitoring system (GMS): a *burst* is eliminated if dead blocks existed in the lower or upper half of the calorimeter, or preshower counter.
  - Tracking chambers: a *burst* is eliminated when a *HV-trip* was reported in either the FCs, BCs or Calorimeter.
  - Particle identification detectors: a *burst* is eliminated when a *HV-trip* was reported in the TRD.
  - Calorimeter threshold (CT): only events with at least one particle depositing more than 3.5 GeV in the calorimeter were selected.

5.2.2 Constraints on the lepton kinematics

Tracking was done with the forced-bridge [45] method, using the FCs for tracking in the front region. A number of constraints on the scattering angle, vertex position and kinematics were applied. The constraints on the kinematic quantities concern Q^2 to ensure the applicability of the QCD framework, W^2 to exclude the resonance region and thus define the DIS character of the event, and y to limit the size of the radiative corrections.

- The positron track is required to be within a well defined region of the HERMES spectrometer ($0.040 < |\theta_y| < 0.140$ rad and $|\theta_x| < 0.170$ rad), implemented by explicit cuts on θ_y and θ_x as well as by using the μDST information (named *iSelect*).
- The origin of the track (position vertex) is required to be within the target region : $|z_L| < 18$ cm and $|z_T| < 0.75$ cm.
- Positron identification: $PID3 + PID5 > 2.0$ (see section 3.4.2)
- The 4-momentum transfer squared and invariant mass of the virtual photon:
  - $Q^2 > 0.3$ GeV^2
  - $W^2 > 4$ GeV^2

- Additional constraints
  - $y < 0.85$
  - Energy of the cluster in the colorimeter (E_{calo}): $E_{calo} > 3.5$ GeV

5.2.3 Number of DIS events

The total number of *runs* and DIS events (in millions) on ^{2}H, ^{3}He, and ^{14}N, after data-quality and kinematic cuts, is listed for the two years of data taking in table 5.1.

Table 5.1: Number of RUNS (DIS events)

	^{2}D	^{3}He	^{14}N
1996	508 (2.80M)	196 (0.8M)	–
1997	729 (2.75M)	–	694 (2.26M)

5.2.4 Radiative corrections

The measured cross section has to be corrected for radiative effects, i.e. processes in which the initial or final positron emits a photon causing a shift in the kinematics. These corrections can be calculated exactly in quantum electrodynamics (QED) if the one (virtual) photon exchange cross section, also referred to as 'Born cross section', is known over a large kinematic (x, Q^2) range. Radiative processes may shift scattering strength from the unmeasured region into the HERMES acceptance. In order to correct for this, extrapolations (and/or other experimental data) are needed that describe the DIS cross section in this domain. The Born cross section can be calculated from the structure functions F_1 and F_2, or equivalently F_2 and R (Eqs. (2.9) and (2.16)). However, these structure functions are the quantities which we would like to determine from our measurement. The solution is the use of an iterative procedure.

The radiative corrections receive contributions of elastic, quasi-elastic and inelastic scattering. The elastic contribution originates from elastic scattering

off the nucleus, the quasi-elastic contribution from elastic scattering off a nucleon bound in a nucleus, and the inelastic contribution from scattering off a quark [46]. For the cross section ratio at low (x, Q^2), the dominant contribution comes from elastic scattering, for the high (x, Q^2) region (where the radiative corrections are much smaller) the dominant contribution to the cross section ratio originates from inelastic scattering.

The corrections are evaluated using the calculations of Akhudov, Bardin, and Shumeiko [47, 48, 49]. The following higher order QED processes are included: vacuum loops of all leptons and quarks, lepton pair production, electroweak interference and bremsstrahlung.

Iterative procedure

As was mentioned before, the Born cross section is needed to determine the size of the radiative contributions. In order to calculate the Born cross section the structure functions F_2 and F_1 are needed, or alternatively the structure function F_2 and the cross section ratio $R = \sigma_L/\sigma_T$ (Eq. (2.16)). An iterative procedure is implemented, in which initially existing data are used for F_2 and R to evaluate the cross sections - and thus F_2 and R - in first approximation. Next these values of F_2 and R are used to re-evaluate the radiative corrections. This sequence is repeated until convergence is obtained, i.e. the difference between the successive values of F_2 and R is less than 0.2%. In order to reach convergence three iterations were needed, mainly for the low (x, Q^2)-bins where the corrections are largest.

The starting value of the Born cross section was determined using the Whitlow parametrization [50] for R_D, and a parametrization [51] of the NMC, SLAC, and BCDMS data for F_2^D. For the elastic contribution the nuclear form factors for ^{2}H, ^{3}He and ^{14}N were taken from references [52]-[54]. The quasi-elastic contribution was determined using a parametrization of the nucleon form factor from Gari and Krümpelmann [55]. The reduction of the bound nucleon cross section with respect to the free nucleon cross section due to the Pauli exclusion principle (quasi-elastic suppression) was determined using the calculations from Bernabeu [56] (^{2}H) and a non-relativistic Fermi gas model [57] (^{3}He and ^{14}N).

It has been investigated to what extend the main conclusion derived from our analysis (i.e. $R_A > R_D$ at low Q^2) depends on the iterative procedure that was used to evaluate the radiative corrections. For that purpose the

data have also been analyzed with radiative corrections in which $R_A = R_D$ is assumed, i.e. without iterations. For R_D a parametrization was taken that was determined by other experiments [50]. The results are discussed in Appendix B, where it is shown that this alternative analysis yields the same conclusion, i.e. $R_A > R_D$. However, quantitatively the non-iterated result is on average 30% smaller in the lowest three x-bins. At the same time it must be realized that the iterative procedure represents the only correct method to evaluate the radiative corrections.

The effect of using $R_A/R_D > 1$ in the evaluation of the radiative corrections is an increase of the radiative corrections. The Born cross section decreases (see Eq. (2.16)) while the elastic and quasi-elastic cross sections, which are not dependent on the Born cross section, remain unchanged. The relative contribution of elastic and quasi-elastic scattering, and thus also the radiative corrections related to these, increases. The increase of the radiative corrections lead to a decrease of the σ_A/σ_D cross section ratios of about 15% for ^{14}N and 5% for ^{3}He, at the lowest x-bin.

A detailed description of the evaluation of the radiative corrections, the external inputs and the systematic error determination is presented in ref. [58].

Systematic uncertainty

For the evaluation of the systematic uncertainty on the radiative corrections the input parametrizations were varied. The different contributions to the systematic uncertainty on the radiative corrections were estimated by using the upper and lower limits of the parametrizations, and by using alternative parametrizations [59, 60].

The total systematic uncertainty of the cross section ratio due to the radiative corrections is shown for different (x, Q^2)-bins in the 3^{rd} and 5^{th} column of table 5.2. The size of the radiative corrections (as presented in section 5.2.7), and therefore the uncertainty in the cross section ratio due to the radiative corrections, decreases with increasing x.

5.2.5 Smearing corrections

Due to inaccuracies in the determination of the scattering angle and particle momentum, the deduced kinematic quantities such as x and Q^2 possibly need to be corrected. This correction is referred to as smearing correction.

Table 5.2: The systematic uncertainty in $\sigma_{^{14}N}/\sigma_D$ and $\sigma_{^3He}/\sigma_D$ due to the radiative corrections (rc), and the total systematic error including the normalization uncertainty (tot).

x	Q^2	$\Delta\frac{\sigma_{^{14}N}}{\sigma_D}$ (%)		$\Delta\frac{\sigma_{^3He}}{\sigma_D}$ (%)	
		rc	tot	rc	tot
0.0125	0.51	4.28	4.53	3.62	3.76
0.0175	0.66	2.32	2.69	2.78	2.95
0.025	0.88	2.06	2.55	2.52	2.71
0.035	1.13	1.42	2.07	1.22	1.58
0.045	1.33	1.05	1.83	1.10	1.49
0.055	1.52	0.94	1.79	1.04	1.44
0.070	1.73	0.62	1.62	0.65	1.19
0.090	2.00	0.42	1.56	0.46	1.10
0.123	2.33	0.41	1.56	0.45	1.10
0.174	2.60	0.30	1.53	0.30	1.04
0.249	3.00	0.30	1.53	0.30	1.04
0.395	4.40	0.30	1.53	0.30	1.04

For the determination of the correction factors for the ^{3}He cross section ratio, 10 million ^{3}He and 19.6 million ^{2}D Monte-Carlo events were generated. The HERMES Monte Carlo (HMC [61]) program generates DIS events and tracks the event through the HERMES spectrometer. The results for the correction factors, i.e. the ratio of the cross section ratio with and without all smearing effects on the kinematics as determined from HMC, are shown in figure 5.1.

It can be seen that the smearing corrections are smaller than 0.25% over the entire x-region. For the low x-region ($x < 0.04$), where the cross section ratio depends most strongly on x, the corrections are even smaller than 0.1%. Since the dependence on x of the σ_N/σ_D data is somewhat larger than that of the σ_{He}/σ_D data, the smearing corrections for $\sigma_{^{14}N}/\sigma_D$ will also be larger. However, as the absolute size of the smearing corrections is much smaller than the errors on the radiative corrections, the smearing corrections for both ^{3}He and ^{14}N have been neglected.

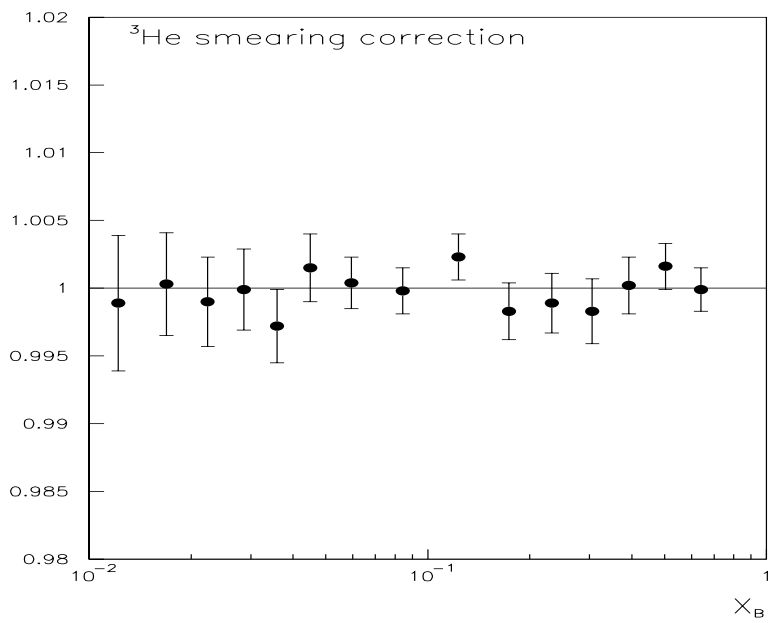

Figure 5.1: Smearing correction for ^{3}He as a function of x.

5.2.6 Uncertainty in the cross section ratio

The results of this analysis are presented in the next section as a ratio of inclusive cross sections. Therefore systematic errors due to the detector inefficiency, acceptance effects, and the absolute normalization, cancel. The main source of systematic uncertainties is the correction for radiative effects, as discussed in the previous sub-section. Remaining uncertainties stem from possible time dependencies of the acceptance and the detector performance. In order to estimate this effect the reproducibility of the data has been investigated by comparing the cross section ratio for three different periods in which largely different target densities were used. The results obtained for each of the different periods deviate from the results where all the data are used by less than 1.5%, which is used as an additional normalization error for ^{14}N (see also figure 5.10). Similar studies for ^{3}He yield a normalization error of 1%. Since different target densities were used in the separate periods, this normalization error includes the uncertainty due to the use of different luminosities of the two targets in the cross section ratio. The results for the different periods are presented in the next section. The total systematic

errors in the cross section ratio for $\sigma_{^{14}N}/\sigma_D$ and $\sigma_{^3He}/\sigma_D$ are listed as the 4^{th} and 6^{th} column of table 5.2.

The statistical uncertainty in the cross section ratio is determined from the square root of the number of DIS events.

5.2.7 Results

The HERMES results for the cross section ratio $\sigma_{^{14}N}/\sigma_D$ and $\sigma_{^3He}/\sigma_D$ are shown in figure 5.2 together with the SLAC [16], NMC [15] and E665 [17] results on the neighboring nuclei ^{12}C and ^{4}He. It is noted that the structure function ratio's published by the NMC, SLAC and E665 experiments are actually cross section ratio's as the authors of reference [16, 15, 17] assumed $R_A = R_D$ in their analysis.

The experiments have used different beam energies as well as different leptons. The NMC and E665 experiment used muons with energies of 197 GeV and 470 GeV, respectively. In the SLAC experiment electrons with an energy of 24.5 GeV, and in the HERMES experiment positrons with an energy of 27.5 GeV were used.

The error bars of the HERMES data shown in the figure represent the statistical error only. The systematic error is represented by the band shown in the lower part of each panel. The statistical errors are always smaller than 0.5%, while the systematic errors for ^{14}N (^{3}He) increase from 1.5% (1.0%) at high x to about 4.5% (3.8%) at low x. The systematic error includes the normalization uncertainty of 1.5% (1.0%) added quadratically to the uncertainty due to the radiative corrections, as presented in table 5.2. The error bars of the NMC, SLAC and E665 data shown in the figure represent the statistical and the systematic error, summed quadratically.

From figure 5.2 it is concluded that while the NMC and E665 data are in agreement with each other, the HERMES data on ^{14}N are significantly below the two other data sets. For ^{3}He a similar discrepancy exists with the NMC results on ^{4}He. The effect, however, is smaller.

The ratio σ_A/σ_D as a function of Q^2, y, and ϵ for A=14 and A=3

The large difference between the HERMES results and the results from NMC and E665 is rather surprising. In an effort to understand this observation

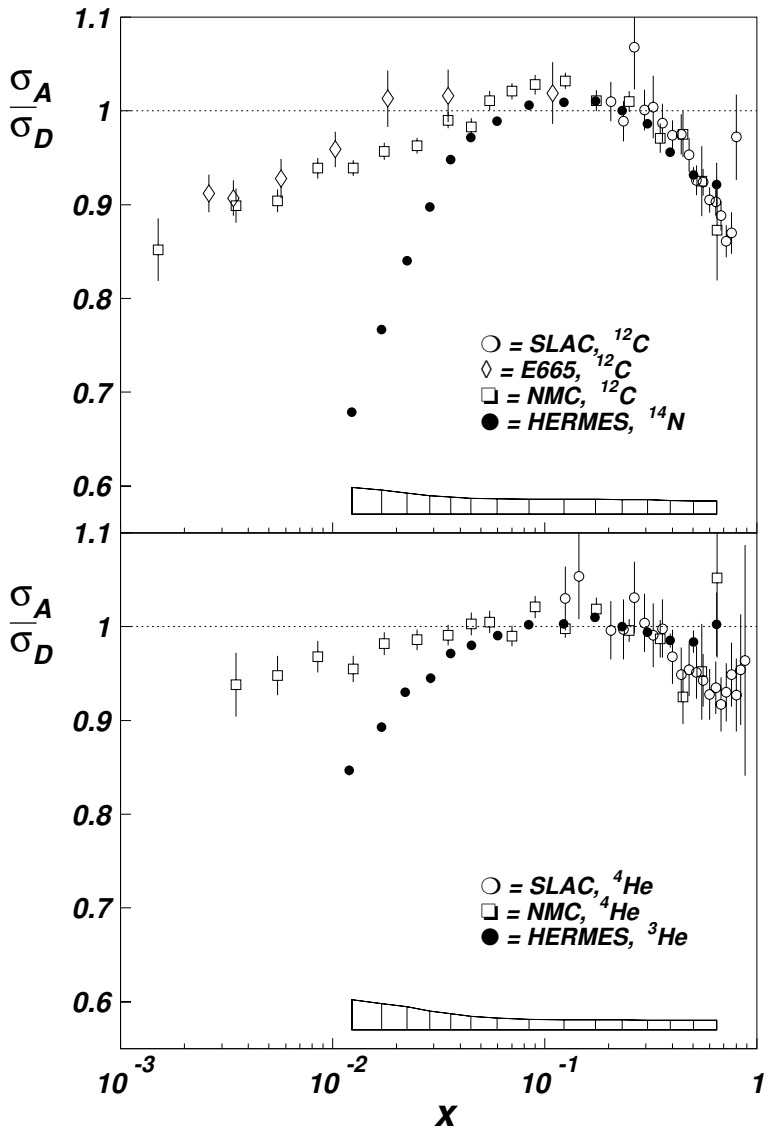

Figure 5.2: Ratio of the cross sections per nucleon as a function of x as measured by HERMES on ^{14}N (upper panel) and ^{3}He (lower panel). The HERMES data are represented as solid circles. Also shown are the data on ^{12}C (upper panel) and ^{4}He (lower panel) obtained by SLAC (open circles), NMC (open squares) and E665 (open diamonds).

the data sets have been plotted as a function of different kinematic variables, shown in figure 5.3, 5.5, and 5.7 for ^{14}N, and figure 5.4, 5.6, and 5.8 for ^{3}He.

In figures 5.3 and 5.4, the ratio of the cross sections per nucleon is shown, as a function of Q^2 and x. The error bars shown are statistical only. In the lowest x-bins a large difference is observed between NMC and HERMES data, collected at the same (x, Q^2) values. Moreover, it is seen that there is no smooth transition from the HERMES data at low Q^2 to the NMC and E665 data at higher Q^2. The discrepancy is most prominent for $0.01 < x < 0.05$, as was already noted in relation to figure 5.2.

In figures 5.5 and 5.6 the ratio of the cross sections per nucleon is shown as a function of y. Note that the value of Q^2 changes with x and y as well. It is seen in figures 5.5 and 5.6 that the deviation of the HERMES and NMC data extends over a large y-range (0.5-0.85), and increase with y. As the values of y and ϵ are closely related, a dependence of the cross section ratio on one of the two variables may be caused by a dependence on the other.

In figures 5.7 and 5.8 the ratio of the cross sections per nucleon is shown as a function of ϵ. Note once more that the value of Q^2 changes with x and ϵ. From figures 5.7 and 5.8 it is seen that the discrepancy between the NMC and HERMES data in the lowest 5 x-bins decreases with ϵ, and it seems to be absent for $\epsilon \approx 1$. The comparison of the HERMES and NMC data shows that there is an ϵ-dependence of the cross section ratio. As shown in subsection 2.1.4, an ϵ-dependence of the cross section ratio implies that $R_A \neq R_D$. As the average value of Q^2 for HERMES and NMC at the same ϵ is different, the data of figures 5.7 and 5.8 suggest that the discrepancy can be resolved by introducing an A-dependence of R which vanishes with increasing Q^2.

The remainder of the current section is used to present checks which have been carried out to verify the size of the radiative corrections and the stability of the results over different data taking periods.

Radiative corrections

Radiative corrections are important, as is shown in figure 5.9, where the ratio of the cross section per nucleon is presented with and without radiative corrections. At low x (thus low Q^2) the radiative corrections are larger for

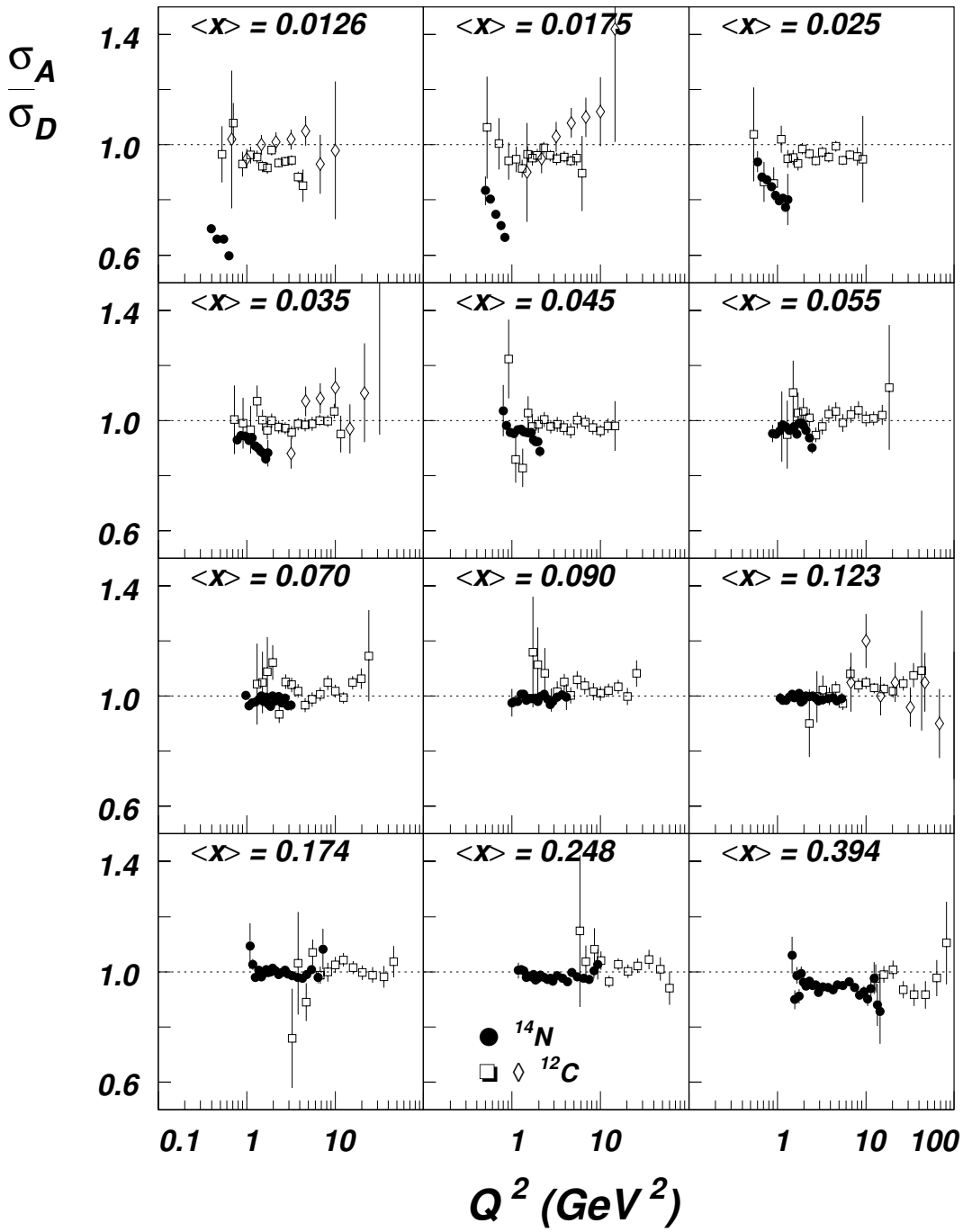

Figure 5.3: Ratio of the cross sections per nucleon as a function of Q^2 for different x-regions. The HERMES data on ^{14}N are represented by solid circles, the NMC and E665 data on ^{12}C by open squares and open diamonds, respectively. Note that the average x value of the E665 data in the 1^{st}, 2^{nd}, 4^{th} and 9^{th} bin is somewhat different from that of the NMC and HERMES data: $<x>_{E665}$ is 0.0107, 0.0196, 0.0364, and 0.121, respectively.

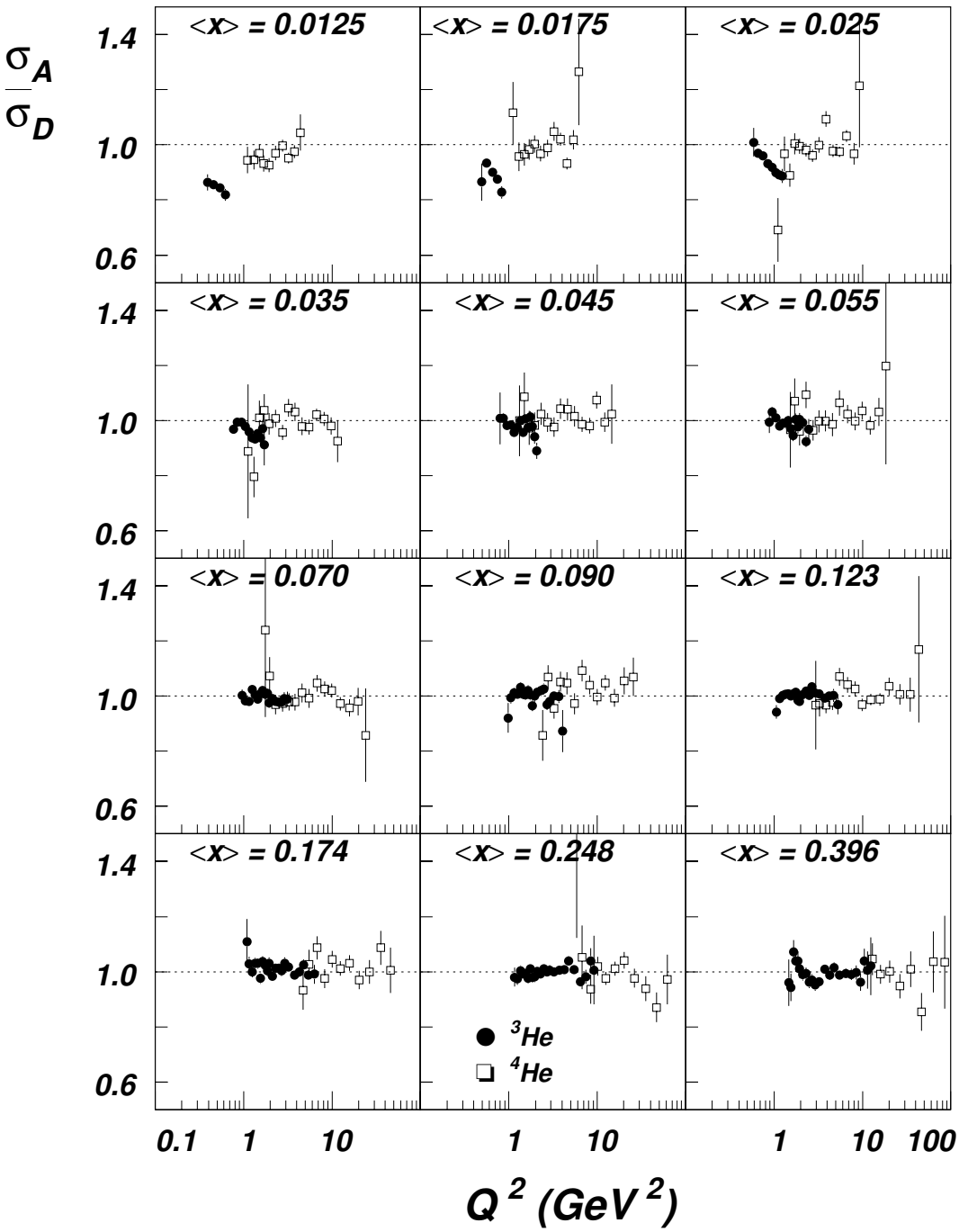

Figure 5.4: Ratio of the cross sections per nucleon as a function of Q^2 for different x-regions. The HERMES data on ^{3}He are represented by solid circles, the NMC data on ^{4}He by open squares.

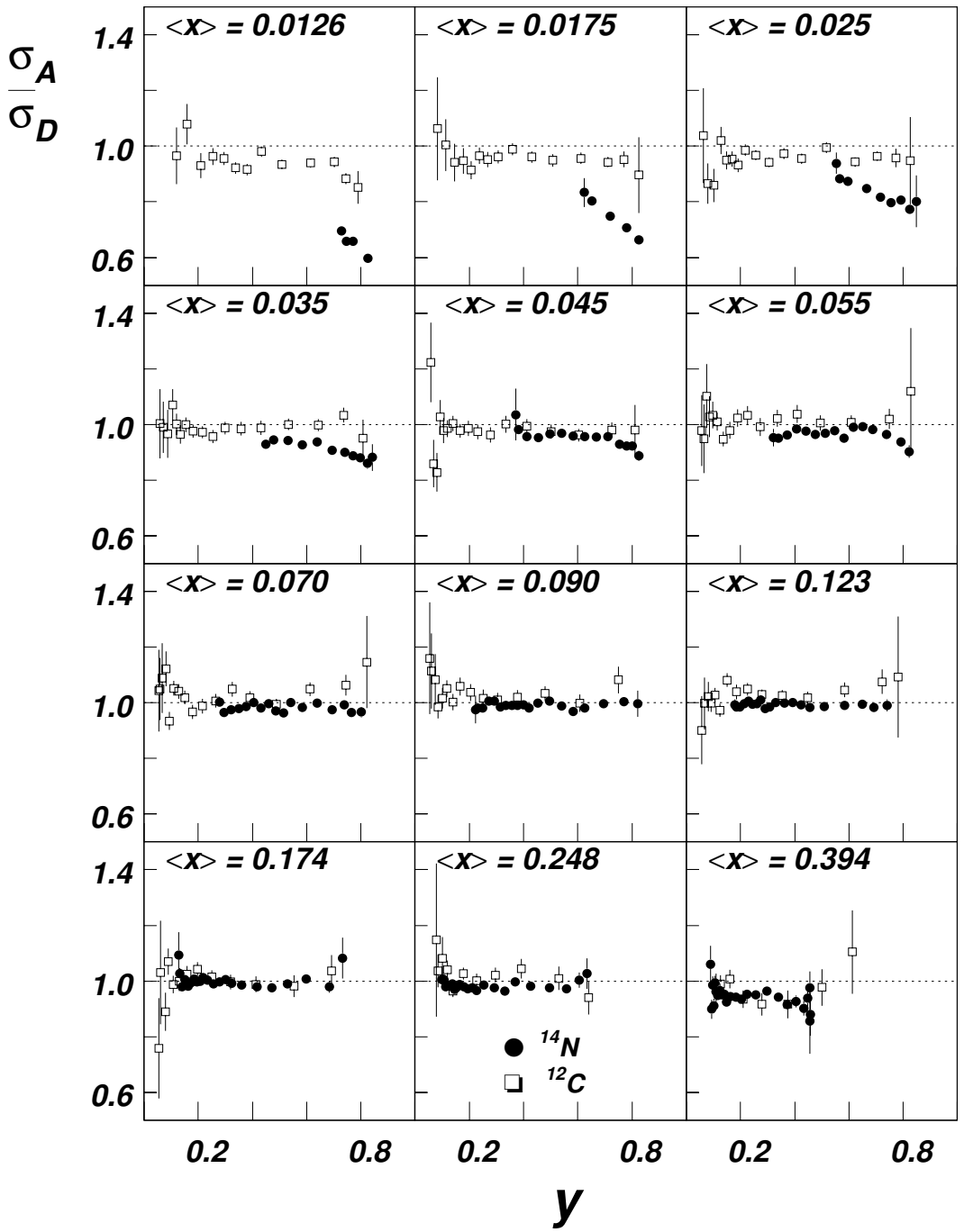

Figure 5.5: Ratio of the cross sections per nucleon as a function of y for different x-regions. The HERMES data on ^{14}N are represented by solid circles, the NMC data on ^{12}C by open squares.

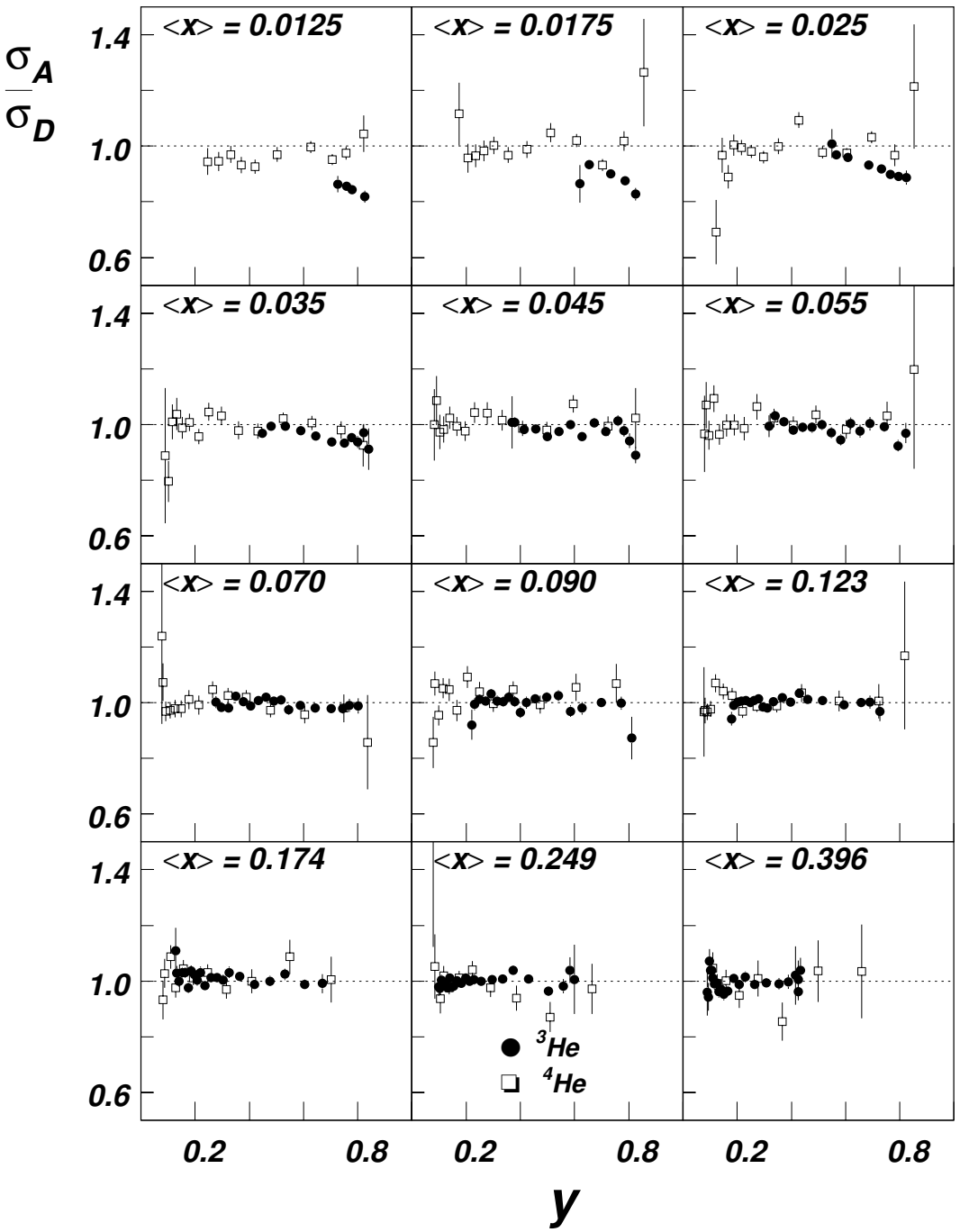

Figure 5.6: Ratio of the cross sections per nucleon as a function of y for different x-regions. The HERMES data on ^{3}He are represented by solid circles, the NMC data on ^{4}He by open squares.

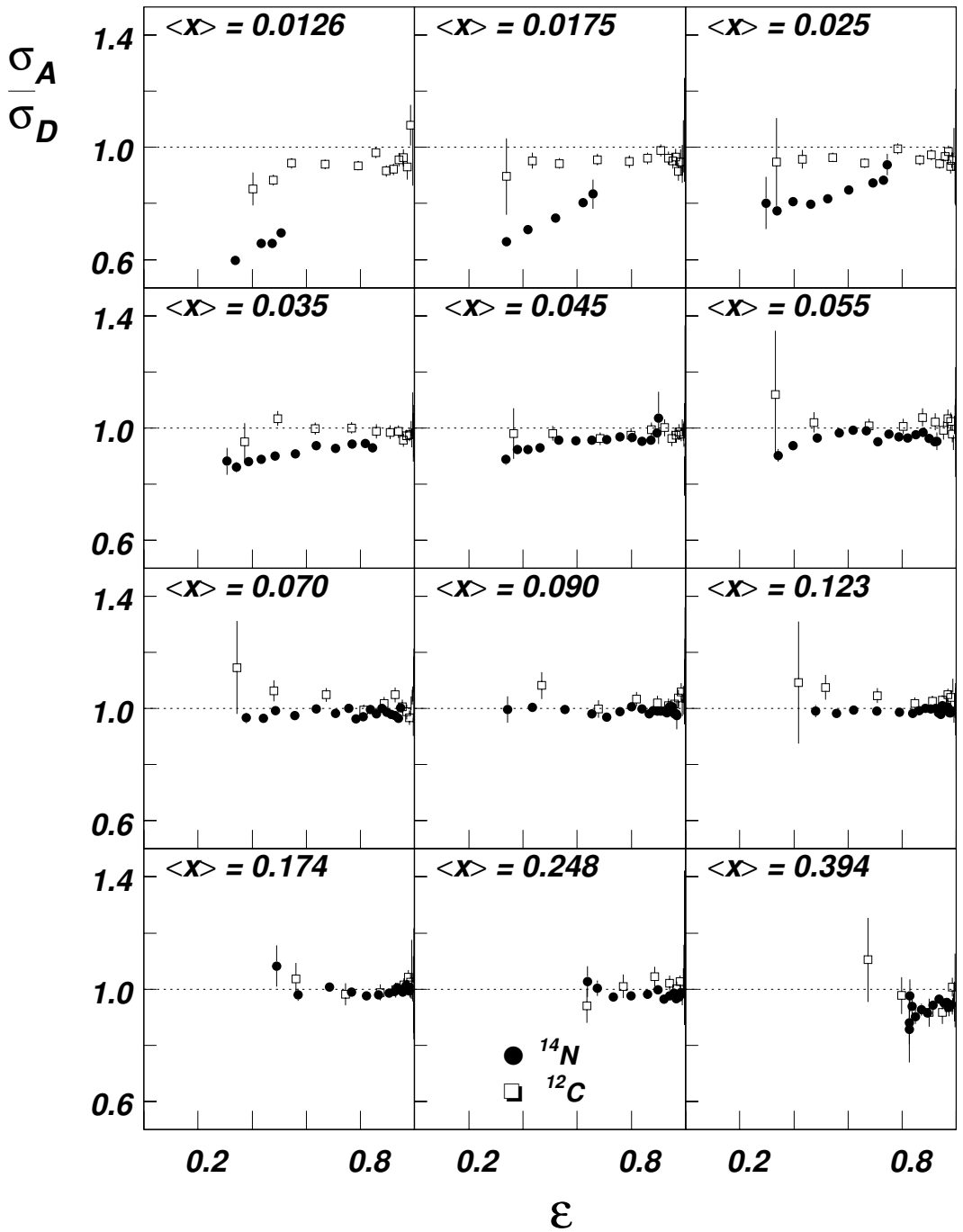

Figure 5.7: Ratio of the cross sections per nucleon as a function of ϵ for different x-regions. The HERMES data on ^{14}N are represented by solid circles, the NMC data on ^{12}C by open squares.

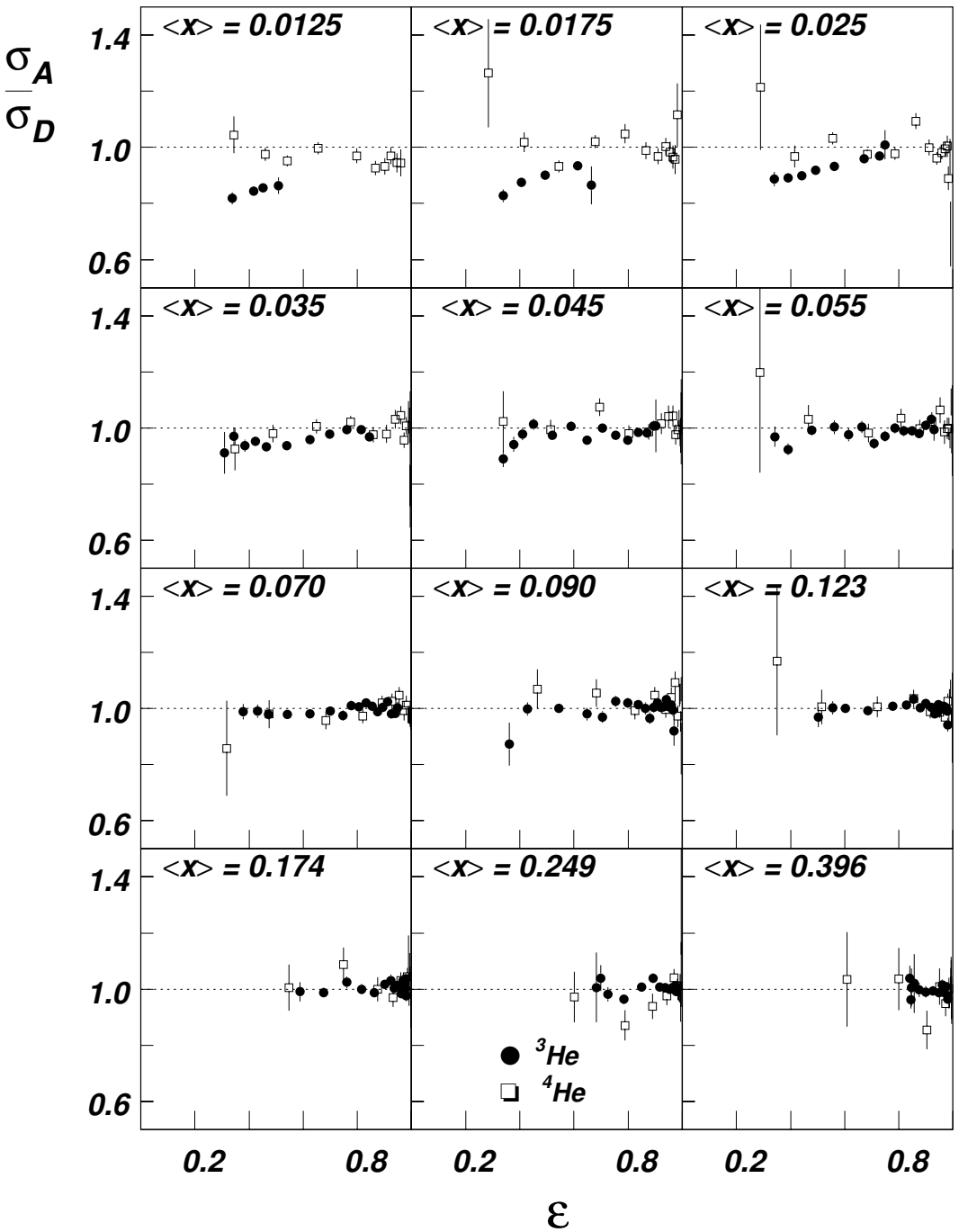

Figure 5.8: Ratio of the cross sections per nucleon as a function of ϵ for different x-regions. The HERMES data on ^{3}He are represented by solid circles, the NMC data on ^{4}He by open squares.

^{14}N than for ^{3}He, originating mainly from the difference in the elastic form-factor of the two nuclei (section 5.2.4). The size of the radiative corrections is largest in the lowest x-bin, where it amounts to 0.552, 0.461 and 0.372 for ^{2}H, ^{3}He and ^{14}N, respectively.

To ensure that the observed difference between the NMC and HERMES data is not due to an incorrect evaluation of the radiative corrections, several cross checks have been performed. These are presented in detail in ref. [58], and are summarized below.

- The NMC data were corrected using the same software (TERAD) as was used for the HERMES data. The radiative corrections for the NMC data were verified by NMC by comparing the inclusive cross section results to results where an additional hadron was detected (thus making sure that the event was not elastic or quasi-elastic). As the radiatively corrected inclusive data agreed well (within 1%) with the 'hadron tagged' data, it was concluded that the corrections were well evaluated [1].

  The radiative corrections can be large. At x values around 0.001 the correction for the NMC C/D ratio is 33%. The corrections decrease rapidly with increasing x, at x around 0.01 the correction to the C/D ratio is less than 2%. At HERMES electrons were used (muons at NMC), resulting in larger radiative corrections. However, the increase of the radiative corrections due to the lower mass of the electron is partly compensated by the lower beam energy at HERMES. For $x \approx 0.01$ the correction to the ratio ^{14}N/D (^{3}He/D) is of similar size as that of the lowest NMC data points, i.e. smaller than 32% (12%).

- The results of the TERAD computer program were compared with results from the POLRAD [62] program. Both results are consistent to within 1% over the entire x range.

- The results of the TERAD computer program were also compared with results from FERRAD, an older program based on an alternative approach [63]. Both results are consistent to within 2% over the entire x range.

[1] Such a cross check could not be carried out for the HERMES data as the hadron tagged events suffer from an additional physics effect, as described in chapter 6.

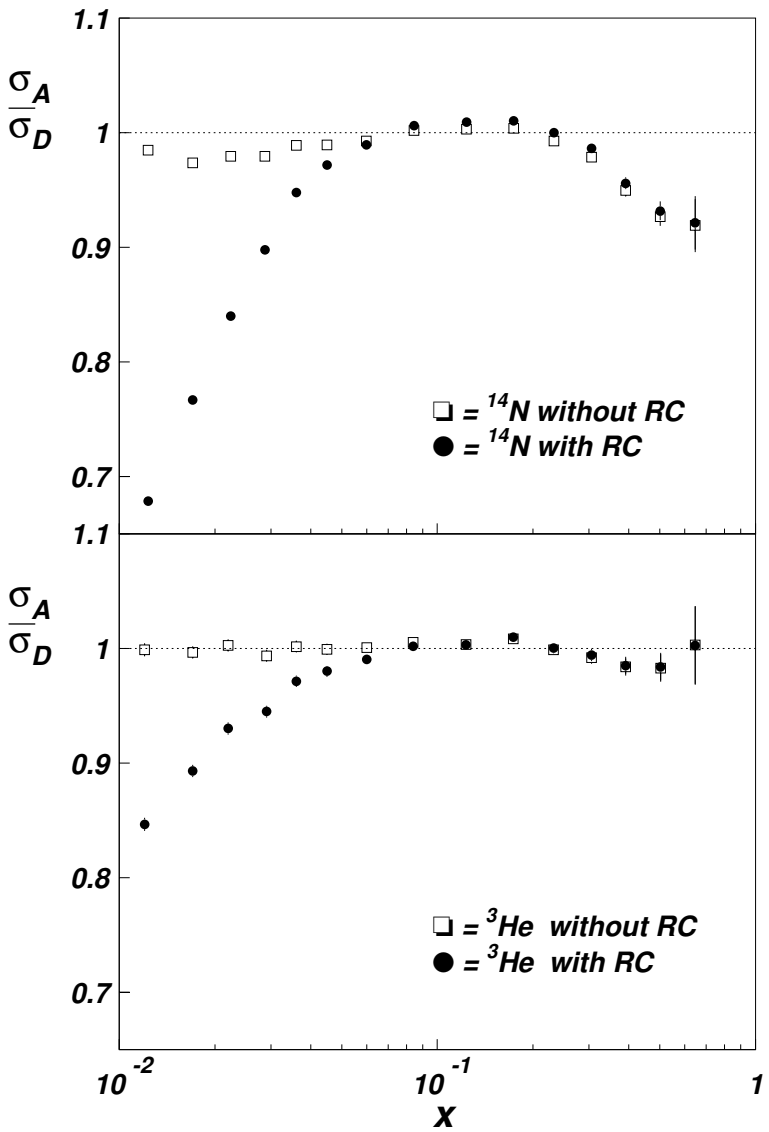

Figure 5.9: Ratio of the cross sections per nucleon as a function of x with and without radiative corrections for ^{14}N (upper panel) and ^{3}He (lower panel).

- Finally, in order to make sure that the calculated radiative correction factors are applied correctly, the HERMES data were analyzed independently at two institutes that are part of the HERMES collaboration (MIT and NIKHEF). The results are found to be consistent within 0.5% (the small difference originates from a slightly different treatment of events with more than one positron candidate). This check also rules out mistakes in the analysis software, since different programs were used.

Reproducibility

In order to investigate the stability of the ^{14}N results during the 1997 data taking period, the cross section ratio σ_N/σ_D was determined for three different time intervals. The results are shown for the three intervals separately and for all the data together in figure 5.10. During periods 1 and 2, which covered several months, data were collected with a low luminosity of about 1×10^{32} nucleons/cm^{2}s. For period 3, which covered one week at the end of the 1997 data taking period, the target density was increased such that luminosities as high as 1.3×10^{33} nucleons/cm^{2}s were reached. Figure 5.10 shows that the normalization of the results in periods 1, 2, and 3 deviates from the result where all the data are used by about 1.5%.

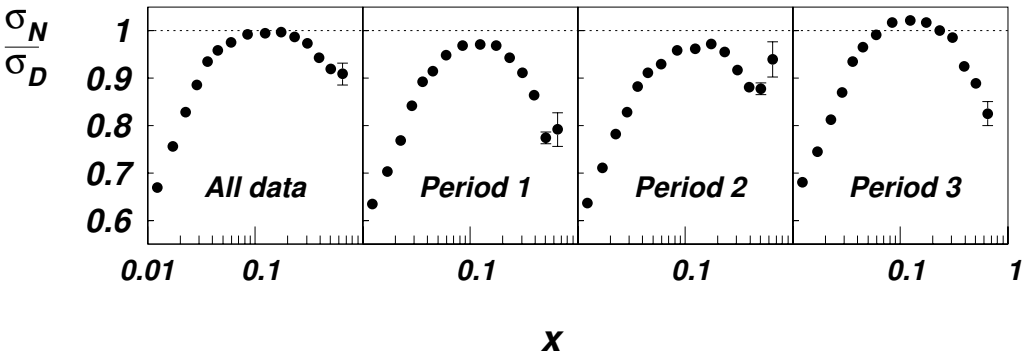

Figure 5.10: The cross section ratio as measured during 3 different time periods in 1997, as well as the ratio determined for all the data together. The difference between the results for the different periods and the result for all the data has been used to determine the uncertainty in the normalization of 1.5%.

It is known that at the end of a HERA fill the normalized yield (DIS event rate per unit of luminosity) is lower than at the beginning of that fill. At the end of a fill the coincidence rate of the luminosity monitor is lower due to the lower positron beam current, while the background due to random coincidences and target gas remnants in the beamline remains constant. This is a small (few %) effect that usually cancels (or can be neglected) in asymmetry or ratio measurements.

Using a low target density has the same effect as end-of-fill running. Since a large part of the nitrogen data collected in periods 1 and 2 was taken at a target density of 0.5×10^{15} nucleons/cm^2, while the deuterium data were taken at an average density of 2×10^{15} nucleons/cm^2, a correction is needed. The correction factor can be determined by using the nitrogen data which were collected during period 3, at target densities between 0.7 and 7.4 $\times 10^{15}$ nucleons/cm^2, averaging to 2.8 $\times 10^{15}$ nucleons/cm^2. In this period the average value of the N_2 target density was about the same as that used for the deuterium data taking. When taking the ratio of the nitrogen data from period 3 and all the deuterium data, the effect of the dependence of the normalized yield on the target density cancels. By comparing the results of the 1^{st} and 2^{nd} period to the 3^{rd} period a correction factor was obtained. When applied to the full data set, the correction factor to the $\sigma_{^{14}N}/\sigma_D$ ratio equals 1.014.

As an estimate of the normalization uncertainty we use the average deviation of period 1, 2, and 3 with respect to all the data, which equals 1.5%. This normalization error is already included in the results which were presented in the previous section.

5.3 Extraction of $R_{^{14}N}/R_D$ and $R_{^3He}/R_D$

As suggested by the ϵ-dependence of the data, the difference in the cross section ratio of the HERMES and NMC (and E665) experiment can possibly be explained by an A-dependence of $R = \sigma_L/\sigma_T$ (also see Eq. (2.23)).

An A-dependence of R is not necessarily inconsistent with the E665 and NMC data, since the Q^2 region covered in these experiments is different. At x values around 0.01 the average Q^2 at HERMES is about 0.5 GeV^2, while for NMC and E665 the value for Q^2 is a few GeV^2. For the low x-region probed by HERMES there are no measurements of $R_A - R_D$ available at

sufficiently low Q^2 to constrain possible deviations of R_A from R_D.

The data are distributed over a large ϵ range, and are therefore sensitive to a possible A-dependence of R. In this section values for $R_{^{14}N}/R_D$ and $R_{^3He}/R_D$ are extracted using the dependence of the cross section ratio on ϵ, as expressed by Eq. (2.23).

Using $R_A/R_D = k(x_i, Q_i^2)$, with x_i the average x and Q_i^2 the average Q^2 in a given x-region labeled by (i), Eq. (2.23) can be written as,

$$\frac{\sigma_A}{\sigma_D} = \frac{F_2^A}{F_2^D} \frac{(1+\epsilon R_D k(x_i,Q_i^2))(1+R_D)}{(1+R_D k(x_i,Q_i^2))(1+\epsilon R_D)}. \tag{5.1}$$

The data in each x-region from figures 5.7 and 5.8 has been fitted using Eq. (5.1), resulting in 12 values for $k(x_i, Q_i^2)$, one for each x-region. These constants are associated with the average Q^2 and x value of the data in each x-region. The only external input which is needed for the fit is a parametrization of R_D, for which R1998 [19] has been used [2]. The free parameters in the fit of the ^{14}N (^{3}He) data are $F_2^{^{14}N}/F_2^D$ and $R_{^{14}N}/R_D$ ($F_2^{^3He}/F_2^D$ and $R_{^3He}/R_D$). It is assumed that the ratios R_A/R_D and F_2^A/F_2^D do not vary with Q^2 within each x-region. At NMC [15] the Q^2-dependence of the ratio $F_2^{^{12}C}/F_2^D$ was determined experimentally, and no dependence was found in the explored x and Q^2 region ($0.0035 < x < 0.60$ and $0.60 < Q^2 < 41$ GeV^2) [3]. The assumed Q^2-independence of R_A/R_D within each x-bin is discussed in more detail below.

The results of the fits for the HERMES data are shown in figures 5.11 and 5.12. The errors shown in these figures represent the statistical errors only. For the NMC data on ^{12}C and ^{4}He fits have been performed as well, resulting in different values for $k(x_i, Q_i^2)$, but the average Q^2 associated with these values is much higher, due to the higher beam energy used at NMC. The results of the fits of the NMC data are shown in figures 5.13 and 5.14.

[2] As alternative R1990 [50] could have been used as parametrization of R_D, but we prefer to use R1998 [19] as it is based on a larger data set, extends to lower Q^2 and is of higher precision.

[3] It is noted that the Q^2-dependence of F_2^A/F_2^D is not measured for exactly the same (x,Q^2)-combination as covered by HERMES. Furthermore, it is noted that for F_2^{Sn}/F_2^C a significant Q^2-dependence was found which may be consistent with pQCD [30].

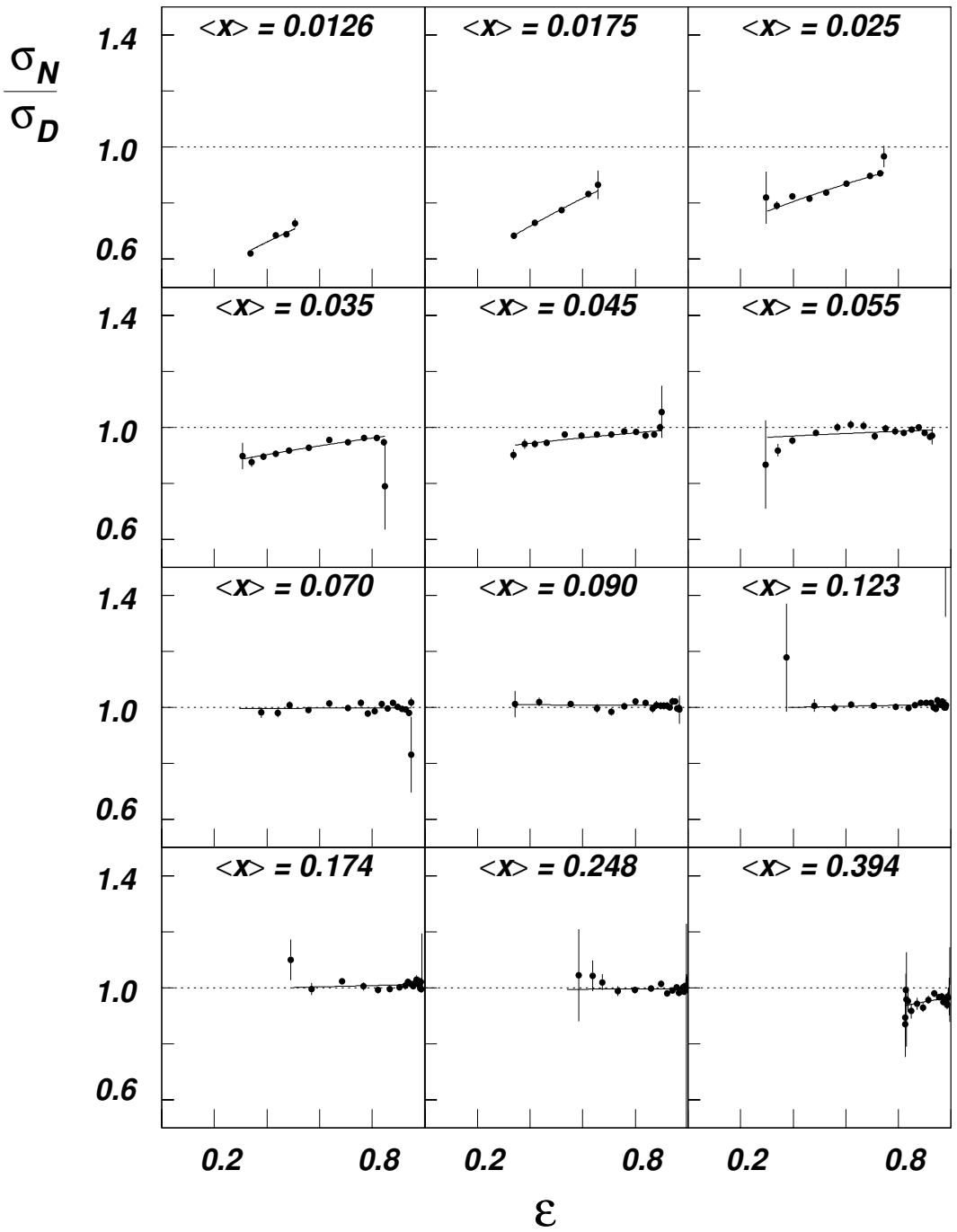

Figure 5.11: Ratio of the cross section per nucleon for $^{14}N/D$ as a function of ϵ compared to the fit results based on Eq. (5.1).

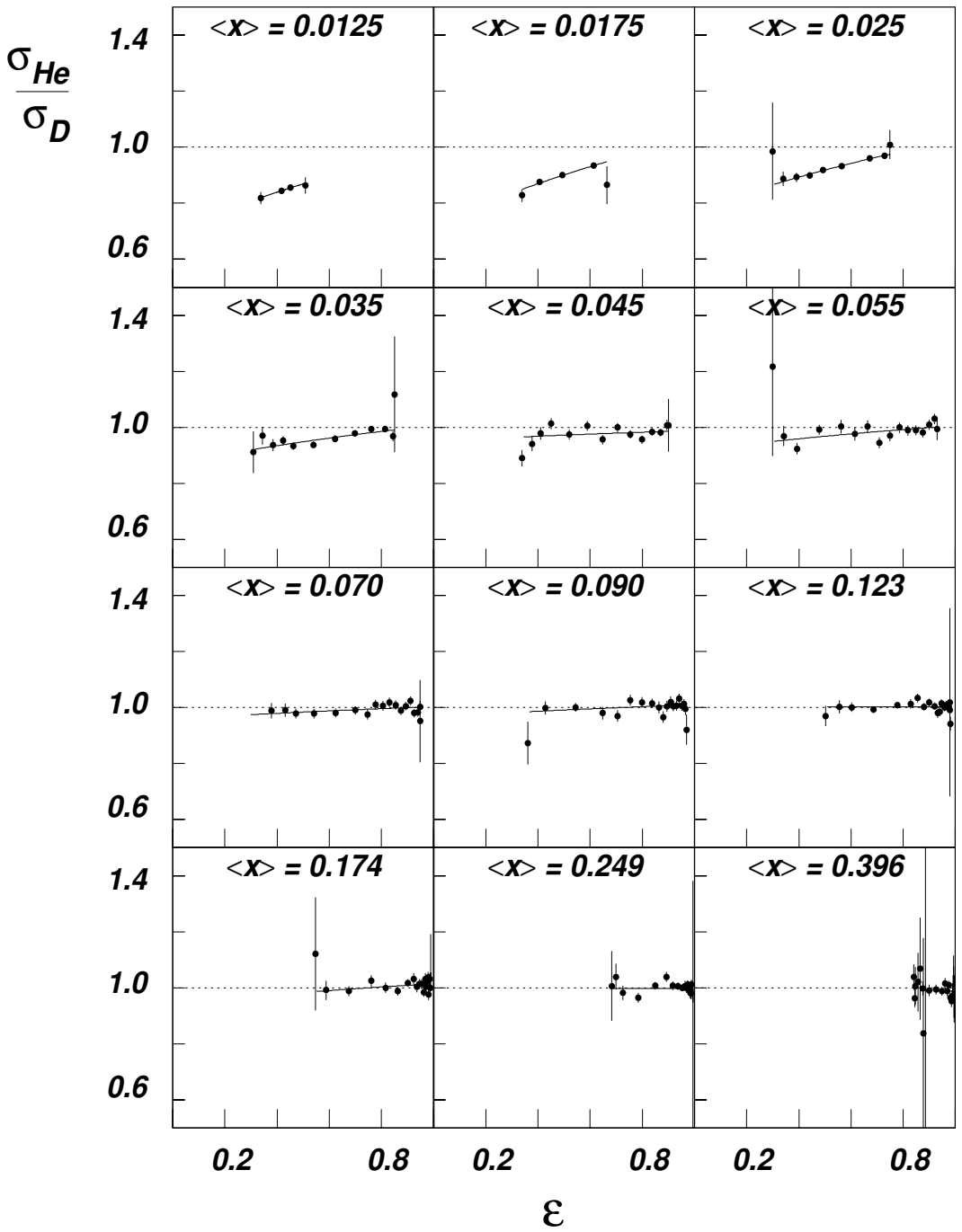

Figure 5.12: Ratio of the cross section per nucleon for $^3He/D$ as a function of ϵ compared to the fit results based on Eq. (5.1).

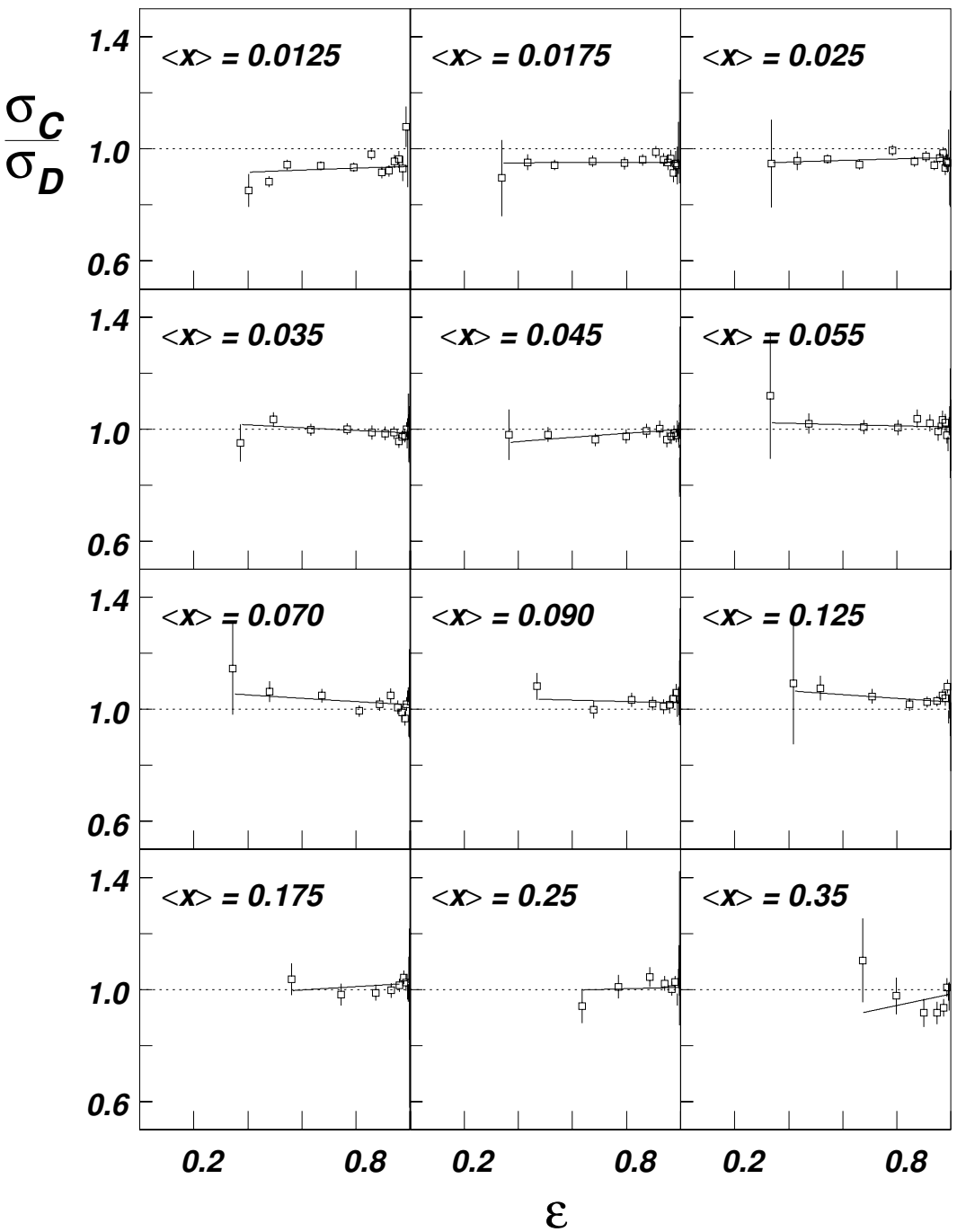

Figure 5.13: Ratio of the cross section per nucleon for the NMC data on $^{12}C/D$ as function of ϵ compared to the fit results based on Eq. (5.1).

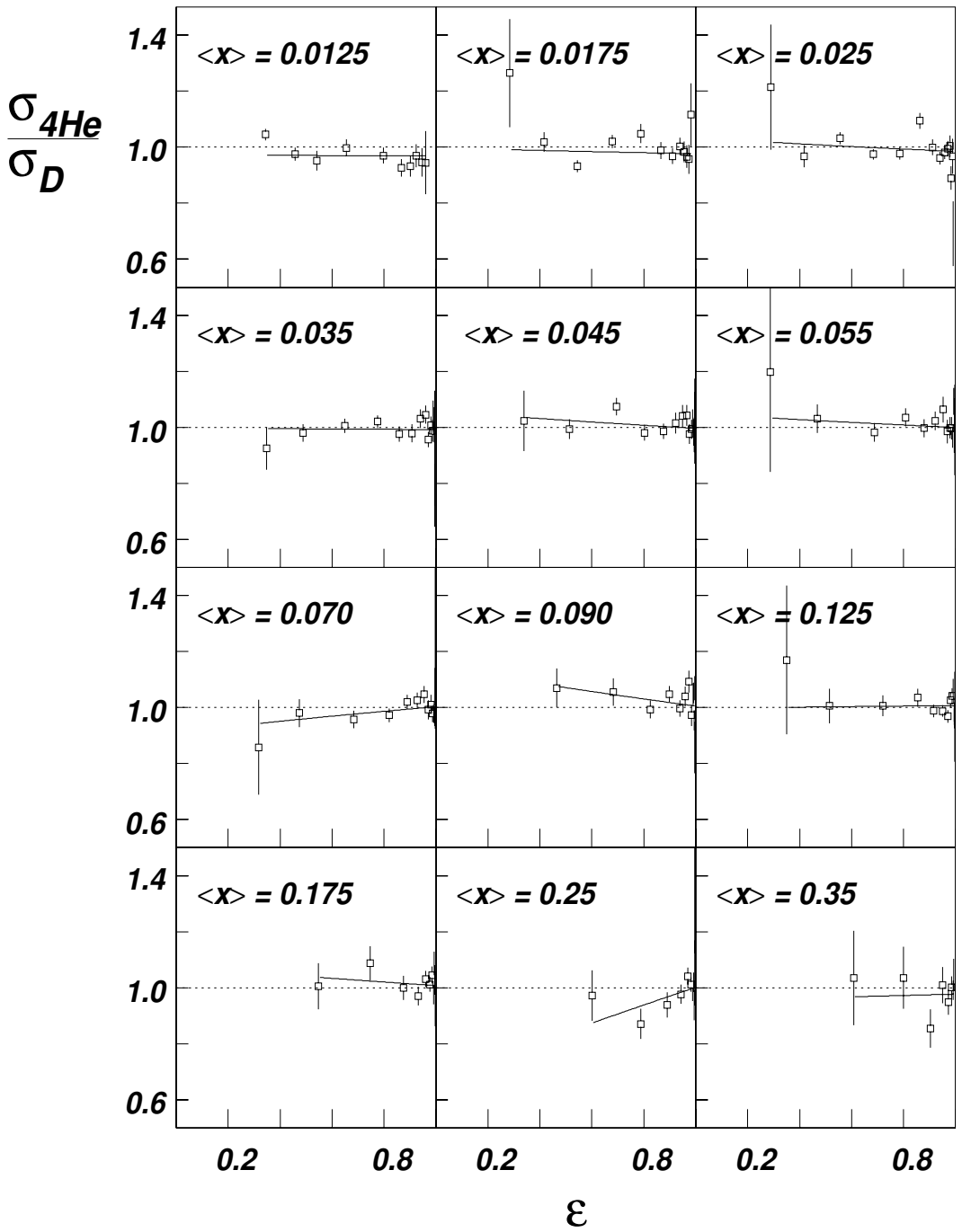

Figure 5.14: Ratio of the cross section per nucleon for the NMC data on $^4He/D$ as function of ϵ compared to the fit results based on Eq. (5.1).

From figures 5.11-5.14 it is seen that the assumed A-dependence of R results in a good description of all available data. The shown error bars represent the statistical uncertainty only. The χ^2 values per degree of freedom are close to unity for all the fits (considering statistical errors only).

As a cross check of the procedure, the fits as a function of ϵ have been performed in three different ways, which are listed below.

Fit A: Two fit parameters: F_2^A/F_2^D and R_A/R_D.

Fit B: Two fit parameters: R_A/R_D and a bounded normalization parameter N_f, representing possible differences in the normalization of the HERMES and NMC data. The fit equation used is given by:

$$\frac{\sigma_A}{\sigma_D} = N_f \frac{F_2^A}{F_2^D} \frac{(1+\epsilon R_D k(x_i,Q_i^2))(1+R_D)}{(1+R_D k(x_i,Q_i^2))(1+\epsilon R_D)}, \tag{5.2}$$

where for $F_2^{14_N}/F_2^D$ (F_2^{3He}/F_2^D) the NMC parametrization of $F_2^{12_C}/F_2^D$ (F_2^{4He}/F_2^D) is used and N_f is allowed to vary between 0.97 and 1.03.

Fit C: The results of the first two fit methods show that R_A/R_D is a fairly steep function of Q^2 in the first six x-regions. The fits for these six x-bins have been repeated but now allowing for a Q^2-dependence of R_A/R_D within each x-region. In Eq. (5.2), $k(x_i,Q_i^2)$ is replaced by $k_1 + k_2(Q^2 - Q_i^2)$. This fit procedure has three free parameters, k_1, k_2 and N_f, and allows to investigate any remaining Q^2-dependence of R_A/R_D within each x-bin.

The results of the fits using the different methods are listed for ^{14}N in tables 5.3, 5.4 and 5.5 and for ^{3}He in tables 5.6, 5.7 and 5.8. For each fit parameter two errors are listed. The 'fit' error includes the effect of the statistical uncertainty in the cross section ratios and the error due to correlations between the fit parameters. The 'systematic' error includes uncertainties due to the radiative corrections and the normalization error, which are summed quadratically. The latter error is evaluated by determining the maximum and minimum values of the cross section ratio, which are used to extract the maximum and minimum values of the fit parameters, F_2^A/F_2^D and R_A/R_D.

The deviation of the fit parameters, relative to the central value, is represented in the tables in the column 'sys'. The uncertainty in R_A/R_D due to the errors included in the R1998 parametrization is smaller than 1%, and can thus be neglected compared to the other errors. It has also been verified that using an alternative parametrization for R_D (R1990 [50]) does not change the values of R_A/R_D significantly. Note that the errors listed for method C only include the 'fit' error as defined above. By comparing table 5.4 and table 5.5, we estimate that the systematic error of the fit parameters for method C is of similar size as the quoted 'fit' error.

The fit methods, A and B give within errors very similar results for R_A/R_D, giving confidence in the extraction of this ratio from the ϵ-dependence of the cross section ratio. Method A is preferred as it is based on HERMES data only, supplying us with results for $R_{^{14}N}/R_D$ and $R_{^3He}/R_D$, as well as results for the structure function ratios, $F_2^{^{14}N}/F_2^D$ and $F_2^{^3He}/F_2^D$.

Table 5.3: Fit results for the ^{14}N cross section ratios: method A, with R_A/R_D and F_2^A/F_2^D as free parameters.

i	x	Q^2	$\frac{R_{^{14}N}}{R_D}$	$\Delta\frac{R_{^{14}N}}{R_D}$		$\frac{F_2^{^{14}N}}{F_2^D}$	$\Delta\frac{F_2^{^{14}N}}{F_2^D}$	
				fit	sys		fit	sys
1	0.0125	0.500	4.78	0.86	0.44	0.895	0.032	0.058
2	0.0175	0.669	4.92	0.44	0.13	0.984	0.015	0.038
3	0.025	0.885	2.76	0.17	0.07	0.973	0.009	0.028
4	0.035	1.138	1.71	0.11	0.01	0.986	0.007	0.020
5	0.045	1.353	1.42	0.10	0.00	0.997	0.006	0.018
6	0.055	1.534	1.18	0.10	0.00	0.993	0.006	0.016
7	0.070	1.758	1.02	0.08	0.00	0.999	0.005	0.016
8	0.090	2.018	0.99	0.11	0.00	1.008	0.006	0.016
9	0.123	2.341	1.09	0.13	0.00	1.011	0.005	0.016
10	0.174	2.702	1.14	0.20	0.00	1.012	0.004	0.016
11	0.248	3.096	1.04	0.28	0.00	0.997	0.003	0.015
12	0.394	4.469	3.14	1.43	0.02	0.967	0.005	0.015

Table 5.4: Fit results for the ^{14}N cross section ratios: method B, with R_A/R_D as free parameter and N_f as bounded parameter.

i	x	Q^2	$\frac{R_{14_N}}{R_D}$	$\Delta\frac{R_{14_N}}{R_D}$		N_f	ΔN_f
				fit	sys		fit
1	0.0125	0.500	6.12	0.26	2.21	0.972	0.012
2	0.0175	0.669	5.41	0.34	0.89	1.025	0.008
3	0.025	0.885	2.91	0.18	0.45	0.995	0.009
4	0.035	1.138	1.71	0.11	0.13	0.995	0.007
5	0.045	1.353	1.38	0.10	0.11	0.995	0.006
6	0.055	1.534	1.13	0.09	0.13	0.984	0.006
7	0.070	1.758	0.98	0.08	0.12	0.984	0.005
8	0.090	2.018	0.97	0.11	0.13	0.987	0.006
9	0.123	2.341	1.08	0.13	0.16	0.987	0.005
10	0.174	2.702	1.14	0.20	0.21	0.992	0.004
11	0.248	3.096	1.05	0.28	0.32	0.989	0.003
12	0.394	4.469	3.10	1.42	1.42	0.995	0.005

Table 5.5: Fit results for the ^{14}N cross section ratios: method C, with k_1 and k_2 as free parameters and N_f as bounded parameter.

i	x	Q^2	$k = k_1 + k_2(Q^2 - Q_i^2)$					
			k_1	Δk_1	k_2	Δk_2	N_f	ΔN_f
1	0.0125	0.500	6.12	0.86	-2.04	2.2	0.97	0.05
2	0.0175	0.669	5.52	0.68	-0.61	2.5	1.03	0.04
3	0.025	0.885	3.83	0.16	-2.31	0.48	1.03	0.01
4	0.035	1.138	1.29	0.22	0.63	0.37	0.97	0.05
5	0.045	1.353	0.89	0.14	0.61	0.19	0.97	0.04
6	0.055	1.534	0.73	0.08	0.45	0.12	0.97	0.01

The results of method C allow us to investigate whether the assumption entering method A and B, i.e. that R_A/R_D is independent of Q^2 within each x-region, is valid. As R_A/R_D only deviates from unity in the first 6 x-regions, only these bins have been investigated. In order to be mutually consistent the parameter k_2 must be negative since the deviation of R_A/R_D decreases with Q^2. If $k_2 > 0$ the obtained value k_2 must be considered as a measure of the systematic uncertainty in this variable. From tables 5.5 and 5.8 it is seen that the value of k_2 is either consistent with zero, or positive (with one exception) indicating that the data give no evidence for a significant Q^2-dependence within each x-region. Moreover, this conclusion is confirmed by the fact that the fitted values of k_1 in most cases agree (within errors, including our estimate of the systematic error on k_1) with the R_A/R_D values found with method A and B.

Table 5.6: Fit results for the ^{3}He cross section ratios: method A, with R_A/R_D and F_2^A/F_2^D as free parameters.

i	x	Q^2	$\frac{R_{^3He}}{R_D}$	$\Delta\frac{R_{^3He}}{R_D}$		$\frac{F_2^{^3He}}{F_2^D}$	$\Delta\frac{F_2^{^3He}}{F_2^D}$	
				fit	sys		fit	sys
1	0.0125	0.498	2.60	1.09	0.23	0.994	0.080	0.056
2	0.0175	0.660	2.57	0.41	0.05	1.032	0.029	0.037
3	0.025	0.872	2.17	0.22	0.05	1.024	0.015	0.029
4	0.035	1.117	1.58	0.15	0.01	1.006	0.011	0.019
5	0.045	1.322	1.15	0.13	0.00	0.989	0.010	0.015
6	0.055	1.493	1.37	0.15	0.00	1.006	0.009	0.013
7	0.070	1.699	1.19	0.13	0.00	1.003	0.007	0.012
8	0.090	1.903	1.19	0.16	0.00	1.010	0.007	0.011
9	0.124	2.167	1.01	0.16	0.00	1.003	0.005	0.011
10	0.174	2.496	1.39	0.31	0.00	1.015	0.006	0.011
11	0.249	2.862	0.98	0.39	0.00	0.997	0.005	0.011
12	0.396	4.241	0.43	1.22	0.01	0.986	0.007	0.011

The values (method A) for R_A/R_D as a function of the average Q^2 are shown in figure 5.15 for four different x-regions (this representation was copied from ref. [19]). The shown uncertainty in R_A/R_D represents the quadratic sum of the uncertainty due to the radiative corrections and the nor-

Table 5.7: Fit results for the ^{3}He cross section ratios: method B, with R_A/R_D as free parameter and N_f as bounded parameter.

i	x	Q^2	$\frac{R_{^3He}}{R_D}$	$\Delta\frac{R_{^3He}}{R_D}$		N_f	ΔN_f
				fit	sys		fit
1	0.0125	0.498	2.28	0.36	0.65	1.029	0.053
2	0.0175	0.660	1.88	0.13	0.43	1.029	0.038
3	0.025	0.872	1.86	0.12	0.28	1.030	0.039
4	0.035	1.117	1.65	0.17	0.17	1.023	0.010
5	0.045	1.322	1.27	0.16	0.16	1.001	0.011
6	0.055	1.493	1.32	0.19	0.19	1.001	0.011
7	0.070	1.699	1.33	0.16	0.16	1.003	0.008
8	0.090	1.903	0.99	0.20	0.20	0.999	0.010
9	0.124	2.167	0.95	0.22	0.22	0.995	0.008
10	0.174	2.496	1.54	0.52	0.52	1.000	0.012
11	0.249	2.862	1.74	0.80	0.80	1.010	0.012
12	0.396	4.241	0.54	1.00	7.80	1.024	0.008

Table 5.8: Fit results for the ^{3}He cross section ratios: method C, with k_1 and k_2 as free parameters and N_f as bounded parameter.

i	x	Q^2	$k = k_1 + k_2(Q^2 - Q_i^2)$					
			k_1	Δk_1	k_2	Δk_2	N_f	ΔN_f
1	0.0125	0.498	1.78	0.40	1.65	2.02	0.98	0.05
2	0.0175	0.660	1.21	0.39	2.20	1.47	0.97	0.05
3	0.025	0.872	1.85	0.37	0.12	0.75	1.03	0.05
4	0.035	1.117	1.45	0.52	0.32	0.89	1.01	0.05
5	0.045	1.322	1.12	0.46	0.19	0.52	0.99	0.02
6	0.055	1.493	1.57	0.57	-0.25	0.55	1.01	0.02

malization, and the error from the fit ("sys" and "fit" in tables 5.3 and 5.6).

The values (method A) for $F_2^{^{14}N}/F_2^D$ and $F_2^{^3He}/F_2^D$ are shown in figure 5.16 as a function of x, together with parametrizations of the NMC and SLAC results for $F_2^{^{12}C}/F_2^D$ and $F_2^{^4He}/F_2^D$. From figure 5.16 it is seen that the values that we obtained for $F_2^{^{14}N}/F_2^D$ and $F_2^{^3He}/F_2^D$, while extracting R_A/R_D, are consistent with the results from SLAC and NMC for carbon and helium-4. The precision at low x is not very high due to the fact that the data for these x values have been collected at relatively low values of ϵ, while the value of F_2^A/F_2^D corresponds to the intercept at ϵ=1 (figures 5.11 and 5.12). The effective extrapolation to ϵ=1 carried out by the fit, leads to a large error bar. However, it is gratifying to observe that the method used to extract values for R_A/R_D also supplies data on $F_2^{^{14}N}/F_2^D$ and $F_2^{^3He}/F_2^D$ which are consistent with existing data on neighboring nuclei. It is noted that differences between ^{14}N and ^{12}C are expected to be about 2-3% on the basis of existing parametrizations of data on nuclear effects in F_2 ratios [2]. These differences are smaller than the uncertainty of the data.

Before drawing any further conclusions, we need to investigate whether our results on $R_{^{14}N}/R_D$ and $R_{^3He}/R_D$ are not inconsistent with previous data on R_A/R_D. The existing measurements of $R_A - R_D$ can be used to extract a value for R_A/R_D using the R1998 [19] parametrization which was determined using mainly hydrogen and deuterium data. The recent measurement of R_C at SLAC [19] for low x values are also converted to R_A/R_D but the errors increase considerably due the uncertainty in R1998. The world data [4] on R_A/R_D is shown together with the fit results of HERMES ($R_{^{14}N}/R_D$, $R_{^3He}/R_D$) and NMC ($R_{^{12}C}/R_D$,$R_{^4He}/R_D$) in figure 5.17. From figure 5.17 it is concluded that the currently observed A-dependence of R is not inconsistent with previous data at larger values of Q^2 and x. At low values of x ($x < 0.06$) and Q^2 ($Q^2 < 1.5$ GeV^2) a strong enhancement of R_A is observed with respect to R_D, which is rising with decreasing values of Q^2.

[4] The Sn and Ca data from NMC were measured relative to carbon, and were converted to R_{Sn}/R_D and R_{Ca}/R_D using $(R_A - R_C + R1998)/R1998$, which is equal to R_A/R_D when $R_C = R_D$. If instead the measured values of $R_C - R_D$ would have been used, the error bars would have been unreasonably large. Moreover, as none of the converted data were collected in a domain where $R_A \neq R_D$ (with the possible exception of the Ca/D data point at $Q^2 = 1$ GeV^2), the chosen assumption gives most credit to the precision of the existing data.

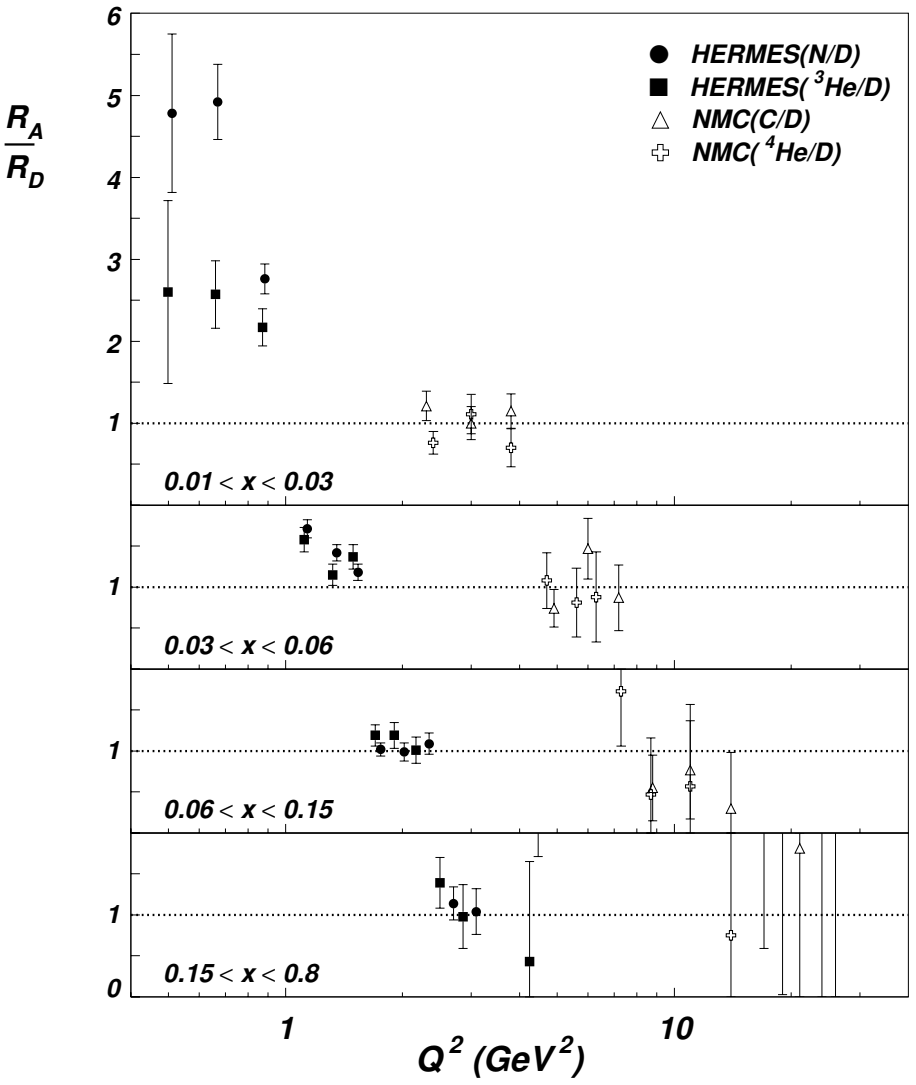

Figure 5.15: The values of R_A/R_D as a function of Q^2 for A=3,4,12 and 14. The errors bars on the data represent the fit errors and the systematic errors added in quadrature. The systematic error arises from the radiative corrections and a normalization error of 1.5%. The error due to the uncertainty in the R1998 parametrization is smaller than 1%. The open symbols have been derived from the NMC data using method B, with N_f=1.

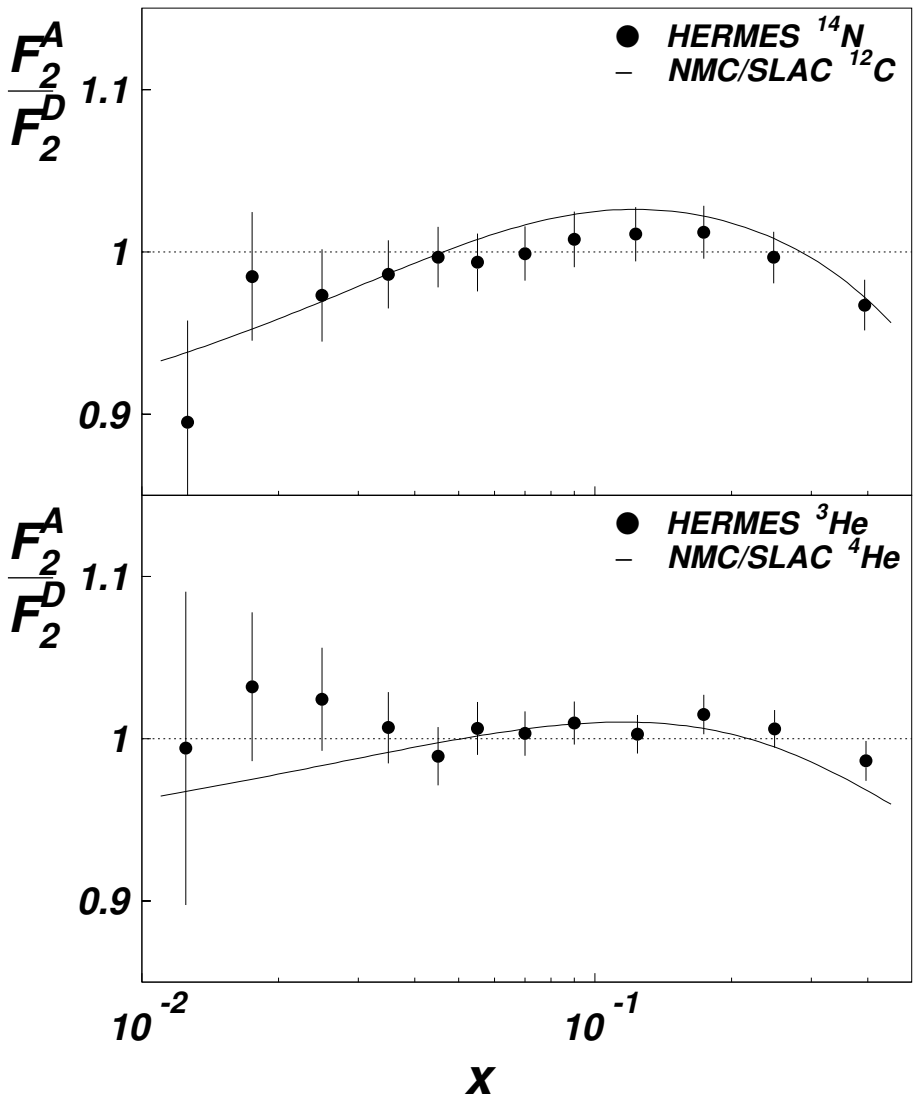

Figure 5.16: The values of F_2^N/F_2^D and $F_2^{^3He}/F_2^D$ as function of x. The errors bars on the data represent the fit errors and the systematic errors added in quadrature. The systematic uncertainty comprises that due to the radiative corrections and the normalization. The curves represent parametrizations of the NMC and SLAC data on ^{4}He and ^{12}C.

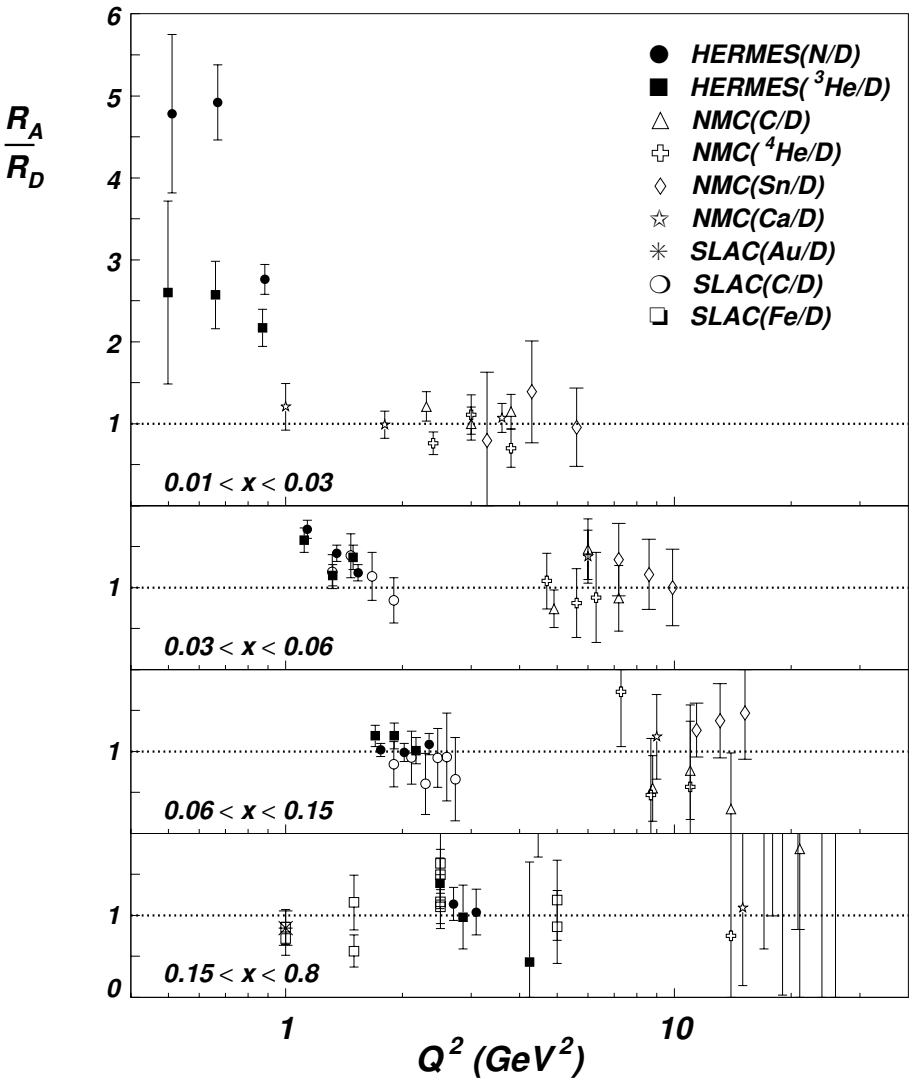

Figure 5.17: The values of R_A/R_D as a function of Q^2 together with the world data. The errors bars on the data include the fit errors as well as the systematic errors (summed quadratically). The systematic error arises from the radiative corrections and a normalization error of 1.5%. The error due to the uncertainty in R1998 is smaller than 1%.

5.4 Interpretation of the data

In this section a possible interpretation of the results on R_A/R_D is discussed. In the first subsection the A-dependence of R is studied, by comparing the $R_{^{14}N}/R_D$ and $R_{^3He}/R_D$ ratios. In the following subsection the A-dependence of R and F_2 is converted into the A-dependence of σ_T^A/σ_T^D and σ_L^A/σ_L^D, separately. In the last subsection possible models for an A-dependence of R are discussed.

5.4.1 The A-dependence of R

The values for $R_{^{14}N}/R_D$ and $R_{^3He}/R_D$ can be used to estimate the A-dependence of R. In order to determine the A-dependence in detail, results on R for more than two targets are needed. Here the A-dependence is derived from the results on two targets only, i.e. ^{3}He and ^{14}N. The disadvantage of this approach is the use of ^{3}He, which is not a 'standard' nucleus of typical density. The A-dependence is parametrized using

$$\left(\frac{R_{^{14}N}}{R_{^3He}}\right) = \left(\frac{A_{^{14}N}}{A_{^3He}}\right)^{\lambda} , \tag{5.3}$$

with λ as a free exponent that can be derived from the data (figure 5.15). The results are shown in figure 5.18. From this figure it can be seen that the exponent λ is consistent with zero, i.e. there is no significant A-dependence, for $Q^2 > 1$ GeV^2, while for the lowest values of Q^2 the exponent is consistent with $\frac{1}{3}$ suggesting a radius effect. However, the error bars are large and do not exclude an exponent of zero either. In order to determine the exact A-dependence of R, additional data on heavier targets are needed.

5.4.2 Results on σ_T^A/σ_T^D and σ_L^A/σ_L^D

Since F_2^A and R_A depend differently on the longitudinal and transverse DIS cross sections, the effect of the nuclear medium on σ_L and σ_T can be determined separately.

The cross section ratio as a function of ϵ can also be fitted with the following expression (as an alternative of Eq. (5.1)),

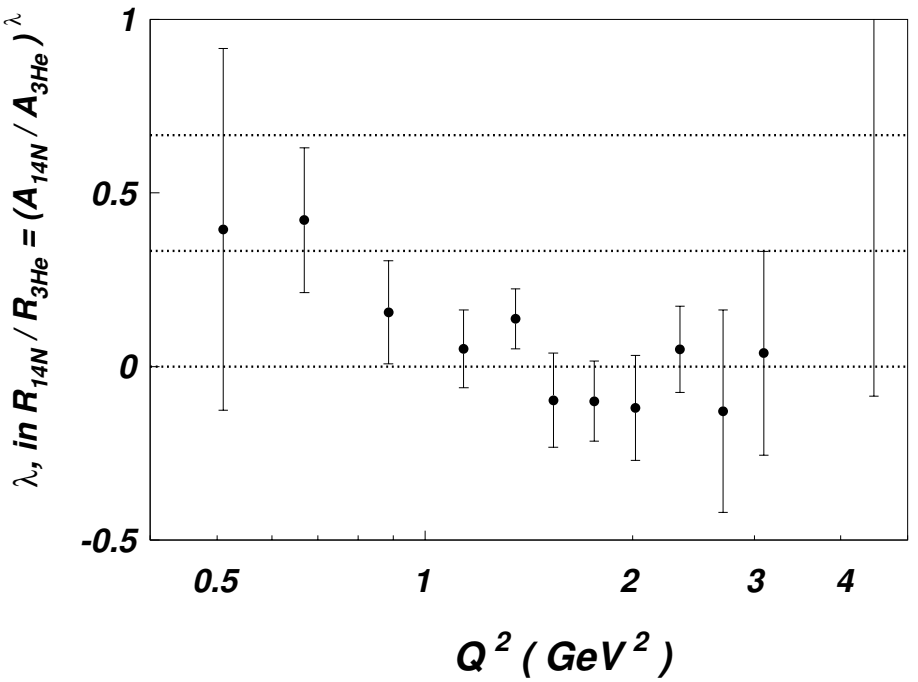

Figure 5.18: The A-dependence of R as a function of Q^2. The A-dependence is determined analytically from the R_N/R_D and R_{He}/R_D values as presented in figure 5.15. The errors include both the systematic and the statistical uncertainties.

$$\frac{\sigma_A}{\sigma_D} = \frac{\sigma_T^A + \epsilon\sigma_L^A}{\sigma_T^D + \epsilon\sigma_L^D} = \frac{\sigma_T^A/\sigma_T^D + \epsilon R_D \sigma_L^A/\sigma_L^D}{1 + \epsilon R_D}, \tag{5.4}$$

using the ratios σ_T^A/σ_T^D and σ_L^A/σ_L^D as free parameters. For R_D the R1998 [19] parametrization has been used. The results of the fit for the two parameters are shown in figure 5.19. From this figure it is seen that at low Q^2 the longitudinal cross section is enhanced in a nuclear medium, while the transverse cross section is reduced.

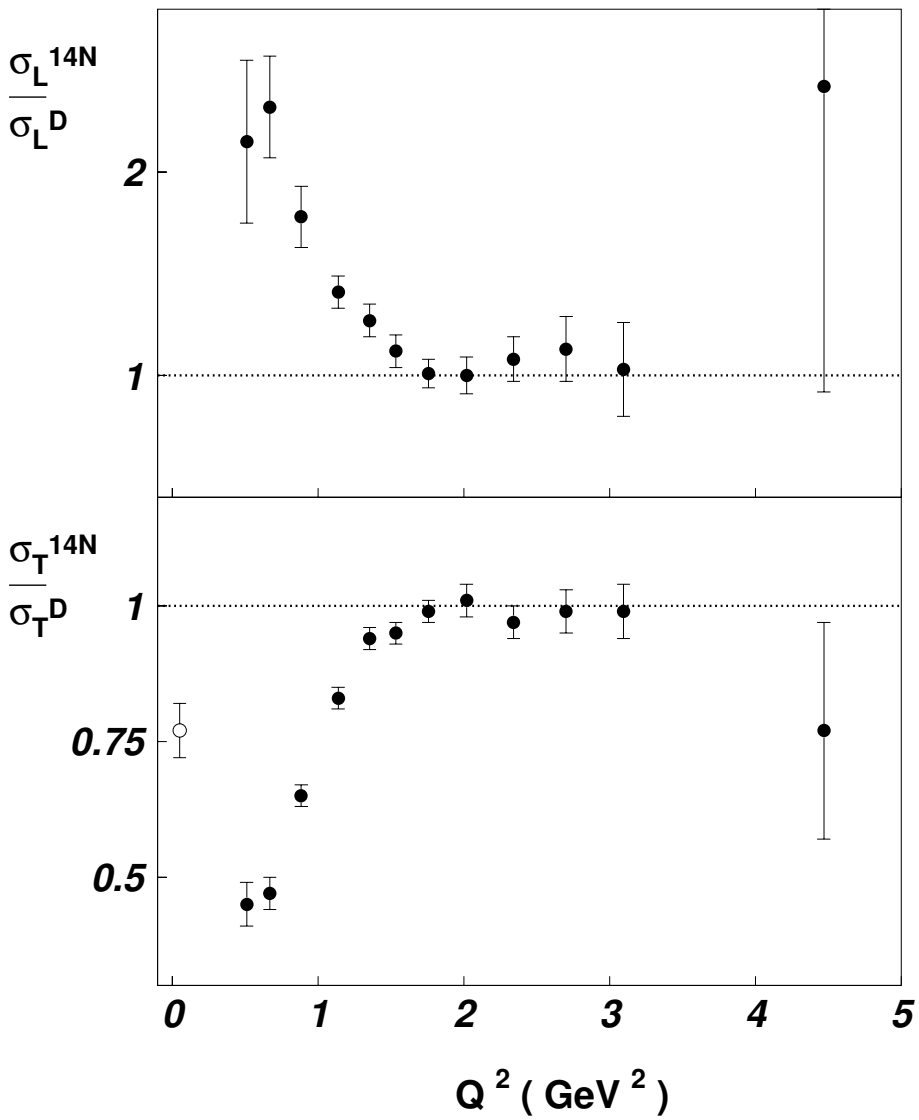

Figure 5.19: The HERMES result for σ_T^A/σ_T^D and σ_L^A/σ_L^D as a function of Q^2 (solid circles). Also a real photon result on ^{12}C is shown (open circle) [24, 64].

At higher values of Q^2 ($Q^2 > 1.5$ GeV^2) there is no effect of the nuclear medium on either the transverse or the longitudinal cross section [5].

Also displayed in figure 5.19 is a ^{12}C result from real-photon data [24, 64], which shows a considerably smaller shadowing effect at $Q^2 = 0$ GeV^2 than the virtual photon data at $Q^2 = 0.5$ GeV^2. A theoretical description of the transverse virtual photon data at low Q^2 should encompass the real photon data as well.

5.5 Models for a nuclear enhancement of R

The steep Q^2-dependence of the R_A/R_D data suggests an explanation in terms of a higher twist effect [3]. Higher twist effects arise due to interactions of the quark which absorbed the virtual photon with spectator quarks. These interactions are expected to decrease with Q^2 since at high Q^2 the time scale of the DIS interaction is very short. Such quark-gluon correlations are expected to be enhanced in the nuclear medium [4] due to interactions between the nucleons.

It has been suggested that higher twist effects give rise to $1/Q^2$ and $1/Q^4$ dependences [20, 3] of R. Therefore, the HERMES data at low x ($x < 0.06$) and Q^2 ($Q^2 < 1.5$ GeV^2) have been fitted as a function of Q^2, in terms of $1/Q^2$ and $1/Q^4$. The results of these fits are shown in figure 5.20. From this figure it is clear that a fit in terms of $1/Q^2$ describes the data well. The addition of a $1/Q^4$ term results in a steeper curve, describing the data slightly better. In the case where $R_{^{14}N}/R_D = a + b/Q^2$ the fit parameters are given by $a = 0.994$ and $b = 1.048$ GeV^2, while in the other case, where $R_{^{14}N}/R_D = a + b/Q^2 + c/Q^4$, the parameters are given by $a = 0.996$, $b = 0.763$ GeV^2, and $c = 0.242$ GeV^4.

Alternative mechanisms for a nuclear enhancement of R at small Q^2 have been proposed by several authors. It was suggested by Gousset and Pirner that the gluon distribution in leading twist may be enhanced in nuclei, which would give rise to $R_A > R_D$ [21]. This effect is expected to be of the order of 10%, too small for explaining the large A-dependence that we observe

[5] The uncertainty in the ratios for the highest Q^2 values ($Q^2 = 4.5$GeV^2) is very large. This is caused by the fact that the data that are used to determine these ratios, shown in the highest x-region (emc-effect region) of figure 5.7, have a very small ϵ range. This results in a large uncertainty in the fit parameters σ_T^A/σ_T^D and σ_L^A/σ_L^D.

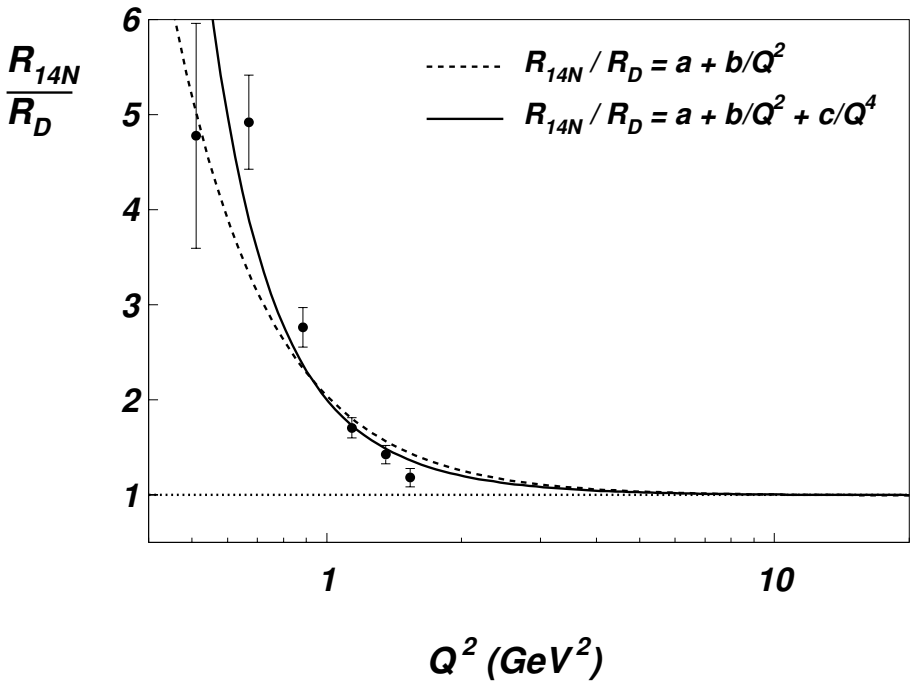

Figure 5.20: The values for R_{14_N}/R_D as a function of Q^2 for $0.01 < x < 0.06$. The curves represent fits with a twist-4 as well as a twist-6 term (solid), and a twist-4 term only (dashed).

presently. Generally, it is expected that such a leading twist effect is small [65, 66].

A very different mechanism was suggested in ref. [22], where a difference in nuclear shadowing for longitudinally and transversely polarized photons is shown to enhance R in a nucleus. An estimate of this effect for the HERMES kinematics suggests, however, that this mechanism leads to an increase of R_A relative to R_D which is smaller than 50% [23], not large enough for explaining the present data.

Soon after the discovery of the *EMC-effect* it was realized that higher twist effects may be important [67, 68]. Models in terms of diquarks, i.e. tightly bound quark pairs, were developed [69, 70], suggesting an enhancement of higher twist effects in nuclei.

5.6 Conclusion

Inclusive cross section ratios for nitrogen and helium with respect to deuterium have been measured, and compared with results from NMC and E665. At small x and Q^2 the HERMES results are found to be significantly lower. This difference is attributed to a nuclear enhancement of $R = \sigma_L/\sigma_T$, the ratio of the longitudinal and transverse virtual photon absorption cross sections. The ratios $R_{^{14}N}/R_D$ and $R_{^3He}/R_D$ have been determined in the kinematic region $0.01 < x < 0.8$ and $0.3 < Q^2 < 15$ GeV^2. At low values of x ($0.01 < x < 0.05$) these ratios reach a maximum value of 4.9 ± 0.5 and 2.6 ± 1.1 for nitrogen and helium, respectively.

The results of the analysis can also be expressed in terms of $\sigma_L^{^{14}N}/\sigma_L^D$ and $\sigma_T^{^{14}N}/\sigma_T^D$, separately. For the lowest (x, Q^2)-bin the fitted values are 2.15 ± 0.40 and 0.45 ± 0.04 for $\sigma_L^{^{14}N}/\sigma_L^D$ and $\sigma_T^{^{14}N}/\sigma_T^D$, respectively.

In the absence of explicit calculations, it may be speculated that our result demonstrates the existence of quark-gluon correlations, which are enhanced in a nuclear medium. A description of the data should encompass both, the enhancement of the longitudinal component σ_L and the reduction of the transverse component σ_T.

Finally, it is interesting to note that the strong nuclear dependence of the cross section ratio at low x and low Q^2, which resulted in the conclusion that $R = \sigma_L/\sigma_T$ is enhanced in the nuclear environment, is already suggested by measurements of σ_A/σ_D carried out at DESY [24], Daresbury [25], Cornell [26], SLAC [27] and FNAL [28] in the seventies, and early eighties. The results on the cross section ratio as a function of x from some of these experiments are shown in figure 5.21 together with the results from HERMES, SLAC and NMC as presented already in figure 5.2. The DESY data on ^{27}Al (open stars) and the FNAL data on ^{12}C (open triangles) show at low x ($Q^2 \approx 0.1 - 0.4$ GeV^2), a lower cross section ratio than the E665 and NMC data ($Q^2 > 1$ GeV^2).

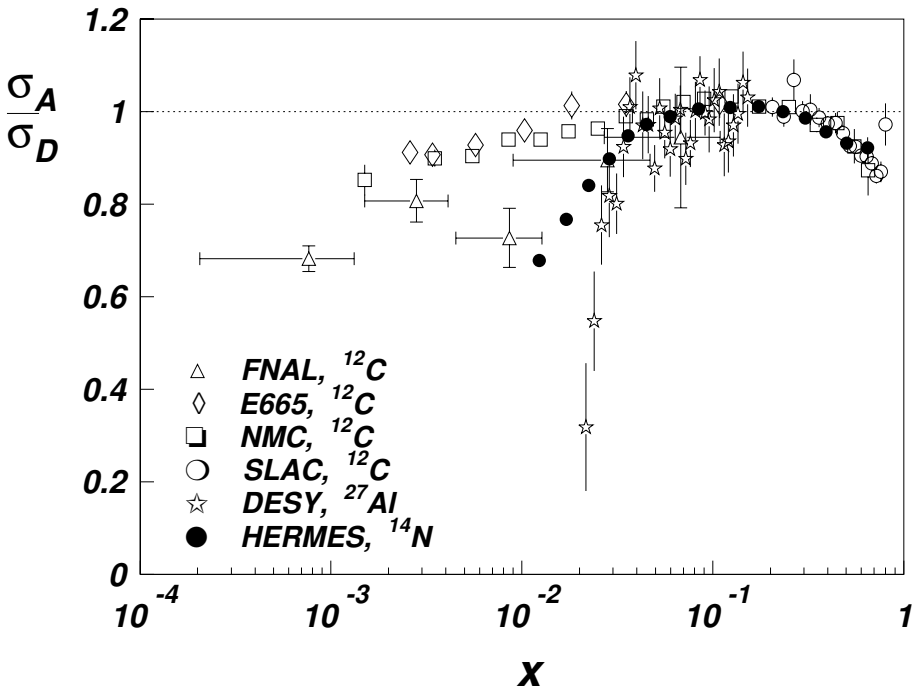

Figure 5.21: Ratio of the cross sections per nucleon as a function of x. The HERMES data on ^{14}N are represented as solid circles, the DESY data on ^{27}Al as open stars. Also shown are the data on ^{12}C obtained by FNAL (open triangles), SLAC (open circles), NMC (open squares) and E665 (open diamonds).

Chapter 6

Hadron Attenuation in ^{14}N

6.1 Introduction

In deep inelastic scattering the lepton-quark interaction leads to the break-up of the target nucleon. New hadrons are formed when the struck quark recombines with other quarks (mostly from the vacuum) to form colorless particles [1].

The process of hadron formation cannot be calculated from first principles in QCD. However, experimental data can be used to investigate this process in more detail. In this chapter the results are presented of measurements in which the fragmentation process is embedded in the nuclear medium. The hadrons are observed in coincidence with the scattered lepton. The quantity studied in such an experiment is the attenuation ratio R_{att} which represents the number of hadrons observed per DIS event for a target with atomic mass A, divided by the same number for a deuterium target. Due to interactions of the struck quark and/or final hadron with the nuclear medium the attenuation ratio is expected to be smaller than unity. For hadrons with a small energy fraction z of the virtual photon energy, however, the ratio can be larger than unity due to rescattering processes. Generally, it is assumed that for $z > 0.2$ such rescattering contributions can be neglected. However, the value of this limit is not known exactly.

The attenuation of the formed hadron depends on the interaction cross

[1] Apart from hadron formation originating from the struck quark (current fragmentation) hadrons can originate from the recoiling quarks not struck in the DIS scattering process (target fragmentation).

sections of the quark (σ_s) and the final (σ_h) hadron with the nuclear medium, as well as on the formation time (τ_f) of the hadron. The formation time is defined as the time between the initial hard interaction and the moment at which the final hadron appears. Since the cross section σ_h is known from total cross section experiments, it may be possible to use data on the hadron attenuation ratio to derive information on both σ_s and τ_f.

In the past, measurements of the attenuation ratio for hadrons were performed at SLAC [35] and CERN [7, 76]. The CERN (EMC [7]) results for R_{att} on Cu cover the energy transfer domain (ν) up to 200 GeV and are close to unity for $\nu > 15$ GeV. The WA21/59 results [76] on Ne cover the energy range between 5 and 40 GeV, and are consistent with the EMC results. At SLAC the attenuation ratio was determined for Be, C, Cu, and Sn targets at an average ν value of 10 GeV. In this case the attenuation ratio is significantly less than unity and increases with the atomic number of the target.

The CERN and SLAC data were compared in ref. [7] to the models of Bialas, Pavel, Chimay and Gyulassy (described in section 2.2.2). The authors concluded that the two-time scale model describes the data better than the one-time scale model. However, due to the limited amount of data at low energy, no explicit fit of the quantities σ_s and τ_f could be performed.

The data on R_{att} collected by HERMES are of substantially better quality than the previous results. The statistics allow fine binning (see [6]) and the effect on R_{att} is expected to be largest in the HERMES kinematic domain.

In this chapter the extraction of R_{att} from HERMES data on ^{14}N is described in detail (section 6.2). Furthermore, the results on R_{att} are compared to the same one-time and two-time scale models used in ref. [7] for interpretation of the previous data. The objective is to attempt a determination of the hadron formation time (section 6.3), and to compare the data on R_{att} to recent calculations based on the gluon bremsstrahlung model described in section 2.2.2. The chapter is concluded in section 6.4.

6.2 Determination of R_{att}

Deep-inelastic scattering (DIS) events on ^{14}N and ^{2}H are used to determine R_{att} as a function of ν, z, Q^2, and p_t. The data analysis is discussed below in various subsections. The results for R_{att} are presented in the last subsection.

6.2.1 Event selection

The criteria for the selection of DIS events are the same as those used for the inclusive analysis presented in section 5.2.1. Additional constraints are imposed to ensure that the hadron information in the event is of good quality. These constraints are discussed in section 6.2.2. For an unambiguous interpretation of the data and comparison with models it is important to exclude data in the region $Q^2 < 1$ GeV^2 where the nuclear effects on the inclusive cross section described in chapter 5 are most prominent. Therefore, Q^2 is constrained to $Q^2 > 1$ GeV^2.

6.2.2 Hadron and Pion identification

Hadrons are selected by the requirement that PID3+PID5 < 0 (see section 3.4.2). The pions contained in this sample can be selected by making use of the Čerenkov detector, as explained in subsection 3.4.2. In the hadron energy range $4 < E_h < 13.5$ GeV the pions give a signal in the threshold Čerenkov detector, while more massive and thus slower hadrons do not give a sizable signal. For a pion a signal of at least 0.25 photoelectrons is required.

In table 6.1 the total number of DIS events [2], the number of hadrons, and the number of identified pions are listed. Requirements on data quality and kinematics are included. The hadron sample contains the pions as well.

Table 6.1: Remaining number of DIS events, hadrons (including pions), and pions after application of the data quality cuts described in the text.

	^{2}D	^{14}N
DIS	2.12×10^6	1.85×10^6
Hadrons	0.991×10^6	0.814×10^6
pions	0.316×10^6	0.251×10^6

[2] The number of DIS events presented in this table is smaller than the number presented in chapter 5 due to the constraint on Q^2 ($Q^2 > 1$ GeV^2).

6.2.3 Acceptance

As the attenuation is obtained from a ratio of DIS yields, the results should not depend on the spectrometer acceptance. This was verified by plotting the ratio of hadrons in nitrogen and deuterium, $R_{N/D}$, versus the azimuthal angle Φ and the polar angle Θ. The angular distributions are shown for hadrons and pions, separately, both as a function of Φ and Θ, in figures 6.1 and 6.2.

The ratio $R_{N/D}$ as a function of Θ (fig. 6.1) shows no dependence on the spatial acceptance for hadrons, but does so for pions for $\Theta > 0.19$ rad. Since only pions are affected, this effect is possibly related to the response of the Čerenkov detector at large pion emission angles and high target density (as used for the ^{14}N data). To avoid this only pions in the Θ-range between 0.04 and 0.19 rad are used.

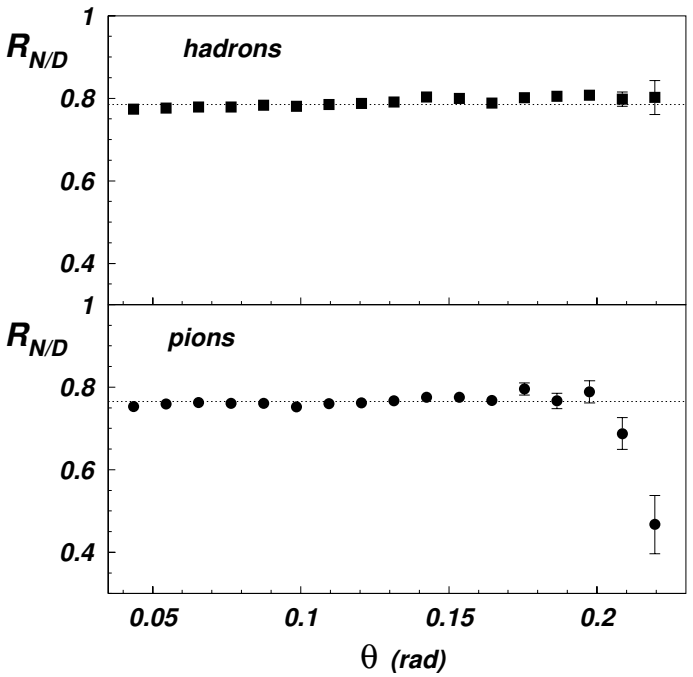

Figure 6.1: Ratio of hadrons (upper panel) and pions (lower panel) in nitrogen and deuterium as a function of the polar angle (Θ).

From figure 6.2 it is seen that there is no significant dependence of the

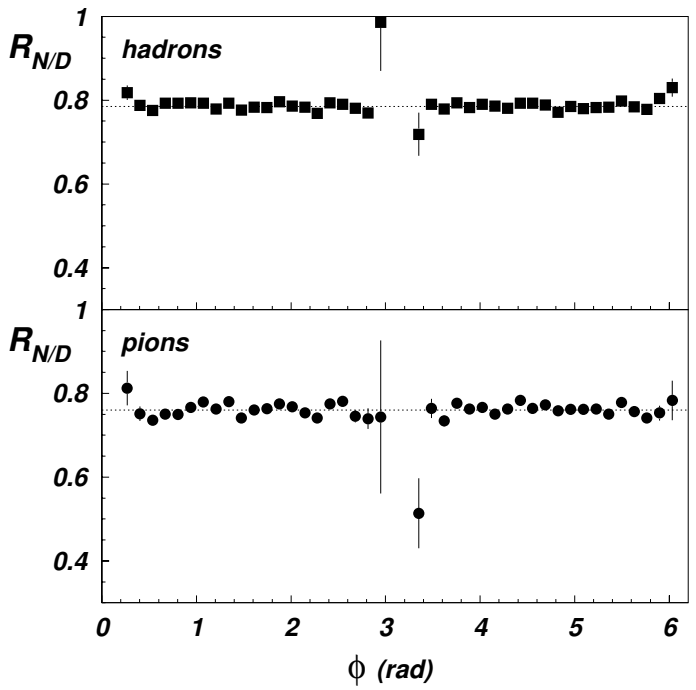

Figure 6.2: Ratio of hadrons (upper panel) and pions (lower panel) in nitrogen and deuterium as a function of the azimuthal angle (Φ).

ratio $R_{N/D}$ on the azimuthal angle Φ, except for some edge effects near $\Phi = \pi$ rad.

6.2.4 Kinematic distributions

The kinematic variables ν, Q^2 and x are related, as is evident from Eq. (2.5). The correlation between ν and Q^2 is shown in figure 6.3. It can be seen that the W, y and Θ boundaries imposed by the analysis or the experiment, limit the ν and Q^2 range that can be used for the determination of R_{att}. For our purposes it is most important to note that the low ν data correspond to a smaller Q^2 range then the high ν data.

Also the hadronic kinematic variables ν, z and E_h are related, as reflected by Eq. (2.7). The energy (E_h) of identified pions ranges between 4 and 13.5 GeV, while for hadrons the energy is always larger than 1.4 GeV (see chapter 3). Hence, two correlation plots have to be made. The correlation

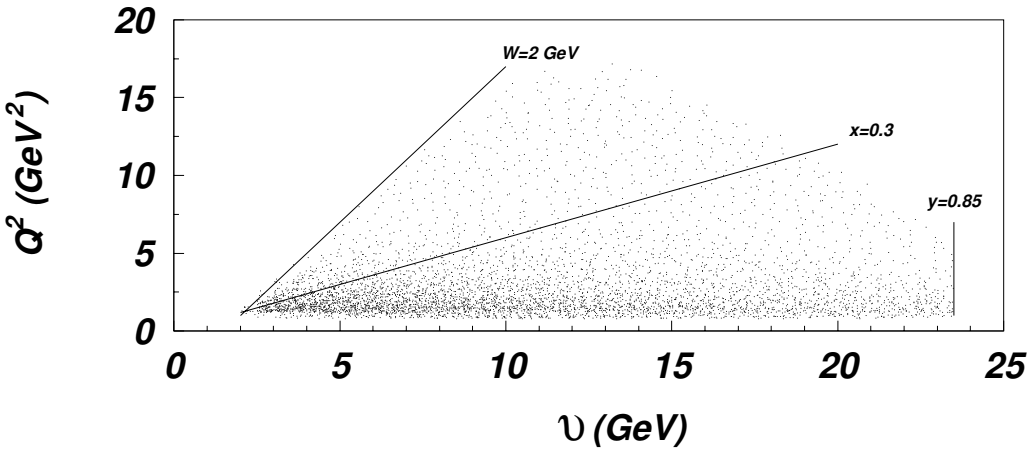

Figure 6.3: Kinematic distribution of DIS events as a function of ν and Q^2. The angular acceptance of the spectrometer ($\Theta < 0.22$ rad) results in the upper boundary for Q^2 as a function of ν. The boundary at the right hand side is caused by the requirement $y < 0.85$. The lower boundary corresponds to $Q^2 = 1$ GeV^2, while the left boundary is the result of excluding the resonance region, $W > 2$ GeV.

between ν and z is shown in figure 6.4 for hadrons and pions separately. From this figure it can be seen that a z-cut of 0.2 (0.5) for hadrons (pions) is only effective above a certain ν value. Quantitatively, a z-cut of 0.2 (0.5) for hadrons (pions) needs the requirement $\nu > 7$ GeV ($\nu > 8$ GeV). At lower values of ν the z-cut is not effective because all values of z are higher anyhow. The $\nu - z$ correlation is important when comparing the R_{att} data to models that assume a certain z or ν-dependence.

6.2.5 Radiative corrections

The ratio of hadrons produced on ^{14}N and ^{2}H is normalized to the ratio of DIS events (in the same kinematic domain) to obtain the attenuation ratio (section 2.2.2). In this way the attenuation ratio is corrected for the A-dependence of the inclusive ratio. Hence, the attenuation ratio only reflects the A-dependence of the hadronization process, which is presumably of different origin than the A-dependence of the inclusive ratio, discussed in chapter 5.

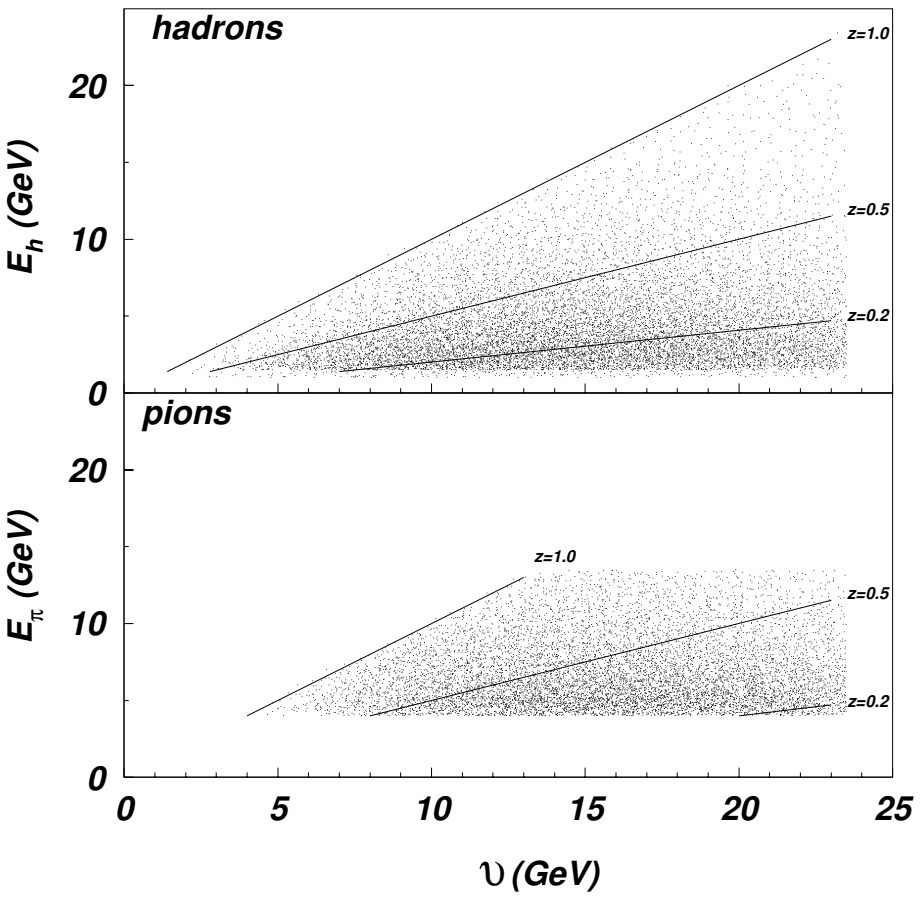

Figure 6.4: Kinematic distribution of hadrons and pions as a function of ν and z.

Through the normalization on the number of DIS events the radiative corrections of the inclusive cross sections enter in the evaluation of the attenuation ratio. As the evaluation of the radiative corrections has been extensively discussed in section 5.2.4, here only the size of the corrections and the uncertainties are given. Table 6.2 lists the radiative corrections for the attenuation ratios. They are composed of the inclusive (rc) and semi-inclusive (sirc) corrections. The inclusive corrections enter the attenuation ratio through the normalization by the number of DIS events, while the semi-inclusive corrections apply to the eA→ehX cross sections. The inclusive corrections are much smaller than those discussed in chapter 5 due to the averaging over

a large Q^2 range and the requirement that $Q^2 > 1$ GeV^2. At high ν the corrections (sirc) which are applied to the semi-inclusive events (in which the hadrons are produced) are much smaller than the inclusive corrections, since the contributions due to elastic and quasi-elastic scattering become very small.

The consistency of the results on the attenuation ratio and the results on the inclusive cross section ratio, as presented in chapter 5, has been investigated. The radiatively corrected inclusive cross section ratio has been compared with the inclusive cross section ratio without applying radiative corrections but including the requirement that for each event at least one hadron is detected. These cross section ratios should be equal since the dominant elastic and quasi-elastic contributions to the radiative corrections hardly contribute to the "tagged" events (i.e. those with at least one hadron) and the remaining radiative corrections are very small. However, since hadrons are attenuated in ^{14}N, the tagged inclusive cross section ratio must be corrected as well. This correction can be carried out by making use of the attenuation ratio, and weigh each tagged event by $1/R_{att}$ if only one hadron was found in the event. If more than one hadron is detected the weight should be equal to unity since the event passes the hadron constraint also with hadron attenuation. It is found that the radiative corrected inclusive cross section ratio and the tagged inclusive cross section ratio agree to within 2%. For more details on the comparison see reference [71]. It is concluded that the inclusive and semi-inclusive results are consistent.

6.2.6 Diffractive ρ^0 production

A small fraction of the detected pions originates from the decay of diffractively produced ρ^0 vector mesons [3]. As the effect of the nuclear medium on diffractive ρ^0 production is related to the hadronic structure of the virtual photon rather than the hadron formation process itself, the pions from diffractively produced ρ^0 mesons should be subtracted from the hadron sample originating from DIS fragmentation processes in the present analysis. The uncertainty arising from the contribution of diffractive ρ^0 mesons can be estimated and included in the systematic error of the hadron attenuation results.

[3] It is noted that part of the detected pions may also originate from ρ^0 mesons that are produced in the fragmentation process. In the present analysis these pions cannot be distinguished from fragmentation pions.

Table 6.2: The inclusive (rc) and semi-inclusive (sirc) radiative corrections of the attenuation ratio. Also shown are the systematic uncertainty in the radiative corrections (Δ rc), the uncertainty due to diffractive ρ^0 production ($\Delta\rho$), and the reproducibility error (Δ rep). The total systematic error which represents the quadratic sum of all three contributions (Δ tot) is given as well. A negative sign means that the correction decreases R_{att}.

ν GeV	rc %	sirc %	Δ rc %	$\Delta\rho$ %	Δ rep %	Δ tot %
5.205	-0.66	0.88	0.40	1.0	1.5	1.8
7.112	-0.53	0.75	0.40	0.9	1.5	1.8
9.065	-0.32	0.47	0.40	0.8	1.5	1.7
11.03	-0.29	0.54	0.40	0.7	1.5	1.7
13.01	-0.14	0.55	0.40	0.6	1.5	1.7
15.00	-0.19	0.60	0.40	0.5	1.5	1.6
16.99	0.82	0.71	0.40	0.4	1.5	1.6
18.98	2.46	0.41	0.60	0.3	1.5	1.6
20.96	5.21	0.15	0.90	0.2	1.5	1.8
22.69	10.7	-0.96	1.00	0.1	1.5	1.8

The fraction of positive and negative pions that originate from diffractive ρ^0 mesons has been estimated by identifying the diffractive ρ^0 mesons from DIS-events that contain one positive and one negative pion. Next, the HERMES Monte Carlo (HMC) is used to determine the ratio of ρ^0 mesons of which only one pion enters the acceptance of the HERMES spectrometer to those of which both decay products are observed. The total ρ^0 meson contribution to the pion multiplicity was estimated by combining the two results. The ρ^0-meson contribution depends on the kinematics and is estimated to range from 0.2 to 5% (largest at $z = 0.65$).

The contribution of these ρ^0 decay pions to the nuclear attenuation has also been estimated. The attenuation of ρ^0 production in nuclei is represented by the nuclear transparency (T_A), which is defined as

$$T_A = \frac{\sigma_A}{A \cdot \sigma_H}, \tag{6.1}$$

where σ_A represents the cross section for ρ^0 production when using a target with atomic mass A. Due to initial and final state interactions between the hadronic components of the virtual photon and the nucleus this ratio is smaller than unity.

For exclusive ρ^0 production the nuclear transparency has been measured at HERMES [72]. The nuclear transparency was found the be a function of the coherence length ($l_{coh} = 2\nu/(Q^2 + M_\rho^2)$), and ranges (for A=14) from 0.45 to 0.68 at l_{coh} values of about 6.0 and 1.0 fm, respectively. The transparency for ^{2}H (T_2) equals 0.969 ± 0.045, almost independent of l_{coh}.

The observed ratio of DIS pions from ^{14}N and ^{2}H, i.e. N_{14}/N_2 (R_{att}^{obs}) will thus be contaminated by a ρ^0 contribution:

$$R_{att}^{obs} = \frac{N_{14}}{N_2} = \frac{R_{att} N_2^{dis} + T_{14} T_2^{-1} N_2^{\rho}}{N_2^{dis} + N_2^{\rho}} \tag{6.2}$$

with N_2^ρ the number of pions from diffractive ρ^0 mesons production on ^{2}H. From Eq. (6.2) it follows that the difference between the desired quantity R_{att} and the observed quantity R_{att}^{obs} is given by

$$R_{att} - R_{att}^{obs} = \frac{N_2^{\rho^0}}{N_2^{dis}} \left(\frac{N_{14}}{N_2} - T_{14} T_2^{-1} \right). \tag{6.3}$$

With $\frac{N_{14}}{N_2} \approx 0.9$, $\frac{N_2^{\rho^0}}{N_2^{dis}}$=5%, and $T_{14}/T_2 > 0.47$ it follows that $R_{att} - R_{att}^{obs}$ is always smaller than 2%. The maximum values for the difference $R_{att} - R_{att}^{obs}$ are determined as a function of z and ν. Half of the difference between R_{att} and R_{att}^{obs} is applied as a correction to the data, while the uncertainty is taken to be half of this difference. The uncertainties are presented in the 3^{rd} column of table 6.3 and the 5^{th} column of table 6.2 as a function of z and ν, respectively.

6.2.7 Systematic uncertainties

Since the results are presented as a ratio, most errors cancel. It has to be realized that R_{att} represents a super ratio, i.e. the ratio of hadrons per DIS event on two nuclei. As a result possible rate fluctuations, efficiency changes, etc., largely cancel. The attenuation ratio was determined for three

Table 6.3: The systematic uncertainty in the attenuation ratio as a function of z originating from diffractive ρ^0 production ($\Delta\rho$), the radiative corrections (Δ rc), and the reproducibility error (Δ rep). The total systematic error, is the quadratic sum of the three contributions (Δ tot), which is also shown.

z	Δ rc %	$\Delta\rho$ %	Δ rep %	Δ tot %
0.26	0.5	0.1	1.5	1.6
0.35	0.5	0.3	1.5	1.6
0.45	0.5	0.6	1.5	1.7
0.55	0.5	0.6	1.5	1.7
0.65	0.5	1.0	1.5	1.9
0.75	0.5	0.8	1.5	1.8
0.85	0.5	0.2	1.5	1.6
0.94	0.5	0.1	1.5	1.6

different data taking periods [73] and deviations smaller than 1.5 % were found, reflecting the uncertainty due to the reproducibility.

The systematic errors thus originate from the inclusive radiative corrections, the diffractive ρ^0 contribution, and the reproducibility. The total systematic error equals the quadratic sum of the three contributions, and is presented in table 6.2 as a function of ν and in table 6.3 as a function of z.

6.2.8 Results

The attenuation ratio for hadrons and pions as a function of ν are shown in figure 6.5 for two different z cuts. The average z values are shown for each ν-bin in the figure. The upper panel represents all the data, while the lower panel shows only data with $z > 0.5$. As was already mentioned in section 6.2.4 the cut $z > 0.5$ for pions is only effective for ν values larger than 8 GeV, as can be seen from the average z values that are well above 0.5 for the lowest ν bins.

Possible differences between hadron and pion attenuation can only be determined from the lower panel for $\nu > 8$ GeV, since here both data sets have similar average z values for every ν bin (section 6.2.4). From the lower

panel of figure 6.5 it is concluded that for $z > 0.5$ and $\nu > 8$ GeV there is no significant difference between hadrons and pions. This is expected since the hadron data sample contains mainly pions.

At low ν values the attenuation ratio is smaller than unity, showing that the hadron formation process is affected by the nuclear environment. It is seen that the ratio increases with increasing ν to values slightly above unity. An increase with ν is expected since at high values of ν the hadron formation is taking place largely outside the target nucleus. For the upper panel the data are significantly above unity in the highest ν-bin. This may be caused by a shift of high z hadrons to lower z hadrons in ^{14}N due to the interactions with the nuclear environment, leading to a depletion of the high z-region and an excess at low z. This is supported by the fact that for the bottom panel of figure 6.5, where $z > 0.5$, the excess is statistically less significant.

The error band in the figure represents the systematic uncertainty in % from unity. Since the diffractive ρ^0 contribution peaks at higher z values ($z = 0.65$), as shown in table 6.3, the systematic error for the lower panel is larger than for the upper panel.

Figure 6.6 shows the attenuation of pions and hadrons as a function of z. Only the z, ν-region is shown where the two kinematic variables are not coupled due to the hadron or pion energy cut, as was explained in section 6.2.4. Again it is concluded that there is no significant difference between hadrons and pions. At $z > 0.8$, a strong decrease of the attenuation ratio is observed. This decrease suggests that the probability for a leading hadron (or quark) to traverse a large nucleus like ^{14}N without loosing a significant amount of energy is very small. The origin of the decrease of the attenuation ratio around $z = 0.65$ is not clear, although it is not excluded that it represents a statistical fluctuation.

The data presented thus far represent the sum of positive and negative hadrons, since the models for hadron attenuation do not differentiate between the two. However, it is important to see if a difference does exists, as this may be an indication that hadrons of different types have different formation times. The attenuation ratios for positive and negative pions and for positive and negative hadrons are shown as a function of ν in figure 6.7. The upper panel shows h^+ and h^-, while the lower panel shows π^+ and π^-. For pions no significant difference is observed, while for hadrons there is a significant difference. At low ν positive hadrons are less attenuated than negative hadrons, i.e. the positive hadrons are less influenced by the nuclear environment. Monte Carlo studies show that for positive hadrons the contribution

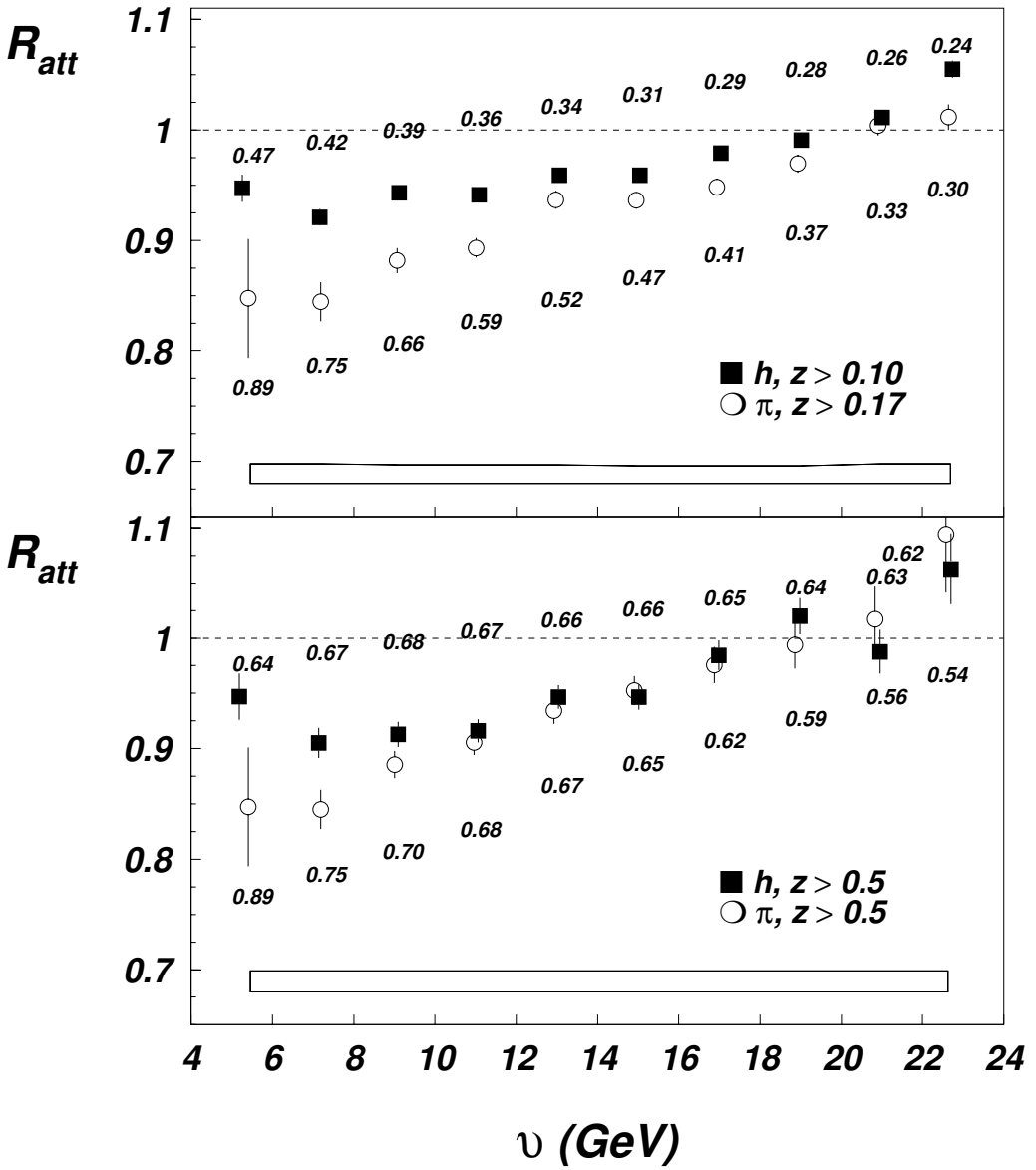

Figure 6.5: Attenuation of hadrons and pions as a function of ν. The upper panel shows all the data, while the lower panel represents the data with $z > 0.5$. The error band represents the quadratic sum of the uncertainty in the radiative corrections, the reproducibility uncertainty, and the uncertainty due to the diffractive ρ^0 meson contribution. The average z values of the data points are printed above data for hadrons and below the data for pions.

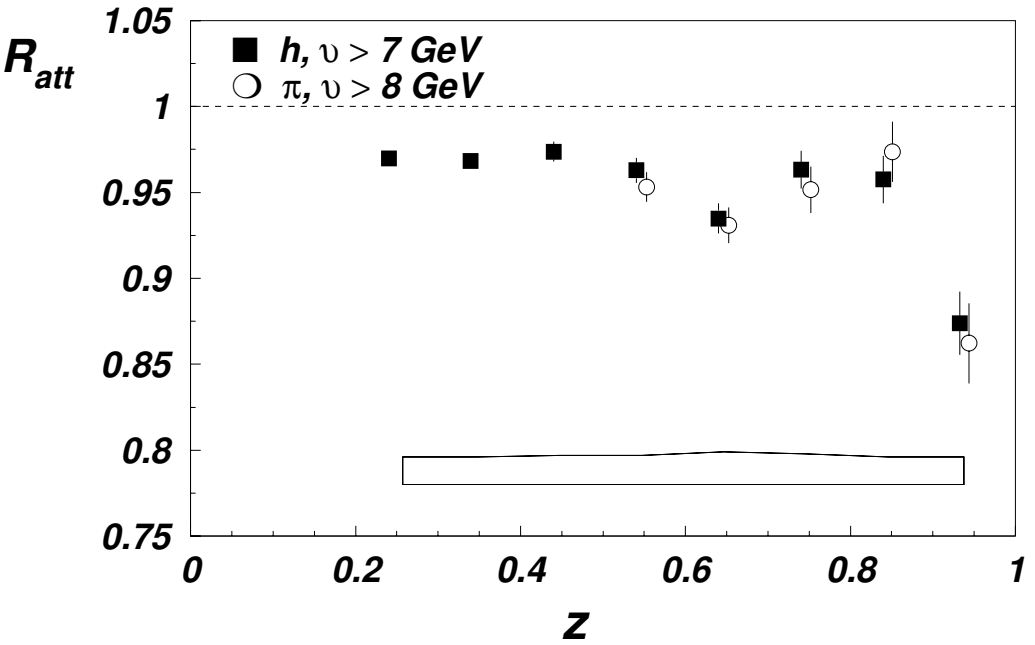

Figure 6.6: Attenuation of hadrons and pions as a function of z. The error band represents the quadratic sum of the uncertainty in the radiative corrections, the reproducibility uncertainty, and the uncertainty due to the diffractive ρ^0 meson contribution.

of protons to the data sample ($\approx$ 17%) is larger than the contribution of anti-protons to the negative hadron sample ($\approx$ 7%). The kaon contributions to the positive and negative hadron samples are less different, i.e. 18% and 12%, respectively. Therefore, a possible qualitative explanation of the larger attenuation ratio for positive hadrons is a longer formation time for protons than for mesons and/or the smaller hadron-nucleon cross section for positive hadrons (see table 6.4). In the next section an attempt is made to estimate the difference of the formation times of positive and negative hadrons using the one-time scale model.

Finally, the attenuation ratios as a function of Q^2 and p_t are presented. In figure 6.8 the attenuation is shown as a function of Q^2 for hadrons and pions with $z > 0.5$ and $\nu > 8$ GeV. At low values of Q^2 the attenuation ratio decreases with Q^2. In the gluon bremsstrahlung model the decrease of R_{att} with Q^2 is related to the proportionality of the quark energy loss with Q^2 (see section 2.2.2), and thus to a decrease of the formation length with Q^2.

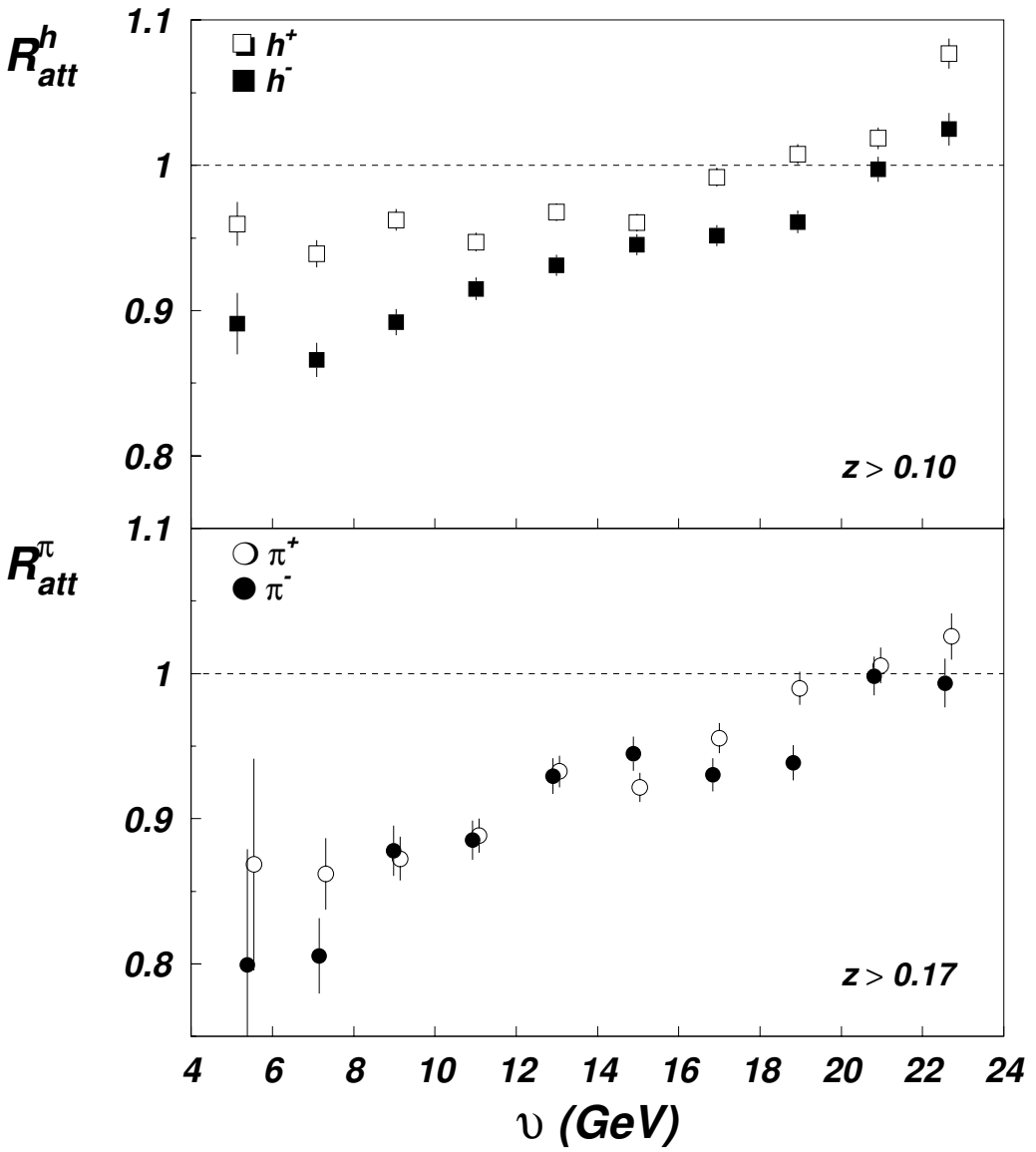

Figure 6.7: Attenuation of positive and negative hadrons (upper panel) and positive and negative pions (lower panel) as a function of ν. The errors bars represent the statistical uncertainty only. The systematic uncertainty is shown in figure 6.5.

At higher values of Q^2 the attenuation ratio is roughly constant and another process may have taken over [4].

In figure 6.9 the attenuation is shown as a function of p_t for hadrons and pions with $z > 0.5$ and $\nu > 8$ GeV. For $p_t > 0.6$ GeV, the attenuation ratio shows a systematic rise, resulting in values larger than unity, while for p_t values between 0.4 and 1 GeV the ratio is smaller than unity. The rise of R_{att} with p_t may be the result of a broadening of the p_t distribution due to additional rescattering processes of the propagating partons and/or hadrons in ^{14}N compared to ^{2}H. For $0.3 < p_t < 0.6$ GeV the attenuation ratio decreases with increasing p_t. For this behavior no explanation is available.

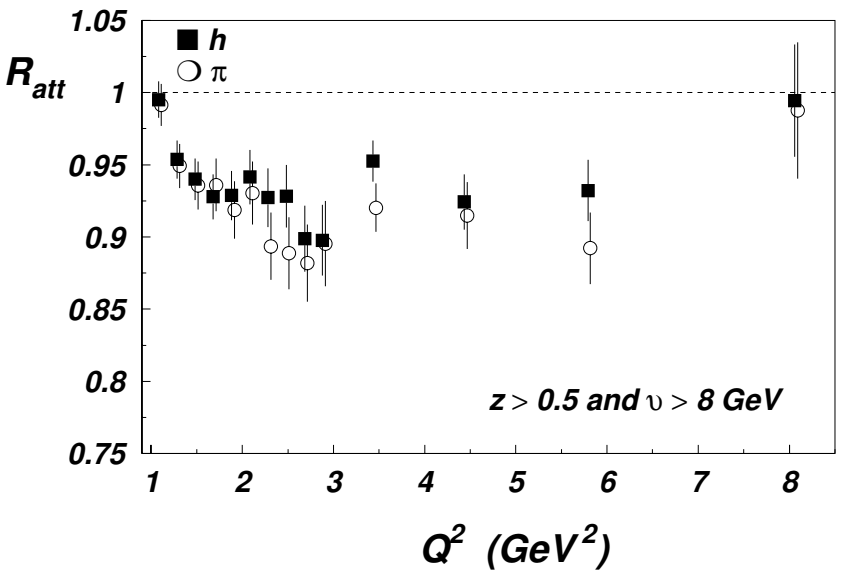

Figure 6.8: Attenuation of hadrons and pions as a function of Q^2. The error bars represent the statistical uncertainty only. The systematic error is about 2%.

[4] A rise with Q^2 could be related to the formation of a point like configuration [74], which has a reduced interaction cross section.

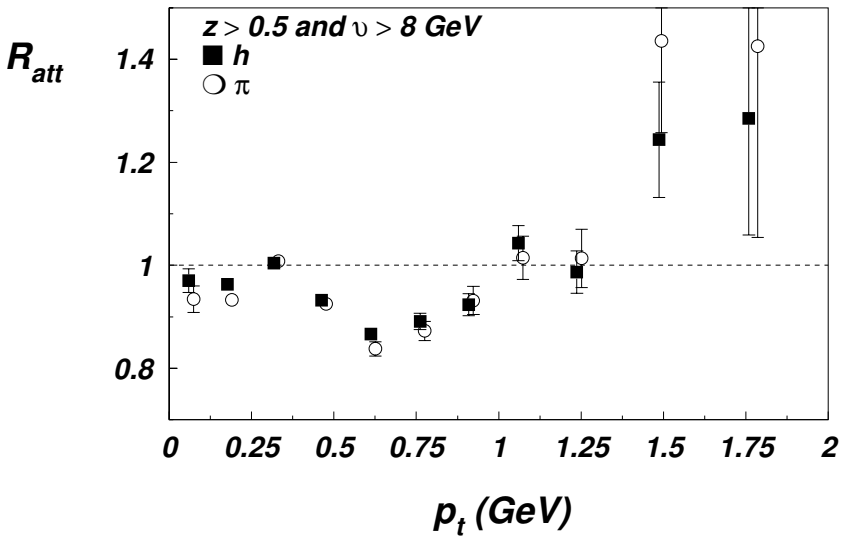

Figure 6.9: Attenuation of hadrons and pions as a function of p_t. The error bars represent the statistical uncertainty. The systematic error is about 2%.

6.3 Models for the attenuation ratio

In this section the pion and hadron attenuation data are discussed in relation to the models described in subsection 2.2.2. First the one-time scale and two-time scale models are compared with the experimental data. In the comparison, the data samples of positive and negative pions are added together as no differences between the two corresponding attenuation ratios have been observed, while positive and negative hadrons are treated separately. Using these models formation times are determined for pions, positive hadrons, and negative hadrons, separately. Finally, the gluon bremsstrahlung model is compared to the data.

6.3.1 One-time and two-time scale models

The ν-dependence of the attenuation ratio is compared with the models which are described in detail in section 2.2.2. In this framework only the ν-dependence can be studied since no Q^2 or p_t-dependence of R_{att} is foreseen in the one-time or two-time scale model. This does not preclude the application of the two models since the experimental data do not show significant Q^2 and p_t-dependences. It has to be realized from the start, however, that

the R_{att} data themselves already contain more information than contained in the one-time and two-time scale models. The strong z-dependence at high z, for instance, is in contradiction with the expressions used for the formation time in the one-time and two-time scale models, but the statistical weight of the data at these high z values ($z > 0.85$) is limited and the high z data are distributed over all the ν bins. For that reason, and in order to be consistent with previous analyses of this kind, the formation time models have still been used for (part of) the interpretation of the data.

In a discussion of models describing hadron attenuation it is important to also consider the data published by EMC, SLAC and WA21/59 [76]. The world data on the attenuation ratio R_{att} for Cu and ^{14}N are shown in the upper and lower panel of figure 6.10, respectively. It is seen from the upper panel that the EMC results on Cu (open squares) rise with increasing values of ν. The SLAC result on ^{14}N in the lower panel is an interpolation of the SLAC results on Be, C, Cu and Sn, and is about two standard deviations below the HERMES results [5]. However, the SLAC error bar only represents the statistical uncertainty and the SLAC ν-bin extends from 4 to 20 GeV. Hence, the data are not necessarily inconsistent. The WA21/59 data on neon (open circles) are evolved to ^{14}N using the A-dependence of R_{att} as parametrized by SLAC [35], resulting in an increase of about 4%. These data are in fair agreement with the HERMES data, with a possible exception at the highest ν values covered by HERMES. The disagreement at these high ν values may be related to the low average z values of the HERMES data in this domain, as was discussed already in relation to figure 6.5.

The curves in figure 6.10 represent the predictions from the one-time and two-time scale models. In this figure, the parameters of the models were taken from the publication of the EMC experiment [7]. A cross section of the final hadron with the nuclear environment (σ_h) of 20 mb is used for all the curves, while the unknown cross section of the color string (σ_s) and color field (σ^*) are varied (but not fitted). For the normalized nuclear density the

[5] Although the systematic and statistical uncertainties should be considered separately, the error on the HERMES data does reflect the quadratic sum of the statistical and systematic uncertainty. This choice was made since it reduces the number of fits that have to be performed to estimate the systematic error on the fit parameters when using phenomenological models to describe the data. Considering the large uncertainty in the fit parameters arising from model dependences, this choice does not affect the uncertainty of the parameters significantly.

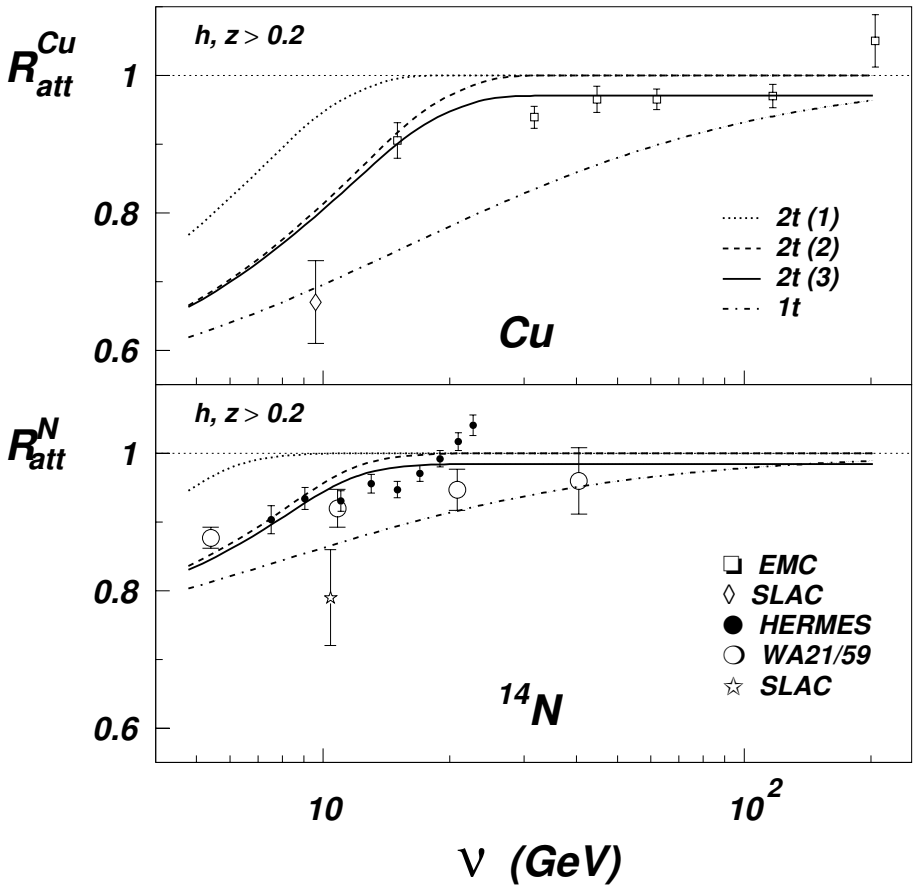

Figure 6.10: The world data on Cu (upper panel) and ^{14}N (lower panel) together with model predictions. The open squares represent the EMC results, the open diamond and star the SLAC results and the open circles the WA21/59 results. The WA21/59 data on neon (and the SLAC data collected on several nuclei) are evolved to ^{14}N, using the A-dependence as parametrized by SLAC [35]. The error bars represent the statistical uncertainty only. The HERMES results are shown as solid circles. The error bars on the HERMES data reflect the quadratic sum of the statistical and systematic uncertainty. The curves are explained in the text.

Saxon-Woods expression [32], i.e.

$$\rho_A = \rho^0/(1 + e^{(r-r_A)/a})$$

with $r_A = (0.978 + 0.0206A^{1/3})A^{1/3}$ fm and $a = 0.54$ fm, is used.
In the two-time scale model expressions for l_c and l_f were derived from the string model [33, 75], i.e. $l_f = z(1-ln(z))\nu/\kappa$ and $l_c = l_f - z\nu/\kappa$. The relation between l_c and l_f is explained in subsection 2.2.2, while the expression for l_f, proposed by T. Chmaj [75], was used by EMC for the calculations with the two-time scale model. Here, the quoted expression for l_f is only used to verify the calculations performed by EMC, and to assess the quality of the models in relation to the new data. In the second half of this section τ_f will be treated as free parameter.

The dotted curves '2t(1)' represent the two-time scale model with σ_s as well as σ^* equal to zero. For the dashed curves '2t(2)' $\sigma_s = 20$ mb and $\sigma^* = 0$ mb, while for the solid curves '2t(3)' also σ^* is larger than zero, namely $\sigma^* = 0.75$ mb. The value for κ is fixed at 1 GeV/fm.

It is concluded that for Cu the solid curve, i.e. a two-time scale model with $\sigma_h = \sigma_s = 20$ mb and $\sigma^* = 0.75$ mb, provides a good description of the data. Using the same parameters for ^{14}N and only adjusting the nuclear density to that of ^{14}N does not give a very good description of the ^{14}N data. However, the discrepancy between the ^{14}N data and the two-time scale model is only significant at high ν. This discrepancy may be caused by the larger contribution of low z hadrons at high ν, leading to an enhancement of R_{att} due to rescattering, as discussed before. No hadron enhancement mechanism is included in the one and two-time scale models. Therefore, it is necessary to exclude the low z hadrons from the data sample when fitting the data. Since the HERMES kinematics (section 6.2.4) dictate a $z > 0.5$ cut to avoid z-ν correlations in the pion data sample, we will use this z-cut for the extraction of the formation time. It is interesting to note that the EMC data also show that $R_{att} > 1$ at the largest ν values. This may be an indication that a similar effect as described for the HERMES data is present in the EMC data.

It is noted that when $\sigma_h \approx \sigma_s$ the two-time scale model is effectively reduced to a one-time scale model (with $\tau_c = -ln(z)\nu/\kappa$ in Eq. (2.37)), which is not consistent with the one-time scale model represented by the dot-dashed curves ('1t') in figure 6.10. One of the reasons for this inconsistency is the fact that in the EMC publication for the one-time scale model it is assumed that $\tau_f = (\tau_h/m_h)\nu z$ with $\tau_h/m_h = 1$ (Eq. (2.33)), which differs significantly

from the expression for τ_c given above. In general the two-time scale models seem to give a better description of the data, but it should be noted that the constrained value of $\tau_h/m_h = 1$ causes the failure of the one-time scale model. If τ_f is used as a free parameter a much better description can be obtained. Hence, it is at this point not possible to discriminate between the one-time and two-time scale models. It is necessary to fit the data using both models, without assumptions on τ_f.

In the remainder of this section the one-time scale and two-time scale models are fitted to the ^{14}N data, in an attempt to derive values for the formation time τ_f. Positive and negative hadron data are fitted separately, such that possible differences in the fit parameters can be determined. As mentioned earlier only hadrons and pions with $z > 0.5$ are used. This removes most of the hadrons originating from rescattering processes, and also removes the ν-z correlation (section 6.2.4).

For the cross section of the final hadron with the nuclear environment, σ_h, the measured hadron-nucleon cross section is used in the fits. These cross sections are known from hadron-nucleon cross section measurements, and are listed in reference [77]. Using the LUND Monte Carlo program the different contributions from pions, protons and kaons to the positive and negative hadron sample have been estimated. The different contributions are listed, together with the individual hadron-nucleon cross sections in table 6.4. The h^+-nucleon and h^--nucleon cross sections (σ_h) are determined from the sum of the pion, kaon and (anti-) proton cross sections, multiplied by the corresponding fractions. The uncertainty ($\Delta\sigma_h$) in the hadron-nucleon cross sections stems from the uncertainty in the individual cross sections. Uncertainties in the Monte Carlo calculated fractions have not been considered.

In the upper panel of figure 6.11 the HERMES pion data are shown together with the fits from the one-time and two-time scale models. For σ_π the sum of the π^+ and π^- cross section is used, multiplied by the π^+ and π^- fractions in the pion data sample (giving 23$\pm$2 mb). The value for κ is fixed at 1 GeV/fm. The two-time scale model was used in three different manners. For the solid curve '2t(4)' the parameters were as in the previous figure, i.e. $\sigma_h = 20$ mb, $\sigma_s = 20$ mb and $\sigma^* = 0.75$ mb. The dotted curve '2t(5)' represents a fit of the data with σ_s and σ^* as free parameters. The results for these parameters are within their uncertainty equal to the parameters of the solid curve. Hence, the fit does not lead to a significant improvement of the description of the data. If l_c is used as a free parameter, as represented by

Table 6.4: The pion, proton and kaon contribution to the positive and negative hadron sample (obtained from Monte Carlo), together with the hadron-nucleon interaction cross sections σ_π, σ_p and σ_k. The $h^\pm$ cross section, i.e. the sum of the pion, kaon and proton cross sections multiplied by the corresponding fractions, and the uncertainties are given in the last two columns.

sample	hadrons and cross sections						σ_h	$\Delta\sigma_h$
	π	σ_π	p	σ_p	K	σ_K		
	%	mb	%	mb	%	mb	mb	mb
h^+	64	22	17	40	18	17	24	2
h^-	81	25	7	60	12	23	27	2

the dashed curve '2t(6)', the fit is equally poor. The two-time scale model does not give a good description of the data, as all fits have a χ^2 per degree of freedom (χ^2/ndf) which is larger than 5.

The dot-dashed curve in figure 6.11 represents a fit using the one-time scale model with two free parameters, i.e. τ_h/m_h in the expression for τ_f ($\tau_f = \nu z \tau_h/m_h$), and σ_s. Since the average z for all the data is about the same (≈ 0.65) no improvement is obtained when the alternative expression for τ_f is used, i.e. $\tau_f = \nu\tau_q/m_q$, with τ_q/m_q as free parameter. In either case the one-time scale model gives a reasonable description of the data at low ν, but is below the data at high ν.

The lower panel of figure 6.11 shows the dependence of the two-time scale fit on the value of κ and σ_h. The effect of both variations is mostly seen at low ν values. The variations of κ and σ_h lead to variations in the fit parameters, which contribute to the uncertainty in these parameters. The fit results for the one-time scale model and the two-time scale model where l_c is a free parameter, are listed in tables 6.5 and 6.6, respectively. The χ^2/ndf value is smallest for the fits with the one-time scale model. The data are not very well described by the two-time scale model, showing that the used relation between l_c and l_f, i.e. $l_c = l_f - z\nu/\kappa$, is not sufficient (if $\sigma_s = \sigma_h$) or not suitable (if $\sigma_s \approx 0$ and $\sigma_h \approx 20$ mb) to describe the ν-dependence of the data. Varying the value of κ does not improve the fits.

The positive and negative hadron data are fitted also with the one and two-time scale model. The resulting fit parameters are also given in tables 6.5

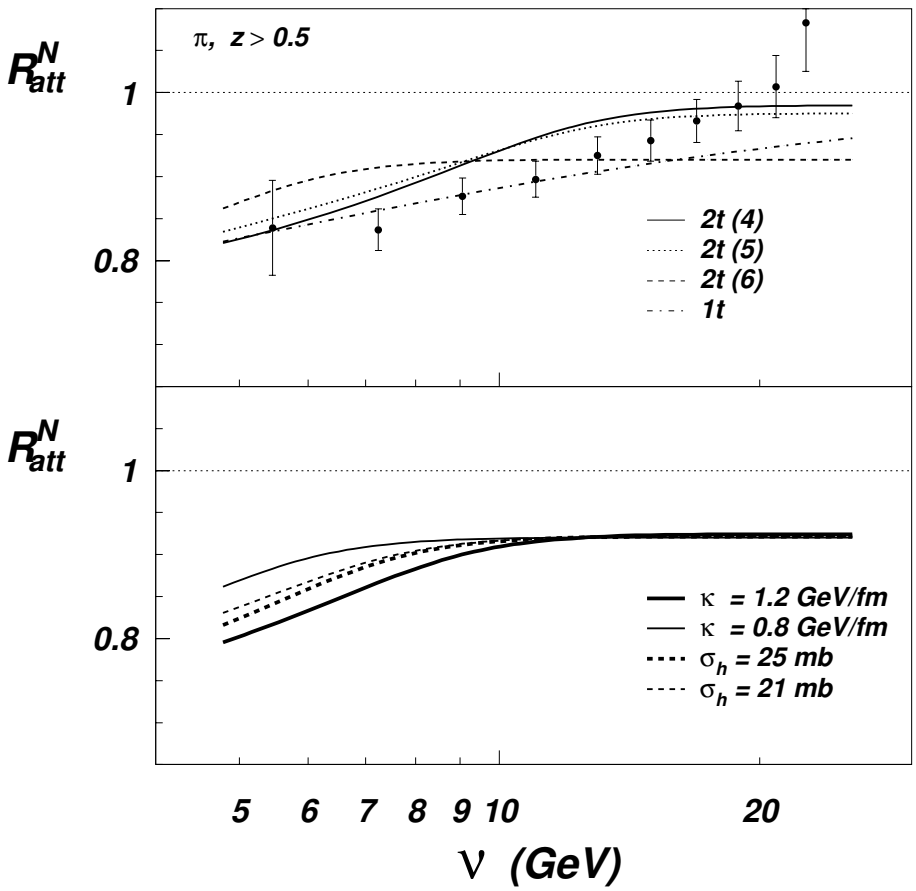

Figure 6.11: Attenuation ratio as a function of ν for fragmentation pions produced on a ^{14}N target. The error bars on the data reflect the quadratic sum of the statistical and systematic uncertainty. In the upper panel, the solid and dotted curve represent fits using the two-time scale model including the expressions for l_c and l_f from the string model, while for the dashed curve τ_c is used as a free parameter. The dot-dashed curve represents a fit using the one-time scale model with two free parameters, σ_s and τ_h/m_h ($\tau_f = z\nu\tau_h/m_h$). In the lower panel the effect of variations in σ_h and κ is shown, using the two-time scale model.

and 6.6, the curves are shown in figure 6.12. From figure 6.12 it is seen that the two-time scale model does not describe the positive and negative hadron data very well. The χ^2 values per degree of freedom (χ^2/ndf) are also shown in the tables. The fit results of the one-time scale model are better, for positive and negative hadrons the χ^2/ndf values are 1.7 and 1.2 respectively.

The fit results for τ_h/m_h and l_c for the one-time and two-time scale models are listed in tables 6.5 and 6.6, respectively. As mentioned before, it is not possible to discriminate between the two versions of the one-time scale model, $\tau_f = \nu z \tau_h/m_h$ or $\tau_f = \nu \tau_q/m_q$. Since the average z is approximately the same (≈ 0.65) for each ν bin, the value of τ_q/m_q can be calculated from $\tau_q/m_q = z\tau_h/m_h$ using fit parameter τ_h/m_h.

For the one-time scale model the dependence of the value for τ_h/m_h on the value for σ_h has been studied. The results of the fits for different values of σ_h are shown in table 6.5 as well. When the uncertainty in τ_h/m_h due to the uncertainty in σ_h is summed quadratically to the fit error of τ_h/m_h, the value for the formation time τ_f equals $(1.4\pm0.3)z\nu$ fm/c for negative hadrons, $(1.7\pm0.4)z\nu$ fm/c for positive hadrons, and $(1.0\pm0.2)z\nu$ fm/c for pions [6] (with ν in GeV). The quality of the two-time scale fits is poor, and does not allow a meaningful comparison between the τ_f values derived from the fits. Hence, we restrict this comparison to the one-time scale model.

The fitted values of the formation time for π, h^+, and h^- have been used to obtain an (model dependent) estimate of the formation times for various hadrons. The formation times for positive and negative hadrons can be expressed as a sum of the formation times τ_π, τ_k, and τ_p multiplied by the corresponding fractions of π's, K's and p's in the hadron sample (table 6.4) [7]. Since the attenuation of π^+ and π^- is the same (figure 6.7), the formation time of π^+ and π^- are also take to be equal. If the hadrons are leading hadrons, this shows that the time needed for a u-quark to pick up a $\bar{d}$-quark from the vacuum is the same as the time needed for a d-quark to pick up a $\bar{u}$-quark from the vacuum. Assuming that this is also true for the kaons, and that the formation time of a kaon is about the same as that of a pion ($=(1.0\pm0.2)z\nu$ fm/c), it follows that the formation times for protons and anti-protons are $(5 \pm 2)z\nu$ fm/c and $(6 \pm 5)z\nu$ fm/c, respectively. The formation

[6] Using a LUND Monte Carlo it has been estimated that about 20% of the pions originate from the decay of fragmentation ρ^0-mesons. Hence, the quoted formation time is a combination of the formation times for pions and ρ^0-mesons.

[7] For the purpose of this estimate the fractions f_π, f_K, and f_p are assumed to be z-independent, while it is known that these fractions depend on z.

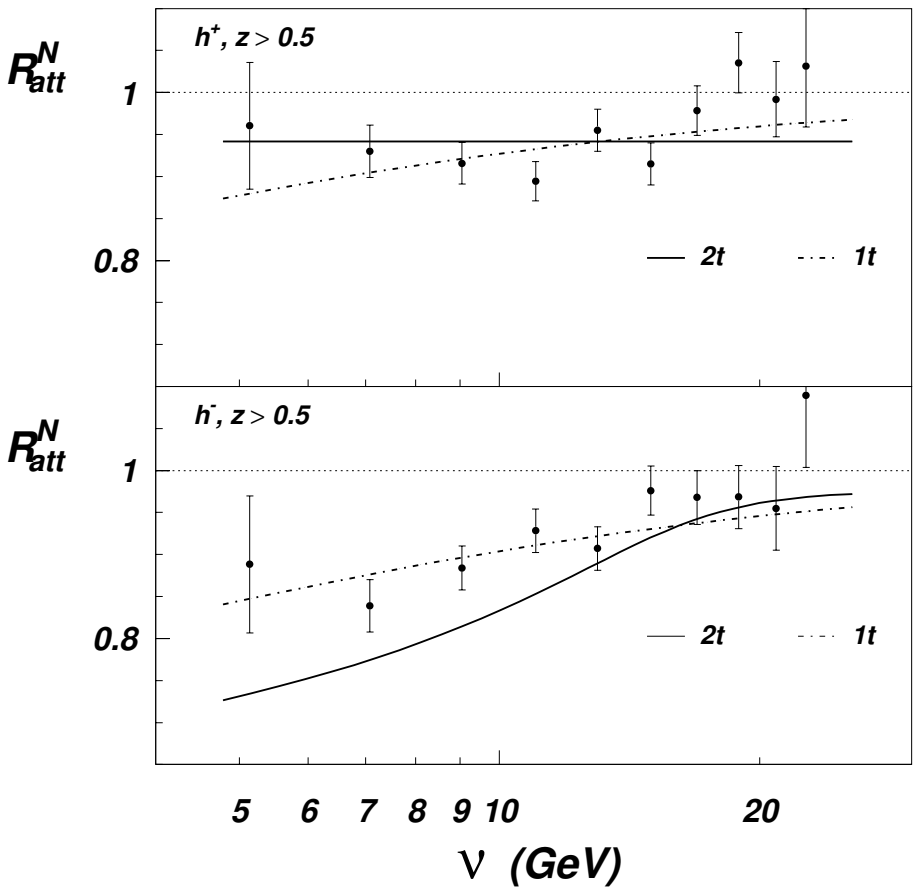

Figure 6.12: Results of the fits of the one and two-time scale models with the positive and negative hadron data. The error bars on the data reflect the quadratic sum of the statistical and systematic uncertainty. In the two-time scale fit τ_c and σ^* are free parameters and σ_s is equal to zero, while in the one-time scale model σ_s and τ_h are both free parameters. For positive hadrons $\sigma_h = 24$ mb, for negative hadrons $\sigma_h = 27$ mb.

time of a (anti-)proton thus seems to be much larger than the formation time of a pion. This may be related to the need for an additional quark in the formation process of a proton. However, the inadequacy of the model to describe the z, Q^2, and p_t-dependence of the data, and the modest quality of the fits, imply that the obtained difference of τ_p and τ_π should be regarded as a rough estimate.

Table 6.5: Results on the fit parameters for the one-time scale model. The hadron cross sections (σ_h) were fixed. For the formation time the expression $\tau_f = \nu z \tau_h / m_h$ is used.

	τ_h/m_h fmc^{-1}GeV^{-1}	$\Delta\tau_h/m_h$ fmc^{-1}GeV^{-1}	σ_s mb	$\Delta\sigma_s$ mb	σ_h mb	χ^2/ndf
π	0.9	0.1	0.0	0.3	21	2.6
	1.0	0.1	0.0	0.3	23	2.6
	1.1	0.1	0.0	0.3	25	2.6
h^+	1.5	0.3	0.0	1.6	22	1.7
	1.7	0.3	0.0	1.6	24	1.7
	1.9	0.4	0.0	1.6	26	1.7
h^-	1.3	0.2	0.0	0.6	25	1.2
	1.4	0.2	0.0	0.6	27	1.2
	1.5	0.2	0.0	0.6	29	1.2

Table 6.6: Results on the fit parameters for the two-time scale model. All hadron cross sections (σ_h) were fixed, while the quark cross sections (σ_s) were fixed only for h^+ and h^-.

	l_c fm	Δl_c fm	σ^* mb	$\Delta\sigma^*$ mb	σ_s mb	$\Delta\sigma_s$ mb	σ_h mb	κ GeV/fm	χ^2/ndf
π	0.12	0.01	100	66	0	7	23	1.0	6
h^+	6	7	3	1	0	-	24	1.0	3
h^-	0.04	0.01	100	98	0	-	27	1.0	4

6.3.2 Gluon bremsstrahlung model

In this section the results of the gluon bremsstrahlung model [8], as described in subsection 2.2.2, are compared to the R_{att} data. The model calculations assume leading hadrons, i.e. those that contain the quark which absorbed the virtual photon, and consider the formation of mesons only. Therefore, the results of the model should be compared with the data on pions for $z > 0.5$. From the results on the attenuation of pions and hadrons we have seen that there is no significant difference between the two for $z > 0.5$ and $\nu > 8$ GeV. For that reason also the hadron results are shown in the figures. The curves represent the model calculations, the open circles the pion data and the solid circles the hadron data.

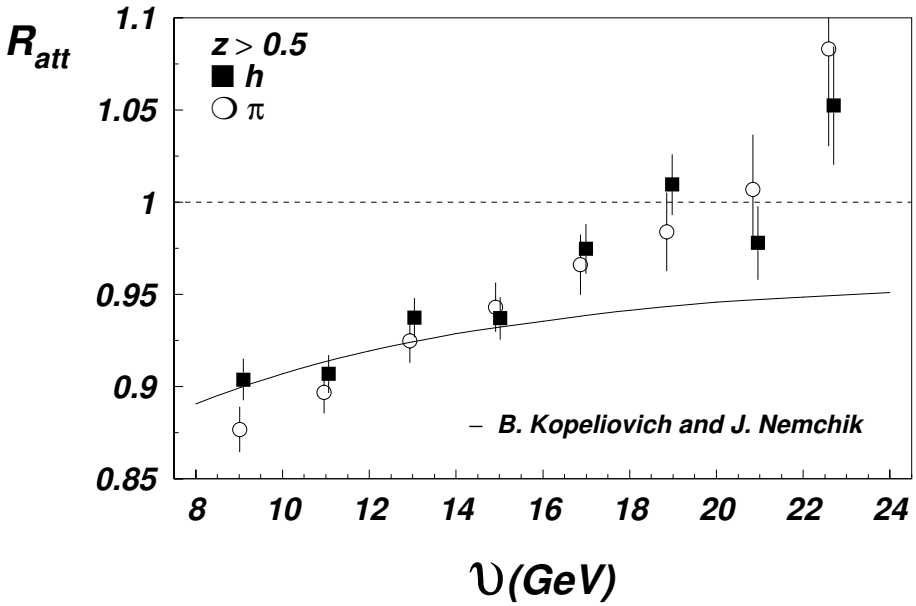

Figure 6.13: Gluon bremsstrahlung model predictions for the attenuation ratio as a function of ν for pions in a ^{14}N target. The errors are statistical only.

Figure 6.13 shows the attenuation as a function of ν. The agreement between the calculation and data is fair. At high ν values the calculations are below the data, while the ν slope seems to be less than required by the data. The main ingredient determining the slope with ν is the final hadron-nucleon cross section σ_h. At high ν values the formation time is long and

σ_h has little effect, while at low ν values the formation time is short and σ_h is relatively important. Also the interaction of the quark with the nuclear environment affects the slope, but this represents a small (few %) effect only.

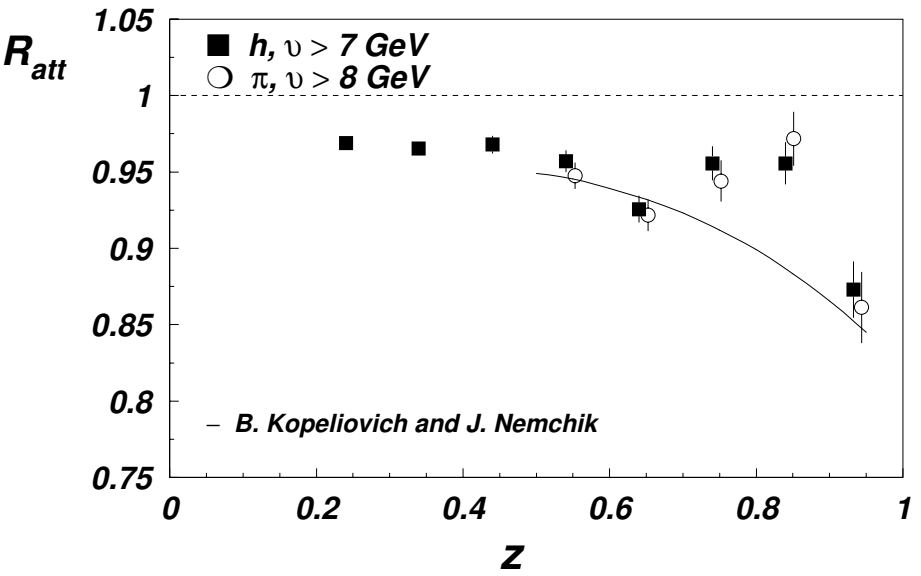

Figure 6.14: Gluon bremsstrahlung model predictions for the attenuation ratio as a function of z for pions in a ^{14}N target. The errors are statistical only.

Figure 6.14 shows the attenuation as a function of z. The fast decrease of the attenuation ratio at high z is roughly in agreement with the calculations. However, the decrease at high z of the data seems to start later than that of the calculations. Since at high z there is no energy left for the emission of gluons, high z mesons are suppressed. The nuclear environment enhances the emission of gluons, since an interaction of the quark with the nucleons result in additional gluon radiation, therefore the suppression is stronger in ^{14}N than in D (see also the text in relation to figure 6.6). The point at which the suppression starts is dependent on energy. At high values of ν the z value at which the suppression starts is higher, since at a given z-value there is more energy available for gluon radiation at high ν than at low ν. The systematic enhancement of the data with respect to the gluon bremsstrahlung calculations for $z > 0.7$ (high z corresponds in the gluon bremsstrahlung model to a short formation time, and therefore a large influence of σ_h) seems

to indicate that the emerging meson interacts with a reduced cross section with the nuclear medium.

6.4 Conclusion

Deep-inelastic scattering (DIS) data on ^{14}N and ^{2}H have been used to study hadron formation. The attenuation of hadrons (and pions separately) was determined as a function of ν, z, Q^2 and p_t with good statistics and small systematic uncertainties ($< 2\%$). No difference was observed between the attenuation of pions and all hadrons (including pions).

The attenuation ratio is found to increase with ν and equals, for hadrons with $z > 0.5$, 0.88±0.02 at a ν value of 9 GeV and 1.05±0.04 at a ν value of 23 GeV. The formation time is expected to increase with ν, therefore at high ν values the nucleus has relatively little effect and the ratio approaches unity. A difference in the ν-dependence was found between negative and positive hadrons. At low ν values positive hadrons are less attenuated, i.e. have a larger attenuation ratio, than negative hadrons. It has been shown that this may originate from a larger formation time for (anti)-protons (baryons) than for pions (mesons) which is presumably due to the need of an additional quark in the hadron formation process.

The z-dependence shows a steep decrease of the attenuation ratio at z values larger than 0.85. While at $z = 0.85$ the ratio equals 0.96±0.02, it decreases to 0.87±0.02 at $z = 0.93$. This steep decrease suggests that the probability for a leading hadron (or quark) to traverse a large nucleus like ^{14}N without loosing a significant amount of energy is very small.

The attenuation ratio is found to decrease with Q^2. The energy loss of a quark may rise with Q^2 according to reference [8], which will lead to a decreasing formation time for increasing Q^2. Hence, the effect of the hadron-nucleon cross section will increase with Q^2, and the attenuation becomes larger.

For $p_t > 0.6$ GeV the attenuation ratio is found to increase with p_t. This increase may be the result of a broadening of the p_t distribution due to rescattering of the quark and/or hadron in the nuclear environment. For $0.3 < p_t < 0.6$ GeV the attenuation ratio decreases with increasing p_t. For this behavior no explanation is available.

The results on the attenuation ratio as a function of ν are compared with the results of other experiments. The agreement with the experiments at

CERN, i.e. EMC and WA21/59 is good, while the SLAC result is two standard deviations below the HERMES and WA21/59 results. However, since the error bar of the SLAC result only contains the statistical uncertainty, the results are not necessarily inconsistent. At high ν values the HERMES results are slightly above the EMC and WA21/59 results. This may be caused by the low average z of the HERMES data at high ν. Low z hadrons may be enhanced in a nuclear environment due to rescattering processes.

The one-time and two-time scale models have been used in an effort to describe the data. Using the two-time scale model including expressions for the formation time (τ_f) based on the LUND model, the description is good for Cu, but not for ^{14}N. When the two-time scale model is fitted without assumptions on the formation time, no improvement is found. The one-time scale model fits the data reasonably well using τ_h/m_h as free parameter in $\tau_f = z\nu\tau_h/m_h$. The formation time equals $(1.4\pm0.3)z\nu$ fm/c for negative hadrons, $(1.7\pm0.4)z\nu$ fm/c for positive hadrons, and $(1.0\pm0.2)z\nu$ fm/c for pions (with ν in GeV). Under the assumption that the formation time of a kaon is equal to the formation time of a pion, and using some other simplifying assumptions, it can be shown that the formation time for protons and anti-protons is larger than the formation time for pions. However, as the one-time scale model is not able to describe the z, Q^2, and p_t-dependence as found in the experiment, the observed difference can only be considered as a model-dependent estimate. A more comprehensive approach would be needed for a more quantitative interpretation of the data.

The agreement of the gluon bremsstrahlung model with the data is fair. However, at high ν values the calculation is below the data. A steep z-dependence is predicted by the gluon bremsstrahlung model, agreeing reasonably well with the experimental results. However, the decrease of the attenuation ratio sets in at a lower z value than found experimentally. At high z the meson formation time is expected to be very short, since the quark which has absorbed the virtual photon only has to find one additional quark to form a meson. Therefore, the interaction of the final hadron with the nuclear environment has a large effect, and the attenuation ratio decreases. While the gluon bremsstrahlung model incorporates this effect, it is not present in the one-time and two-time scale models.

In summary, some intriguing (partly unexplained) dependences of the attenuation ratio on z, Q^2, ν and p_t have been observed. The HERMES experimental data are sufficiently precise to enable improvements of the gluon bremsstrahlung model and the one-time and two-time scale models. Only if

such improvements become available it will be possible to derive unambiguous values for the hadron formation time. Experimentally, additional data on heavier targets and identification possibilities for kaons, pions and protons (a RICH detector) are desirable to improve upon the present data set.

Chapter 7

Summary

In this thesis the A-dependence of deep-inelastic positron scattering off ^{14}N has been investigated. Both the ratio R of the longitudinal and transverse virtual photon absorption cross section and the hadron formation process were studied. The data were collected at the HERMES experiment at DESY. In this experiment the 27.5 GeV positrons of the HERA storage ring were scattered off a ^{14}N target. Relatively high target densities were used, leading to luminosities up to 1.2×10^{33} nucleons/cm^{2}s with a positron beam current of 32 mA.

The DIS cross section ratios $\sigma_{^{14}N}/\sigma_{^2H}$ and $\sigma_{^3He}/\sigma_{^2H}$ have been determined for $0.01 < x < 0.8$. Compared to data from the NMC and E665 experiments (using beam energies of 197 and 470 GeV, respectively) the HERMES results are significantly lower, even if the same values of x and Q^2 are considered. This observation implies that the inclusive cross section ratio is dependent on the virtual photon polarization parameter ϵ, which - on average - is largely different for the experiments. The ϵ-dependence of the cross section ratio for a given x-bin has been used in a fit in which the ratio R_A/R_D and the structure function ratio F_2^A/F_2^D are taken as free parameters. While the fitted F_2-ratios are in agreement with previous data the fitted ratios $R_{^{14}N}/R_{^2H}$ and $R_{^3He}/R_{^2H}$ show a large enhancement in the kinematic region $0.01 < x < 0.06$ and $0.3 < Q^2 < 1.5$ GeV^2. In this domain the ratios are enhanced by a factor of 5 for ^{14}N, and a factor 2.5 for ^{3}He.

The Q^2-dependence of the results on R_A/R_D suggests an interpretation in terms of a higher twist effect, which is enhanced in a nuclear medium. As a higher twist effect represents a quark-gluon correlation, the data seem to suggest enhanced quark-gluon correlations in nuclei.

Alternatively, the results on the A-dependence of R for ^{14}N have been expressed in terms of the A-dependence of the longitudinal and transverse virtual photon absorption cross section ratios, $\sigma_L^{14_N}/\sigma_L^D$ and $\sigma_T^{14_N}/\sigma_T^D$. For the lowest (x, Q^2)-bin these ratios obtain values of 2.15±0.40 and 0.45±0.04, respectively. It is concluded that a complete description of the data should encompass both the enhancement of the longitudinal and the reduction of the transverse virtual photon absorption cross section, as observed in the present experiment.

By embedding the hadron formation in a nuclear medium the space-time structure of this process has been studied. The quantity which is measured in the experiment is the attenuation ratio R_{att} which represents the number of hadrons observed per DIS event for a target with atomic mass A, divided by the same number for a deuterium target.

The attenuation of hadrons (and pions, separately) was determined as a function of ν, z, Q^2 and p_t with good statistics and small systematic uncertainty ($< 2\%$). No difference was observed between the attenuation of pions and all hadrons (including pions). However, a difference in the ν-dependence was found between negative and positive hadrons. At low ν values positive hadrons are less attenuated, i.e. have a larger attenuation ratio, than negative hadrons. It has been shown that this difference may originate from a larger formation time for (anti)-protons (baryons) than for pions (mesons), which is possibly due to the need to bring three instead of two quarks together.

Phenomenological models have been used in an effort to extract the hadron formation time τ_f from the data. It was found that so called one-time scale models with two free parameters describe the data reasonably well. The free parameters are the cross section of a quark with the nuclear environment σ_s, and τ_h/m_h in the expression for the formation time $\tau_f = z\nu\tau_h/m_h$. The cross section σ_s is found to be very small, i.e. 0 ± 2 mb. The fitted formation times τ_f are $(1.4\pm0.3)z\nu$ fm/c for negative hadrons, $(1.7\pm0.4)z\nu$ fm/c for positive hadrons, and $(1.0\pm0.2)z\nu$ fm/c for pions (with ν in GeV). Also from these values the larger formation time of positive hadrons compared to negative hadrons is evident. However, it is important to note that the used phenomenological model does not contain the proper z, Q^2, and p_t-dependence as found in the experiment. Hence, the derived formation times contain a model uncertainty which cannot be easily estimated in this framework. A more comprehensive approach is needed to extract less model dependent information on the formation times.

The data have also been compared to the gluon bremsstrahlung model as a function of ν and z. At high ν the calculation is below the data, while at low ν there is good agreement. The z-dependence of the gluon bremsstrahlung model shows a decrease of R_{att} at high z values, as is also observed in the data, but on average the calculation is below the experimental result. At high z the formation time is very short, implying that the attenuation of a hadron propagating through the nuclear environment becomes important. The difference between the data and the calculation may therefore be related to the size of the hadron-nucleus cross section which was used in the gluon bremsstrahlung model.

The HERMES experimental data of the attenuation ratio as a function of ν, z, Q^2 and p_t are valuable, as they enable improvements of both the gluon bremsstrahlung model and the phenomenological models. Such improvements are necessary in order to derive less model dependent values of the formation time. Experimentally, additional data on heavier targets and identification possibilities for kaons, pions and protons (as provided by a RICH detector) are desirable to extend the present data set.

Appendix A

DIS cross section expression

In the laboratory frame, the expression for the differential DIS cross section reads [9]

$$\frac{d\sigma}{dE'd\Omega} = \frac{4\alpha^2 E'^2}{Q^4}\left[W_2 cos^2(\frac{\Theta}{2}) + 2W_1 sin^2(\frac{\Theta}{2})\right], \tag{A.1}$$

with Θ the scattering angle and W_1 and W_2 the structure functions, parameterizing the virtual photon-hadron vertex.

Substituting

$$W_1 = \frac{F_1}{M} \quad \text{and} \quad W_2 = \frac{F_2}{\nu}, \tag{A.2}$$

and using

$$F_1 = \frac{F_2}{2x(R+1)}\left(1 + \frac{4M^2x^2}{Q^2}\right), \tag{A.3}$$

with R the ratio of the longitudional and transverse virtual photon absorption cross section ($R = \sigma_L/\sigma_T$) this gives

$$\frac{d\sigma}{dE'd\Omega} = \frac{4\alpha^2 E'^2}{Q^4}\frac{cos^2(\frac{\Theta}{2})F_2}{\nu(R+1)}\left[R + 1 + \frac{\nu}{Mx}(1 + \frac{4M^2x^2}{Q^2})tan^2(\frac{\Theta}{2})\right]. \tag{A.4}$$

By using $x = Q^2/2M\nu$, the last equation can be converted to

$$\frac{d\sigma}{dE'd\Omega} = \frac{4\alpha^2 E'^2}{Q^4}\frac{cos^2(\frac{\Theta}{2})F_2}{\nu(R+1)}\left[R + 1 + 2(\frac{\nu^2}{Q^2}+1)tan^2(\frac{\Theta}{2})\right]. \tag{A.5}$$

The expression for ϵ can be replaced,

$$\epsilon = \frac{4(1-y) - \frac{Q^2}{E^2}}{4(1-y) + 2y^2 + \frac{Q^2}{E^2}} \overset{lab}{=} \left(1 + 2(\frac{\nu^2}{Q^2}+1)tan^2(\frac{\Theta}{2})\right)^{-1}, \tag{A.6}$$

and after substitution we obtain,

$$\frac{d\sigma}{dE'd\Omega} = \frac{4\alpha^2 E'^2}{Q^4}\frac{cos^2(\frac{\Theta}{2})F_2}{\nu(R+1)}\left[R + \epsilon^{-1}\right]. \tag{A.7}$$

Using the expression for the Mott-cross section σ_{mott} which represents the cross section for scattering off a point charge with unity electric charge (also see equation 2.17),

$$\sigma_{mott} = \frac{4\alpha^2 E'^2}{Q^4}cos^2(\frac{\Theta}{2}), \tag{A.8}$$

it follows that

$$\frac{d\sigma}{dE'd\Omega} = \sigma_{mott}\frac{2MxF_2}{Q^2\epsilon}\left(\frac{1+\epsilon R}{1+R}\right). \tag{A.9}$$

Appendix B

$R_A = R_D$ in the radiative corrections

The DIS cross section ratios for $^{14}N/D$ and $^{3}He/D$ are presented as function of Q^2 in the same way as in chapter 5, but now assuming R_A=R_D in the radiative corrections. Also shown is the result of the ϵ-fit in terms of R_A/R_D versus Q^2 in a separate figure. It is seen that the obtained values of R_A/R_D are smaller than those discussed in chapter 5, but qualitatively the same conclusions can be derived from the data.

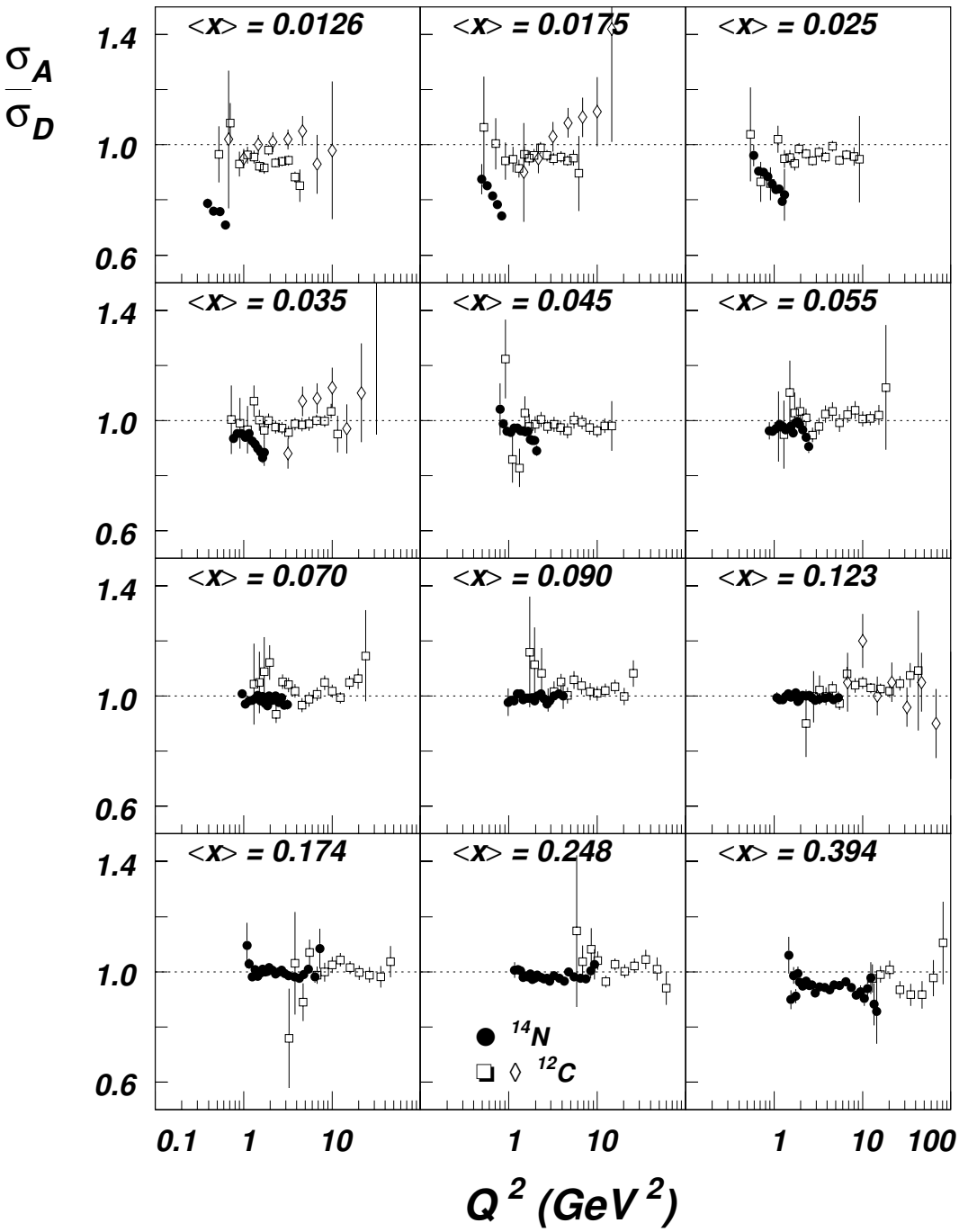

Figure B.1: Ratio of the cross sections per nucleon as function of Q^2 for different x-regions. For the radiative corrections it is assumed that R_A=R_D. The HERMES data on ^{14}N are represented as solid circles, the NMC and E665 data on ^{12}C as open squares and open diamonds, respectively.

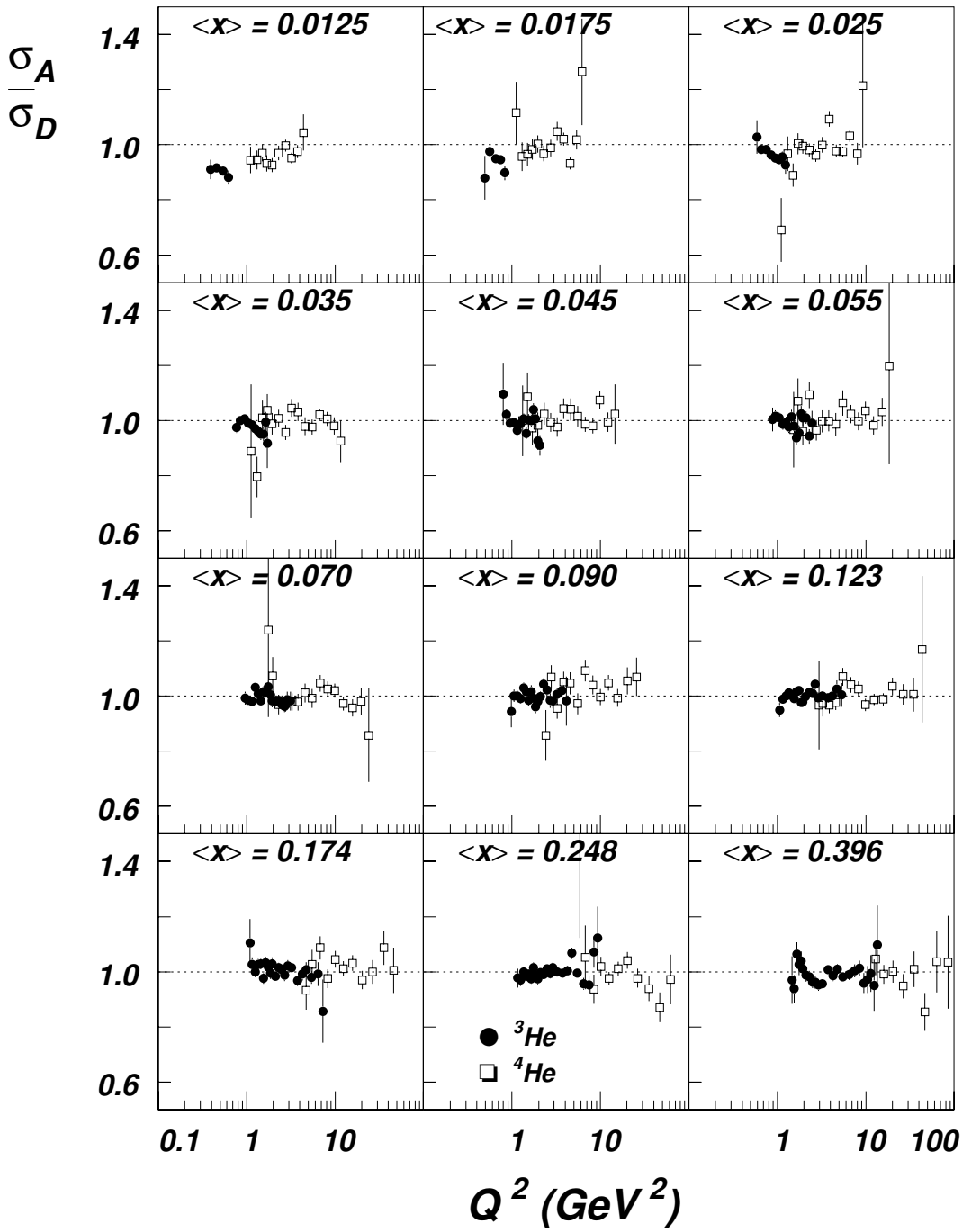

Figure B.2: Ratio of the cross sections per nucleon as function of Q^2 for different x-regions. For the radiative corrections it is assumed that R_A=R_D. The HERMES data on ^{3}He are represented as solid circles, the NMC data on ^{4}He as open squares.

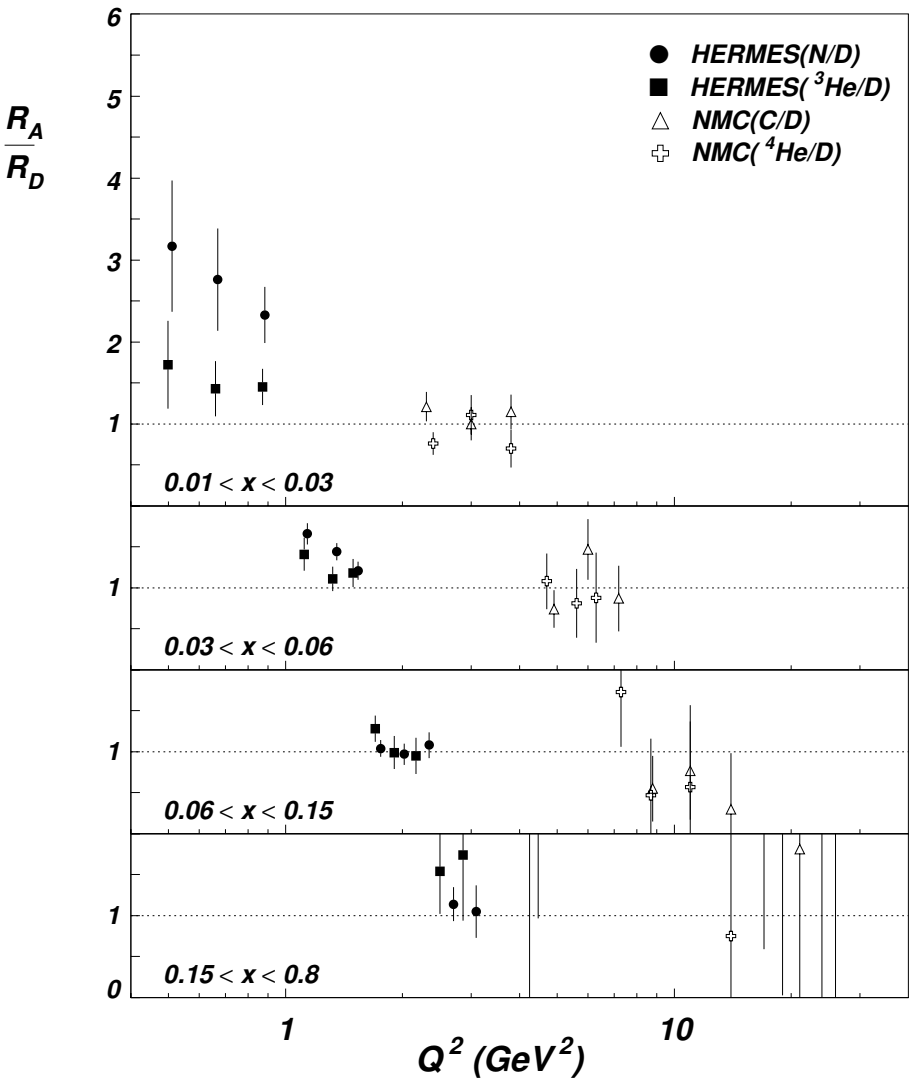

Figure B.3: The obtained values of R_A/R_D as function of Q^2. The errors bars on the points include the fit errors as well as the systematic errors (summed quadratically). The systematic error arises from the radiative corrections and a normalization error of 1.5%. The error due to the uncertainty in R1998 is smaller than 1%.

Bibliography

[1] J.J. Aubert et al., *Phys. Lett.* B **123**, 275 (1983)

[2] M. Arneodo, *Phys. Rep.* **240**, 301 (1994).

[3] R.K. Ellis, W. Furmanski and R. Petronzio, *Nucl. Phys.* B **207**, 1 (1982).

[4] S. Barshay and D. Rein, *Z. Phys.* C **46**, 215 (1990).

[5] M. Arneodo et al., Proceedings of the workshop on Future Physics at HERA, Edited by G. Ingelman, A. De Roeck and R. Klanner, DESY, 1995/1996, vol 2, 887.

[6] G. van der Steenhoven, *Nucl. Phys.* A **662**, 31c (1997).

[7] J. Ashman et al., *Z. Phys.* C **52**, 1 (1991).

[8] B. Kopeliovich et al., Proceedings of the workshop on Future Physics at HERA, Edited by G. Ingelman, A. De Roeck and R. Klanner, DESY, 1995/1996, vol 2, 1038.

[9] F. Halzen and A.D. Martin, *Quarks & Leptons: An introductory Course in Modern Particle Physiscs*, JOHN WILEY & SONS, 1984.

[10] G. Altarelli and G. Parisi, *Nucl. Phys.* B **126**, 298 (1977).

[11] M. Glück, E. Reya, M. Stratmann, and W. Vogelsang, *Phys. Rev.* D **53**, 4775 (1996).

[12] U.K. Yang and A. Bodek, *Phys. Rev. Lett.* **82**, 2467 (1999).

[13] M. Dasgupta and B.R. Webber, *Phys. Lett.* B **382**, 273 (1996). *Phys. Rev.* D **53**, 4775 (1996)

[14] U.K. Yang and A. Bodek, submitted to Phys. Rev. Lett., hep-ex/9908058.

[15] P. Amaudruz et al., *Nucl. Phys.* B **441**, 3 (1995).

[16] J. Gomez et al., *Phys. Rev.* D **49**, 4348 (1994).

[17] M.R. Adams et al., *Z. Phys.* C **67**, 403 (1995).

[18] G. Piller and W. Weise, hep-ph/9908230.

[19] K. Abe at al., *Phys. Lett.* B **452**, 194 (1999).

[20] J. Milana, *Phys. Rev.* C **49**, 2820 (1994).

[21] T. Gousset and H.J. Pirner, *Phys. Lett.* B **375**, 349 (1996).

[22] N.N. Nikolaev and B.G. Zakharov, *Z. Phys.* C **49**, 607 (1991).

[23] B. Kopeliovich, Study presented at the Workshop on Structure Functions and Higher Twist Effects, MIT, Boston, October 1 and 2, 1999.

[24] J. Franz et al., *Z. Phys.* C **10**, 105 (1981).

[25] J. Bailey et al., *Nucl. Phys.* B **151**, 367 (1979).

[26] J. Eickmeyer et al., *Phys. Rev. Lett.* **36**, 289 (1976).

[27] W.R. Ditzler et al., *Phys. Lett.* B **57**, 201 (1975), S. Stein et al., *Phys. Rev.* D **12**, 1884 (1975).

[28] M.S. Goodman et al., *Phys. Rev. Lett.* **47**, 293 (1981).

[29] P. Amaudruz et al., *Phys. Lett.* B **294**, 120 (1992).

[30] M. Arneodo et al., *Nucl. Phys.* B **481**, 23 (1996).

[31] S. Dasu et al., *Phys. Rev.* D **49**, 5641 (1994).

[32] A. Bialas and T. Chmaj, *Phys. Lett.* B **133**, 241 (1983).

[33] A. Bialas and M. Gyulassy, *Nucl. Phys.* B **291**, 793 (1987).

[34] B. Andersson et al., *Phys. Rep.* **97**, 31 (1983).

[35] L.S. Osborne et al., *Phys. Rev. Lett.* **40**, 25 (1978).

[36] K. Ackerstaff et al., *Nucl. Instrum. Methods* A **417**, 230 (1998).

[37] The HERMES collaboration. *Technical Design Report*, Technical Report DESY-PRC 93/06, DESY,1993.

[38] J. Blouw, Ph.D. Thesis, NIKHEF/Vrije Universiteit, Amsterdam, October 1998.

[39] J. Blouw et al., *Nucl. Instrum. Methods* A **434**, 227 (1999).

[40] F.G. Hartjes et al. Proceedings of The International Workshop on Micro-Strip Gas Chambers, Legnaro(Italy), 13-14 October 1994. NIKHEF-H/94-36

[41] F. van de Berg et al., *Gas gain stability in MSGCs and MGCs at high rate operation.*, NIKHEF/97-014

[42] F. Sauli, *Nucl. Instrum. Methods* A **386**, 531 (1997).

[43] F. Sauli et al., *Nucl. Instrum. Methods* A **409**, 79 (1998).

[44] T. Zeuner (for the HERA-B Inner Tracker Collaboration), submitted to Beauty99, 6^{th} International Conference on B-Physics with Hadron Machines, June 21-25, 1999, Bled, Slovenia.

[45] W. Wander., *Rekonstruktion hochenergetischer streuereignisse im HERMES Experiment.*, PhD thesis, 1996. HERMES internal note 96-023.

[46] I.V. Akushevich et al., *Nucl. Part. Phys.* **20**, 513 (1994).

[47] A. A. Akhudov, D. Yu. Bardin, and N.M. Shumeiko, *Sov. J. Nucl. Phys.* D **26**, 660 (1977)

[48] D. Yu. Bardin, and N.M. Shumeiko, *Sov. J. Nucl. Phys.* D **29**, 499 (1979)

[49] A. A. Akhudov et al., *Sov. J. Nucl. Phys.* D **44**, 988 (1986)

[50] L.W. Whitlow et al., *Phys. Lett.* B **250**, 193 (1990).

[51] M. Arneodo et al., *Nucl. Phys.* B **487**, 3 (1997).

[52] A. Svarc and M.P. Locher, *Fizika* **22**, 549 (1990); M.P. Locher and A. Svarc, *Z. Phys.* A **338**, 89 (1991).

[53] J.S. McCarthy, I. Sick and R.R. Whitney, *Phys. Rev.* C **15**, 1396 (1977)

[54] C.W. de Jager et al., *Atom. Data and Nucl. Data Tables* **14**, 479 (1974).

[55] M. Gari and W. Krümpelmann, *Z. Phys.* A **322**, 689 (1985).

[56] J. Bernabeu, *Nucl. Phys.* B **49**, 186 (1972).

[57] E.J. Moniz et al., *Phys. Rev.* **184**, 1154 (1969)

[58] I. Akushevich, A. Brüll, T. Shin., *Radiative corrections to the structure function ratios.*, HERMES INTERNAL note.

[59] S. Platchkov, *Nucl. Phys.* A **510**, 740 (1990); P.C. Dunn et al., *Phys. Rev.* C **26**, 71 (1983); H. de Vries et al., *Atom. Data and Nucl. Data Tables* **36**, 501 (1987); R.L. Huffmann et al., *Phys. Lett.* B **139**, 249 (1984).

[60] H. Arenhövel, private communication (1998); D. Day, private communication (1998).

[61] M. Düeren, P. Geiger, N. Makins, E. Volk, and P. Welch, *The HERMES Monte Carlo.*, http://www.mpi-hd.mpg.de/herprod/.

[62] I. Akushevich et al., *Comp. Phys. Comm.* **104**, 201 (1997).

[63] T.S. Tsai, *Phys. Rev.* **120**, 269 (1960) and L.W. Mo and T.S. Tsai, *Rev. Mod. Phys.* **41**, 205 (1969)

[64] L. Griegee et al., *Nucl. Phys.* B **121**, 38 (1977).

[65] M. Strikman, private communication (Boston, October 1999).

[66] B. Kopeliovich, private communication (Boston, October 1999).

[67] K. Rith, *Z. Phys.* C **38**, 317 (1988).

[68] E.V. Shuryak, *Nucl. Phys.* A **446**, 259 (1985).

[69] Sverker Fredriksson, *Phys. Rev. Lett.* **52**, 724 (1984).

[70] Svante Ekelin and Sverker Fredriksson, *Phys. Lett.* B **162**, 373 (1985).

[71] A. Brüll, J.J. van Hunen, T. Shin, G. van der Steenhoven and P.K.A. de Witt Huberts, *Report on the F_2^N/F_2^D and F_2^{He}/F_2^D structure function analysis*, 1999, HERMES internal note.

[72] K. Ackerstaff et al., *Phys. Rev. Lett.* **82**, 3025 (1999).

[73] N. Bianchi, V. Muccifora, P. Di Nezza, N. Bianchi, J.J. van Hunen and G. van der Steenhoven, *Hadron Attenuation in ^{14}N*, 1999, HERMES internal note.

[74] L.L. Frankfurt, G.A. Miller, and M. Strikman, *Annu. Rev. Nucl. Part. Sci.* **45**, 501 (1994).

[75] T. Chmaj, *Acta Phys. Pol.* B **18**, 1131 (1987).

[76] W. Burkot et al., *Z. Phys.* C **70**, 47 (1996).

[77] Particle Data Group *Review of Particle Physics*, *Phys. Rev.* D **54**, 182 (1996).

Samenvatting

Alle materie die ons omringt is opgebouwd uit atomen. Elk atoom bestaat uit een zeer kleine compacte kern omringd door elektronen. De atoomkernen van de verschillende soorten materie (waterstof, stikstof, ijzer, enzovoort) onderscheiden zich door verschillende aantallen neutronen en protonen (nucleonen). Nucleonen zijn opgebouwd uit quarks en gluonen. Quarks zijn, voor zover bekend, ondeelbaar. Gluonen zijn de dragers van de "sterke kracht" die zorgdragen voor de binding van de quarks in het nucleon. Quarks komen niet vrij in de natuur voor, ze zijn altijd gebonden met minstens één ander quark.

Informatie over de quark-gluon structuur van het nucleon kan worden verkregen door hoogenergetische elektronen met een atoomkern te laten botsen. Indien de energie van het elektron hoog genoeg is, treedt met een zekere waarschijnlijkheid verstrooiing (verandering van richting en energie) van een elektron aan een quark in één van de nucleonen op. Zo'n verstrooiingsproces wordt beschreven als de overdracht van een foton (de drager van de "elektromagnetische kracht") van het elektron aan de quark. Omdat impuls en energie van dit foton niet gelijk zijn, betekent dit dat het foton geen gewoon foton is (zoals bij licht), maar een virtueel foton. De impulsoverdracht is een maat voor het oplossend vermogen (resolutie) van het verstrooiingsproces. Het verstrooiingsproces wordt verder gekarakteriseerd door de polarisatie van het virtuele foton. De draaiende beweging (spin) van het foton is longitudinaal of transversaal ten opzichte van bewegingsrichting van het foton.

Indien het nucleon deel uitmaakt van een atoomkern kan informatie worden verkregen over de invloed van de omringende nucleonen op, onder andere, de werkzame doorsnede (σ) van het verstrooiingsproces van het elektron aan de quark. De werkzame doorsnede is een maat voor de waarschijnlijkheid dat de verstrooiing optreedt. Voor 1982 was de verwachting dat de invloed

van de omringende nucleonen te verwaarlozen zou zijn, omdat het elektron een energie aan de quark overdraagt die zo'n honderd maal groter is dan de bindingsenergie van de nucleonen in de atoomkern. Bij experimenten op het CERN (in Geneve) in 1982 is echter gebleken dat deze verwachting onjuist is. Het onderzoek dat is beschreven in het eerste deel van dit proefschrift richt zich op de vraag naar de invloed van de omringende nucleonen op de werkzame doorsnede van elektron-quark verstrooiing.

Door de absorptie van het hoogenergetische foton zal de quark zich verwijderen van de omringende quarks in het nucleon, en combineert dan met één of meerdere quarks - die voornamelijk voortkomen uit het omringende vacuüm - tot een reëel deeltje (hadron). Door dit formatieproces te laten plaatsvinden in een atoomkern is het mogelijk de tijdsduur van hadronformatie te bestuderen. De atoomkern functioneert dan als een soort filter. Als het hadron snel wordt gevormd is de afstand die het hadron door de atoomkern moet afleggen groot, en is de kans op energieverlies van het hadron door wisselwerkingen met de atoomkern ook groot. Evenals het hadron kan ook de quark wisselwerken met de atoomkern, echter de waarschijnlijkheden voor deze wisselwerkingen zijn niet gelijk. Informatie over de tijdsduur die nodig is voor de formatie van een hadron kan worden verkregen indien de hadronen worden waargenomen met een detector, en het aantal en de energie van de hadronen worden vergeleken met de situatie waarbij een zeer kleine atoomkern wordt gebruikt.

Het verstrooiingsexperiment dat is beschreven in dit proefschrift is uitgevoerd met een experimentele opstelling bij DESY (in Hamburg), die de naam HERMES draagt. In het resterende gedeelte van deze samenvatting zullen de experimentele resultaten worden beschreven. De invloed van de omringende nucleonen op het elektron-quark verstrooiingsproces en het hadron formatieprocess worden achtereenvolgens besproken.

De verhouding van de werkzame doorsnedes voor verstrooiing aan stikstof (7 neutronen en 7 protonen) en deuterium (1 neutron en 1 proton), $\sigma_{14_N}/\sigma_{2_H}$, is bepaald voor verschillende waarden van de energie- en impulsoverdracht. De waarden voor $\sigma_{14_N}/\sigma_{2_H}$ zijn beduidend lager dan kan worden verwacht op basis van metingen die eerder zijn uitgevoerd bij het CERN. Het verschil tussen de HERMES en CERN metingen is in dit proefschrift toegeschreven aan een afhankelijkheid van de verhouding $\sigma_{14_N}/\sigma_{2_H}$ van de polarisatie van het virtuele foton. Dit is mogelijk omdat de fotonpolarisatie verschillend is voor de twee experimenten. Door gebruik te maken van de afhanke-

lijkheid van $\sigma_{14_N}/\sigma_{2_H}$ van de fotonpolarisatie kan afzonderlijke informatie worden verkregen over de verandering van de longitudinale en transversale verstrooiing in stikstof ten opzichte van deuterium.

Bij lage waarden van de impulsoverdracht blijkt de werkzame doorsnede voor de absorptie van transversaal gepolariseerde fotonen een factor twee kleiner te zijn voor stikstof dan voor deuterium, terwijl voor longitudinaal gepolariseerde fotonen de werkzame doorsnede juist een factor twee groter is. De afhankelijkheid van de werkzame doorsnedeverhouding van de impulsoverdracht lijkt te suggereren dat de waargenomen verschijnselen het gevolg zijn van wisselwerkingen tussen quarks van verschillende nucleonen. Op dit moment zijn er echter nog geen exacte berekeningen beschikbaar om deze interpretatie kwantitatief te verifieren.

Eén van de belangrijkste waarnemingen is dat de formatie van positief geladen hadronen minder invloed ondervindt van de atoomkern dan de formatie van negatief geladen hadronen. Voor positieve hadronen is de fractie baryonen (hadronen bestaande uit drie quarks) in vergelijking met mesonen (hadronen bestaande uit twee quarks) groter dan voor negatieve hadronen. Het verschil tussen de positieve en negatieve hadronen kan worden begrepen door aan te nemen dat baryonen een langere tijd nodig hebben om te ontstaan dan mesonen. Daardoor hebben zij een kleinere kans om met nucleonen in de atoomkern te wisselwerken. Dit is in tegenspraak met een aantal (eenvoudige) modellen voor hadron formatie, die een formatietijd voorspellen die omgekeerd evenredig is met de massa van het gevormde hadron.

Het blijkt dat bij deuterium meer hadronen met een grote fractie van de energie van het virtuele foton worden gedetecteerd dan bij stikstof. Dit wijst er op dat een hadron en/of quark een kleine kans heeft om de atoomkern te doorkruisen zonder dat het energie verliest. Wanneer de waarschijnlijkheid voor een wisselwerking van de quark met de atoomkern kleiner is dan voor een hadron, zoals blijkt uit eenvoudige modellen, is een mogelijke oorzaak hiervoor dat de formatietijd voor een hadron met een hoge energiefractie relatief klein is. Een vergelijking van de meetgegevens met modellen waarbij het formatieproces is opgedeeld in twee of drie perioden, laat zien dat dergelijke modellen in de huidige vorm niet is staat zijn alle meetgegevens adequaat te beschrijven. Modellen die gebaseerd zijn op de emissie van gluonen beschrijven de meetgegevens redelijk.

Acknowledgements

First, I would like to thank my supervisor Gerard van der Steenhoven and promotor Peter de Witt Huberts.

The enormous enthusiasm of Gerard, his support, and all the discussions about physics and data analysis have been of great value. I appreciate the time and energy, often in weekends and evenings, that Gerard spent reading and commenting my manuscripts.

Peter I would like to thank for the numerous occasions that we discussed physics in his office. The exactitude of Peter -"if possible, please quantify"- has contributed to the clarity of this thesis.

Concerning the operation of the HERMES Vertex Chamber I would like to thank the NIKHEF technical departments, specially Martin Doets, Martin van Beuzekom, Peter Jansweijer, Erwin Kok and Joop Rövekamp, for their excellent technical support. Furthermore I would like to thank Fred Hartjes and Thomas Henkes for introducing me to the HERMES Vertex Chamber.

During the four years that I worked for the HERMES experiment I worked with many colleagues. The collaboration with all of them has been very pleasant. I very much enjoyed their kindness.

I would like to thank Ger van Middelkoop and Klaus Rith for their commentary leading to improvements of this thesis.

Finally, I would like to thank my wife, Kirsi Silander, for her continuous support while I was working on this thesis, and for her flexibility and willingness to spend much of her spare time traveling to Hamburg to spend weekends with me.

Curriculum vitae

- Surname: van Hunen
  First names: Jeroen Jaap
  Date of birth: April 14, 1968
  Place of birth: London, Canada

- Education and work experience

- VWO, Marnix College, Ede, The Netherlands.

- August 1988 - August 1994: Delft University of Technology, Department of Applied Physics, Radiation Technology Group, Delft, The Netherlands.
  August 1992 - July 1993: Research Associate at the Department of Physics, University of Alberta, Edmonton, Canada. Lifetime measurements of atomic excited states.

- September 1994 - December 1995: Research Associate at the Universidade de Coimbra, Coimbra, Portugal. Design and construction of a Xe-filled scintillation detector with a CsI electron multiplier.

- Since January 1996: Ph.D. student at the Nationaal Instituut voor Kernfysica en Hoge-Energiefysica, NIKHEF, Amsterdam, The Netherlands.
  February 1997 - October 1998: Responsible for the Vertex Chamber at the HERMES Experiment, DESY, Hamburg, Germany.